NASA/CR-2005-213938

Modeling of Turbulent Boundary Layer Surface Pressure Fluctuation Auto and Cross Spectra – Verification and Adjustments Based on TU-144LL Data

Robert Rackl and Adam Weston
The Boeing Company, Seattle, Washington

December 2005

Since its founding, NASA has been dedicated to the advancement of aeronautics and space science. The NASA Scientific and Technical Information (STI) Program Office plays a key part in helping NASA maintain this important role.

The NASA STI Program Office is operated by Langley Research Center, the lead center for NASA's scientific and technical information. The NASA STI Program Office provides access to the NASA STI Database, the largest collection of aeronautical and space science STI in the world. The Program Office is also NASA's institutional mechanism for disseminating the results of its research and development activities. These results are published by NASA in the NASA STI Report Series, which includes the following report types:

- TECHNICAL PUBLICATION. Reports of completed research or a major significant phase of research that present the results of NASA programs and include extensive data or theoretical analysis. Includes compilations of significant scientific and technical data and information deemed to be of continuing reference value. NASA counterpart of peer-reviewed formal professional papers, but having less stringent limitations on manuscript length and extent of graphic presentations.

- TECHNICAL MEMORANDUM. Scientific and technical findings that are preliminary or of specialized interest, e.g., quick release reports, working papers, and bibliographies that contain minimal annotation. Does not contain extensive analysis.

- CONTRACTOR REPORT. Scientific and technical findings by NASA-sponsored contractors and grantees.

- CONFERENCE PUBLICATION. Collected papers from scientific and technical conferences, symposia, seminars, or other meetings sponsored or co-sponsored by NASA.

- SPECIAL PUBLICATION. Scientific, technical, or historical information from NASA programs, projects, and missions, often concerned with subjects having substantial public interest.

- TECHNICAL TRANSLATION. English-language translations of foreign scientific and technical material pertinent to NASA's mission.

Specialized services that complement the STI Program Office's diverse offerings include creating custom thesauri, building customized databases, organizing and publishing research results ... even providing videos.

For more information about the NASA STI Program Office, see the following:

- Access the NASA STI Program Home Page at *http://www.sti.nasa.gov*

- E-mail your question via the Internet to help@sti.nasa.gov

- Fax your question to the NASA STI Help Desk at (301) 621-0134

- Phone the NASA STI Help Desk at (301) 621-0390

- Write to:
  NASA STI Help Desk
  NASA Center for AeroSpace Information
  7121 Standard Drive
  Hanover, MD 21076-1320

NASA/CR-2005-213938

Modeling of Turbulent Boundary Layer Surface Pressure Fluctuation Auto and Cross Spectra – Verification and Adjustments Based on TU-144LL Data

Robert Rackl and Adam Weston
The Boeing Company, Seattle, Washington

Available from:

Preface

The random fluctuations generated by the turbulent boundary layer are a dominant source of interior cabin noise at subsonic as well as supersonic speeds; added treatment to manage this noise usually is a significant weight consideration. Fluctuating surface pressure measurements were conducted on flight tests of the Tupolev 144LL Flying Laboratory in late 1997 and early 1998 in Russia. These flight tests used pressure sensors mounted in cabin window blanks in different locations down the length of the fuselage. The recorded data were returned to the U.S. for analysis by NASA and Boeing.

The literature on turbulent boundary layer pressure fluctuations provides several empirical models which were compared to the measured TU-144 data. The model developed by Efimtsov showed the best agreement. Adjustments were made to improve its agreement further, consisting of the addition of a broad band peak in the mid frequencies, and a minor modification to the high frequency roll-off. The adjusted Efimtsov predicted and measured results are compared for both subsonic and supersonic flight conditions. Measurements in the forward and middle portions of the fuselage have better agreement with the model than those from the aft portion. For High Speed Civil Transport supersonic cruise, interior levels predicted by use of this model are expected to increase by 1 to 3 dB due to the adjustments to the Efimtsov model.

The space-time cross-correlations and cross-spectra of the fluctuating surface pressure were also investigated. This analysis is an important ingredient in structural acoustic models of aircraft interior noise. Once again the measured data were compared to the predicted levels from the Efimtsov model. No adjustments were made to the cross-correlation portion of the prediction model.

The auto-spectral model presented in this report can be used as improved input data to structural acoustic prediction models. However, further investigation of the cross-functional model is recommended to fully utilize the information available from the TU-144 measured data.

Table of Contents

List of Figures

List of Tables

1. Introduction

The motivation for this work stems from the need for an aerodynamic loads model for predicting passenger aircraft interior noise, at subsonic as well as supersonic cruising speeds. The turbulent boundary layer on the fuselage causes structural vibrations which radiate random noise into cockpit and passenger cabin. Simple interior noise prediction models use auto spectra of the pressure fluctuations. More complex models require space-time cross-correlations (or cross-spectra) of pressure fluctuations.

This work was performed at the Boeing Company under NASA Contract 20220, High Speed Research Program, Phase II, Task 27, Structural Acoustics. The objective was the validation of fluctuating pressure turbulent boundary layer models or model, both for single signals (auto spectra) and signal pairs (cross spectra).

The data set underlying this study came from measurements during flight tests of the Tupolev 144 Supersonic Flying Laboratory in late 1997 and early 1998 [Ref. 10].

2. Models

Several models available in the literature are discussed and then used to compare the present data with their predictions. A model by Smol'yakov-Tkachenko [Ref. 17] is not used because it was built with marine applications in mind and is not well suited to high speed flight [Ref. 11]. As discussed in the Sections below, several authors have built different models for power spectra (auto spectra) at a single point of the surface. In those references, models for space-time cross-correlation or frequency-wave number cross spectra are either not discussed, or are cast in only one form (exponential decay with spatial separation) which is discussed in Section 2.5 (Efimtsov). The equations presented here are meant to convey the flavor and complexity of the models. If the reader wishes to actually implement any of these, please refer to the complete references.

2.1 Robertson [Ref. 1]

This prediction of the turbulent boundary layer fluctuating pressure power spectrum is derived from an empirical evaluation of sub-sonic and super-sonic wind tunnel experimental results. The normalized equation for the frequency spectrum is a function of an estimate of the mean squared pressure and the Strouhal number.

$$\frac{\Phi(\omega)U_\infty}{q_\infty^2 \delta^*} = \frac{\dfrac{\overline{P^2}}{q_\infty^2}}{\dfrac{\omega_0 \delta^*}{U_\infty}\left(1+\left(\omega/\omega_0\right)^{0.9}\right)^2}$$

Where:

$$\omega_0 = 0.5\frac{U_\infty}{\delta^*} \qquad \text{and} \qquad \frac{\overline{P^2}}{q_\infty^2} = \frac{\left(0.006\right)^2}{\left(1+0.14M^2\right)^2}$$

2.2 ESDU [Ref. 2]

The predicted power spectrum is based on an analysis of flight test results. Fluctuating pressure levels, flow field, and boundary layer parameters from flight testing is curve fitted to determine the

predicted octave and third octave band levels. The prediction is a function of: Mach number, Strouhal number, and Reynolds number. The curve fitting equations appear in Section 10 (Appendix A).

2.3 Laganelli [Ref. 3]

Predicted power spectra are derived from experimental and fluid dynamic principles. Experimental data includes: AFWAL Mach 3 facility, Blake, Laganelli, Raman, Coe, and Bull (these do not appear to include flight data). The equation is an expansion of Robertson's equation, but adds friction coefficient considerations:

$$\frac{\Phi(\omega)U_\infty}{q^2\delta^*} = 2.293 \times \frac{10^{-5} F_C^{-0.5733}}{1 + F_C^{2.867}\left(\dfrac{\delta^*}{U_\infty}\omega\right)^2}$$

where F_c is a transformation from compressible to incompressible flow states:

$$F_c = \frac{C_{f_i}}{C_{f_c}} = \frac{h^*}{h_e} = \frac{1}{2} + \frac{h_w}{h_{aw}}\left(\frac{1}{2} + r\frac{\gamma-1}{2}M^2\right) + 0.22r\frac{\gamma-1}{2}M^2$$

2.4 Goodwin [Ref. 4]

This fluctuating pressure predicted spectrum was derived from previous prediction equations and flight test data on three super-sonic test aircraft: XB-70, A3J, and Concorde. A very small portion of the XB-70 data and even less of the A3J data was usable for this type of prediction due to a number of experimental errors. Additionally, the Concorde data, which used Kulites in window blanks very similar to those used for the Tu144 testing, is somewhat suspect due to the experimenter not paying close attention to the sensitivity of the Kulites to the flushness of the sensor's surface relative to the surrounding surface (discussed further in Section 3.1.3). The Kulite measurements varied as much as 9 dB between sensors in the same window blank. This test also experienced trouble duplicating results for repeated test conditions. Goodwin adjusted the Robertson and Laganelli predictions to account for the measured in-flight data using the following equations:

$$\Phi(f) = \frac{\dfrac{2}{\pi}\left(\dfrac{P_{rms}}{q_\infty}\right)^2\left(\dfrac{\rho_w(T_w,P_w)}{\rho_\infty}\right)^3\left(1.2 + 0.1\left(\dfrac{n-7}{7}\right)^{0.45}\right)}{1 + \left(\dfrac{1.2\theta\omega}{U_\infty}\right)^2}$$

$$n = 4.0 + 2.5\log_{10}\left(\frac{Re_x}{631,000}\right)$$

$$P_{rms}^2 = \frac{2}{\pi}\frac{A}{B}\frac{U_\infty}{\theta}\Phi_{pp}(0)$$

$$A = \left(\frac{\rho_\infty}{\rho_w(T_w,P_\infty)}\right)^3\frac{\theta}{\delta^*}\left(1 + 0.08\left(\frac{n-7}{7}\right)^{0.45}\right), B = Constant = 1.2$$

2

2.5 Efimtsov [Ref. 5 and 13]

Professor B. M. Efimtsov of TsAGI (Central Aerohydrodynamic Institute in Moscow, Russia) updated the existing model of turbulent boundary layer fluctuating pressure levels. This new model utilized data from the low and high speed TsAGI wind tunnels, Tu144, and what appears to be a TU-22 (twin engined, supersonic military aircraft) in-flight measurements. Details of the flight conditions and sensor locations are given; they appear to be similar to those measured on the Tu144 by NASA-Boeing. However, no actual flight data is presented for direct comparison to the NASA-Boeing tests.

The analytical derivation of the TsAGI predicted power spectrum references Laganelli's calculations; the principal independent variables are Strouhal number and Reynolds number. Efimtsov's equation is:

$$\Phi(\omega) = 2\pi\alpha U_\tau^3 \rho^2 \delta \frac{\beta}{\left(1 + 8\alpha^3 Sh^2\right)^{1/3} + \alpha\beta Re_\tau \left(Sh / Re_\tau\right)^{10/3}},$$

$$\beta = \left[1 + \left(Re_{\tau 0} / Re_\tau\right)^3\right]^{1/3}, \alpha = 0.01, \qquad Sh = \frac{\omega\delta}{U_\tau} \text{ (Strouhal Number)}$$

The model for cross-spectral density assumes that dependencies on frequency and spatial separation can be mathematically separated as follows:

$$\Phi(\xi_1, \xi_2, \omega) = \Phi(\omega) e^{\left[-\frac{|\xi_1|}{\Lambda_1} - \frac{|\xi_2|}{\Lambda_2} - i\omega\xi_1 U_p\right]}$$

where subscript 1 refers to the longitudinal (flow-wise) direction, and subscript 2 to the lateral (cross flow along the surface) direction. ξ_1 and ξ_2 are separation distances between points on the surface, and Λ_1 and Λ_2 are the correlation length scales which strongly depend on frequency (see Ref. 13 for details).

3. Boundary Layer Data

The reader is referred to Ref. 10 for details on how TU-144 data were acquired. Figure 1 shows the flight conditions for which data was acquired. Due to lack of time for this study, only a representative subset of the data was utilized.

TU-144 FLIGHT ENVELOPE

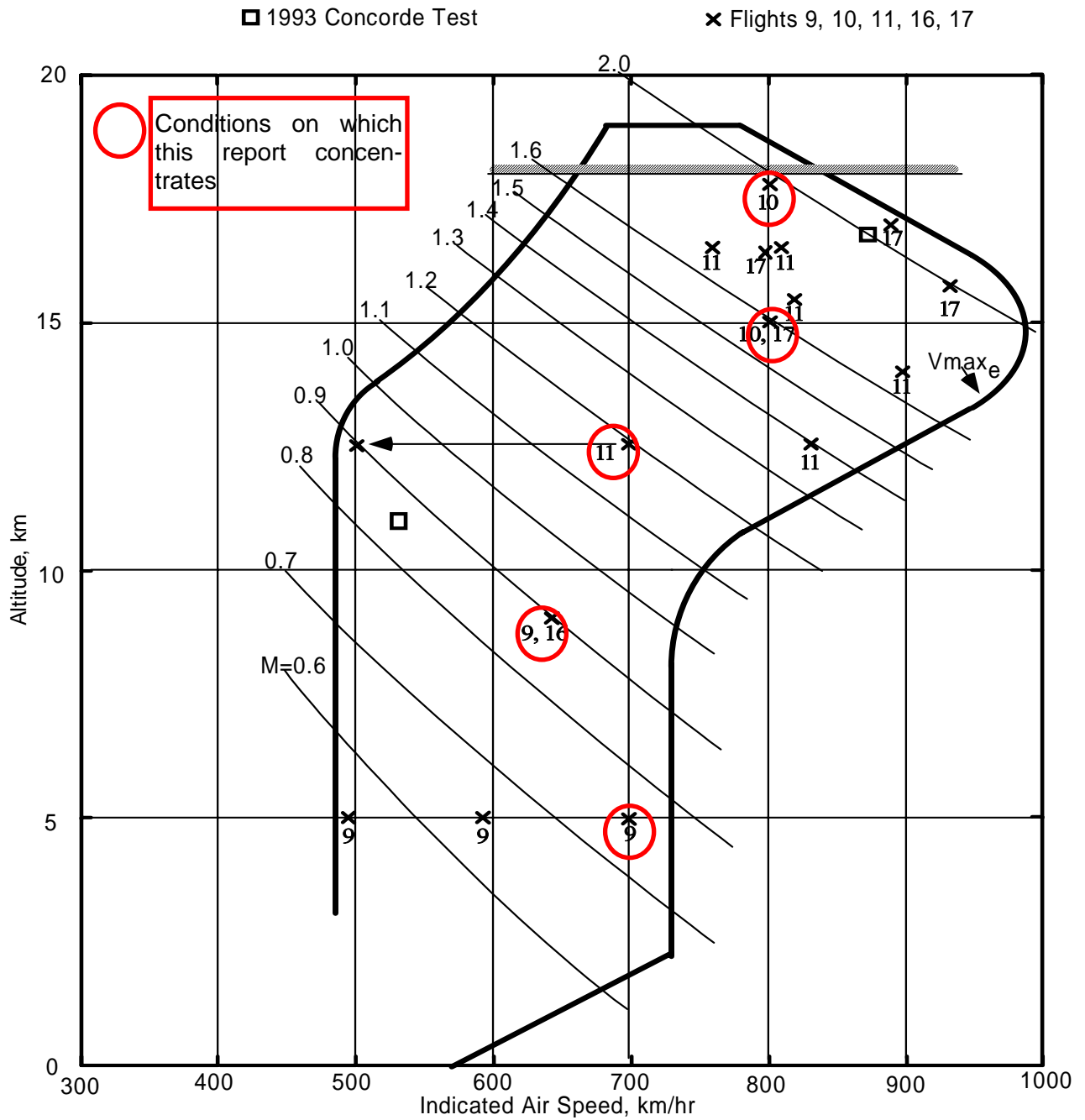□ 1993 Concorde Test   ✖ Flights 9, 10, 11, 16, 17

Figure 1 TU-144 Flight Envelope and Experiment 2.1 Test Points

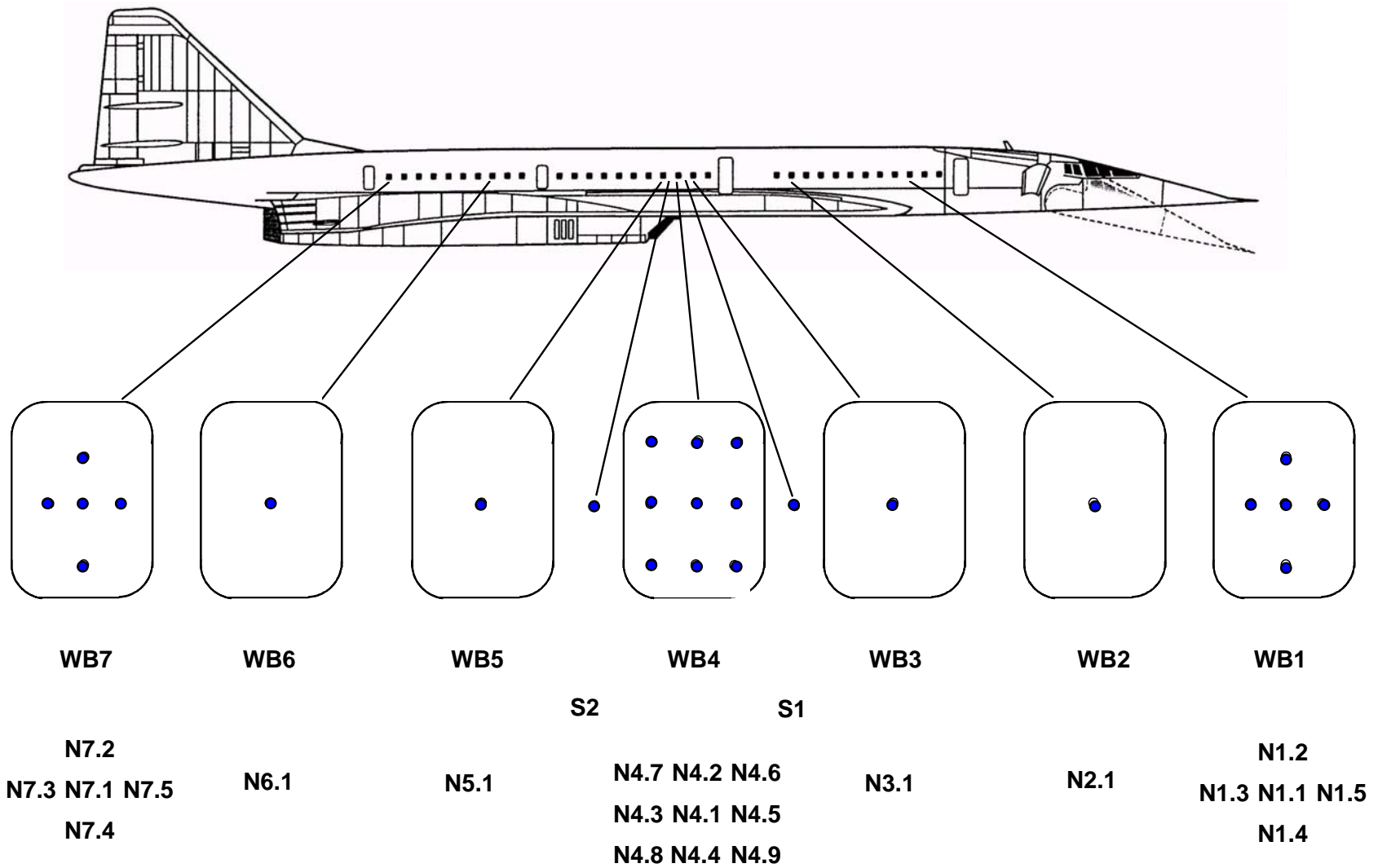Figure 2 shows the layout and nomenclature of the transducers in the window blanks and in the fuselage skin.

Figure 2 Location and Identification of Window Blanks (WB) Instrumented with Kulite Pressure Transducers (N1.1 through N7.5, S1, S2)

WB7   WB6   WB5   WB4   WB3   WB2   WB1

S2   S1

N7.2
N7.3 N7.1 N7.5
N7.4

N6.1

N5.1

N4.7 N4.2 N4.6
N4.3 N4.1 N4.5
N4.8 N4.4 N4.9

N3.1

N2.1

N1.2
N1.3 N1.1 N1.5
N1.4

3.1 Data Analysis

3.1.1 Data Reduction

Pressure level spectra were calculated from one minute samples recorded for each transducer and for each flight condition. These spectra were calculated both on a narrow band and a third octave band basis. The narrow bands have a uniform constant bandwidth of 2.44 Hz; spectral levels reported here were corrected to a 1Hz bandwidth. The third octave band levels were also corrected to a 1 Hz bandwidth for direct comparison between the narrow band and the third OB and to compare levels to some of the published results from previous investigations.

All signal analysis was carried out using the MATLAB software package on an HP-UX work station. Analysis scripts were provided by Dr. Stephen A. Rizzi of NASA Langley Research Center.

3.1.2 Data Normalization

Two forms of data normalization were investigated to help compare between channels and between flight conditions, and for comparing data to previous tests. The first normalization is what is seen in most of the literature on turbulent boundary layer spectral shapes [Ref. 6 and 7]

$$\frac{\Phi(\omega)U_0}{q_0^2\delta^*} vs. \frac{\omega\delta^*}{U_0}$$

where U_0 is the free stream velocity, q_0 is the dynamic pressure, and δ^* is the displacement boundary layer thickness. Efimtsov [Ref. 5] suggests a slightly different normalization for a better collapse of the TsAGI measured data:

$$\frac{\Phi(\omega)}{\rho_w^2 U_\tau^3 \delta} vs. \frac{\omega\delta}{U_\tau}$$

where U_τ is the friction velocity defined by the quotient of wall shear stress over fluid density at the wall ρ_w, and δ is the (velocity deficit) boundary layer thickness. We usually use the Efimtsov normalization in our work.

3.1.3 Kulite Flushness

An exhaustive wind tunnel test was performed by Professor Efimtsov at TsAGI [Ref. 8] to determine the effect sensor flushness would have on the measured results at both subsonic and supersonic speeds. For measured flushness ranging from recessed to protruding, deviation from expected third octave band levels were reported. Variations of less than 2 dB can be expected for sensors deviating less than 20×10^{-6}m from flush, the flushness deviation being measured in the stream-wise direction. The Tu144 flight test Kulite flushness measurements are discussed in Ref. 10. Only four of the Kulites measured this much of a deviation from flushness. However, when these four Kulites were compared to Kulites in the same window blanks (Section 3.1.4), only one of them (N4.1) varied significantly from the average measured SPL within that blank; data from Kulite N4.1 was not used in the auto spectrum analysis in this study.

3.1.4 Outlying Fluctuating Pressure Levels

Within window blank comparisons were conducted by plotting the third octave band levels for all of the sensors within each window blank for 22 selected steady-state flight conditions. Channels that

showed significant deviation from the other channels within the same window blank were noted as deviant and were not used for further auto-spectral analysis (Table 1). Causes for the deviation in measured SPL may included: line noise, damaged sensors, sensor flushness, localized flow disturbances.

Table 1 Outlying Fluctuating Pressure Measurements.

Flight & Run #	Altitude (kft)	Mach #	Window Blank 1 Only	Window Blank 4 Only	Window Blank 7 Only	Central Transducer on all 7 Window Blanks	Bad Channel #'s			
f9r17	16.4	0.648	OK	4.1, 4.9	OK	OK	5	26		
f9r21	16.4	0.877	OK	4.1, 4.9	OK	7.1	5	16	26	
f9r23	13.1	0.563	OK	4.1, 4.9	OK	OK	5	26		
f10r29	45	1.6	OK	4.1, 4.4, 4.5	7.5	4.1	5	8	9	30
f10r31	46.6	1.6	OK	4.1, 4.5	7.5	4.1	5	9	30	
f10r33	55.4	1.95	OK	4.1	7.5	4.1	5	30		
f10r34	55.4	1.95		4.1, 4.3		4.1	5	7		
f10r35	56.8	1.95	OK	4.1, 4.3	7.5	4.1	5	7	30	
f10r36	56.8	1.95		4.1, 4.3		4.1	5	7		
f10r37	56.8	1.95		4.1, 4.3		4.1	5	7		
f11r40	52.5	1.8	OK	4.1, 4.5	OK	4.1	5	9		
f11r42	54.5	1.7	OK	4.1, 4.3, 4.5	OK	4.1	5	7	9	
f11r44	50.9	1.7	OK	4.1, 4.5	OK	4.1	5	9		
f11r48	41.3	1.4	OK	4.1, 4.5	OK	4.1	5	9		
f11r50	41	1.2	1.2	4.1	OK	4.1	5	22		
f11r53	16.4	0.75	OK	4.1	OK	4.1	5			
f17r66	53.1	2	OK	4.3	OK	4.1	5	7		
f17r68	55.4	2.05	OK	4.3	OK	4.1	5	7		
f17r70	53.8	1.75	OK	4.1, 4.3, 4.5	OK	4.1	5	7	9	
f17r71	49.2	1.6	N/A	4.3	N/A	OK	7			

Single sensors located on window blanks by themselves (blanks 2,3,5, and 6) and the two sensors on the skin (S1 and S2) were more difficult to compare for outlying SPL. Normalized levels plotted for sensors down the length of the plane could be used to some extent. However, the uncertainties in the data were too great for meaningful interpolations so that data from single sensors were not included in the auto-spectral analyses in this report.

4. Data Correction

A correction was added to all auto-spectra of boundary layer surface pressure fluctuations. It accounts for the lack for spatial turbulence scale resolution of the transducer at high frequencies, according to Corcos [Ref. 14]. Ideally, one would follow the theory presented in Ref. 14 and develop the correction formula based on the transducer's actual geometry as shown in Figure 3. This was attempted but abandoned due to mathematical complexity and because an assumption made in the theory was not satisfied which says that the sensing areas on the transducer face contribute to the total instantaneous measured pressure without phase shift. In the present case, the 12 small circles in Figure 3 are just through holes to a small volume behind the face containing a single strain gage to which each hole contributes with unknown phase shifts. Instead, a circular transducer sensing surface was assumed in order to use the calculated results in Ref. 14.

Then, the crucial question is what transducer radius to use in the correction procedure. Efimtsov [Ref. 8] stated that the transducer he investigated in the wind tunnel behaved with regard to a Corcos correction as if its diameter was about 8 mm, i.e. double its outer diameter. However, when we used a radius of 4mm for the Corcos correction, the high frequency behavior of the corrected spectra became unreasonable: instead of a more or less constant roll-off slope on a log-log plot, the spectrum started to curve upwards again at higher frequencies. Instead, Philippe Spalart [Ref. 15] suggested that an equivalent radius be determined on the basis of calculating root-mean-square distances from points on the sensing device to the center. With a ring, the root-mean-square equals the radius of the ring. With a disk, it is the disk radius divided by square root of two. Therefore, we multiplied the radius of the circle on which the sensing holes are located (the "ring") by $\sqrt{2}$ resulting in $\frac{0.104}{2}\sqrt{2} \; inches = 1.87 \; mm$. This resulted in reasonable corrections. An example is shown in Figure 4.
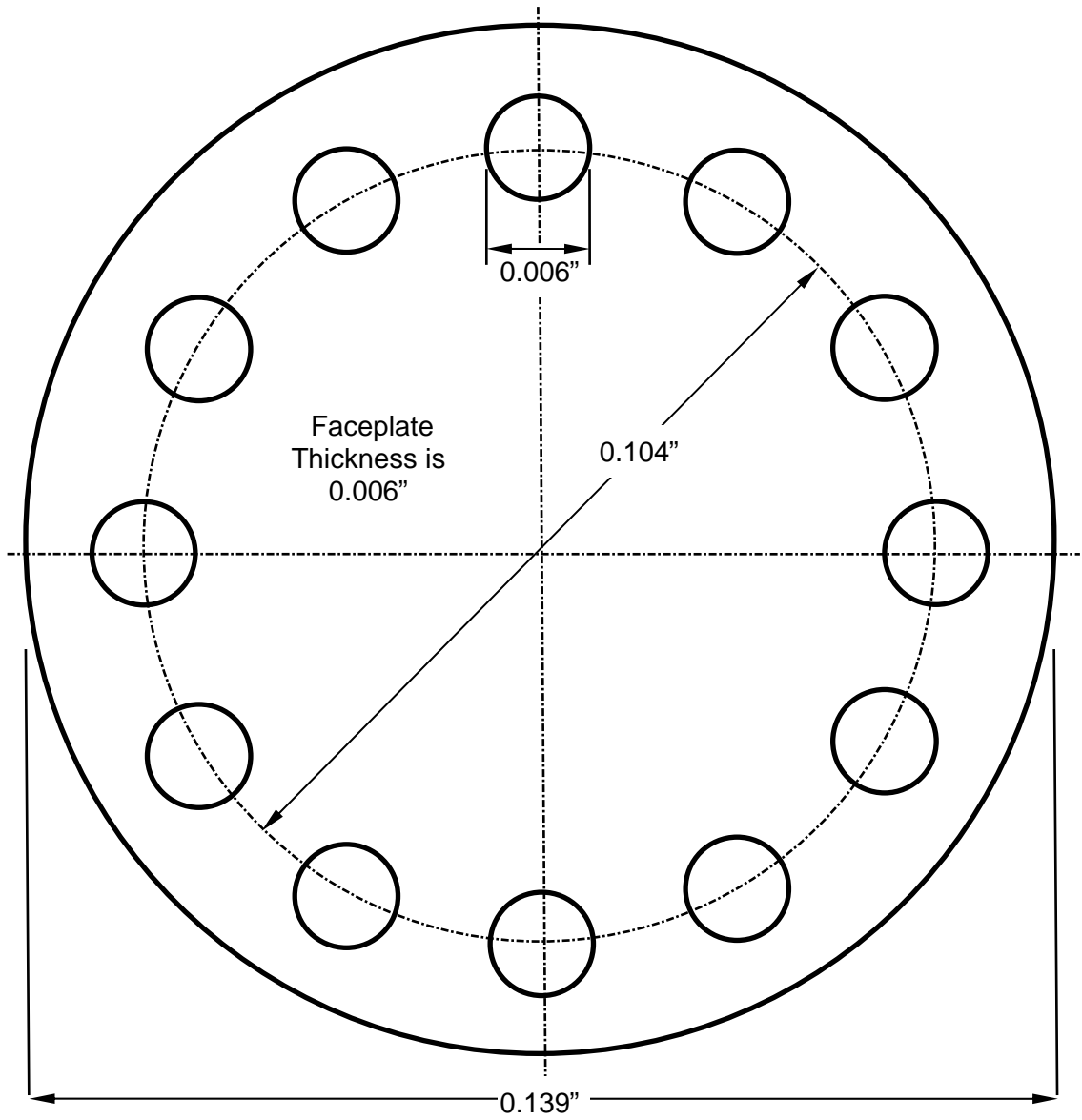
Figure 3 Geometry of Face of Kulite Transducer XCS-190
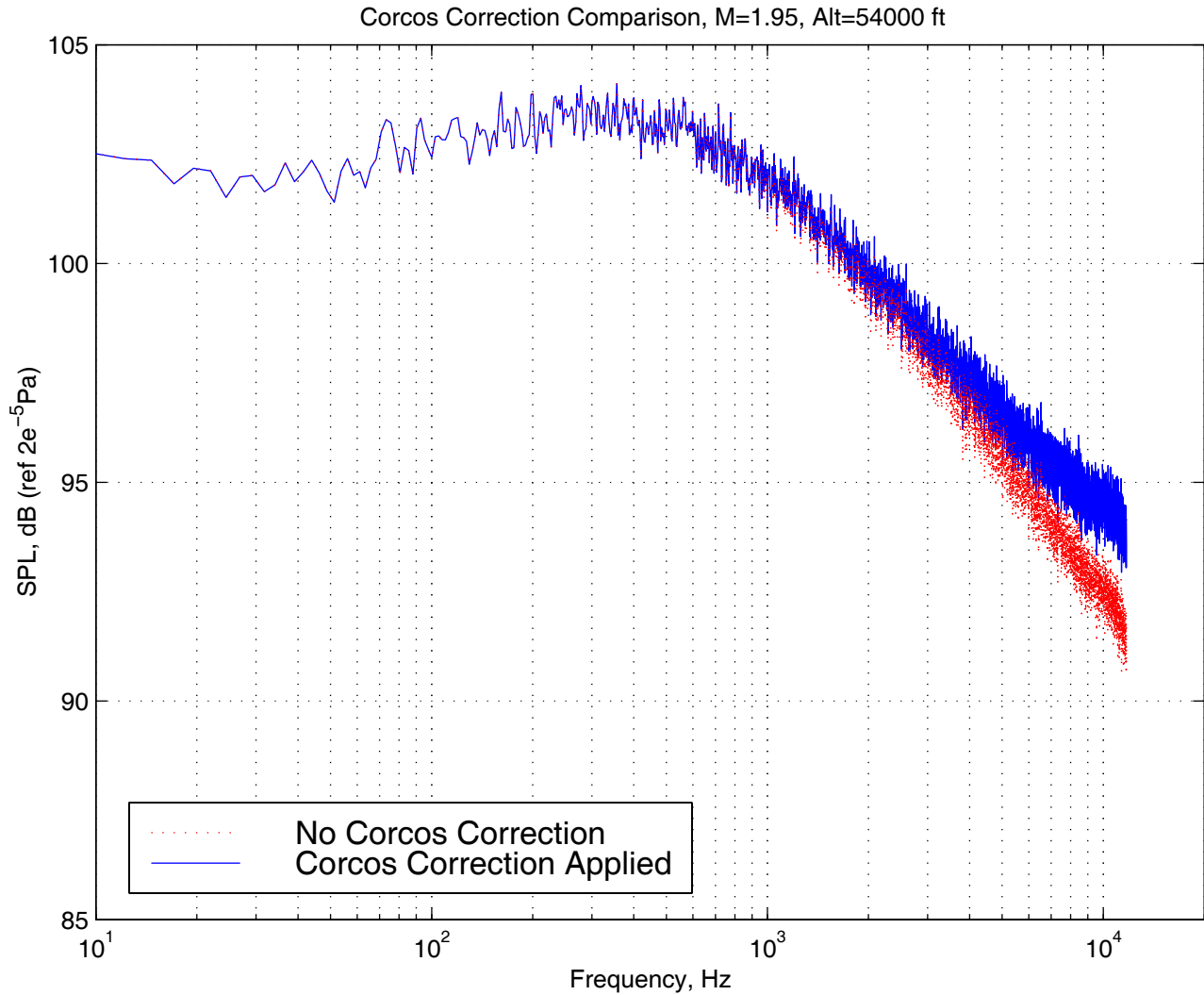
Figure 4 Example of a Corcos Correction

5. Comparisons of Measured Data with Models

5.1 Auto-Spectra

Figure 5 and Figure 6 (absolute levels) and Figure 7 (normalized) show comparisons between all the models and the measured data, for window blank 4 (in the middle of the fuselage). The Efimtsov and Goodwin models are the most accurate for predicting the measurements on the Tu144. Figure 8 and   Figure 9 contain comparisons of TU-144LL data with Efimtsov and Goodwin predictions for window blanks 1, 4, and 7. These data are typical of what we saw: at subsonic speeds, the Efimtsov model predicts well, and at supersonic speeds both the Efimtsov and Goodwin models provide good estimates. All models but Efimtsov's predict a steeper high frequency roll-off than the TU-144LL data (which has been corrected for transducer size). Efimtsov's model was chosen for further adjustment, as it had the best overall match to the measured data.
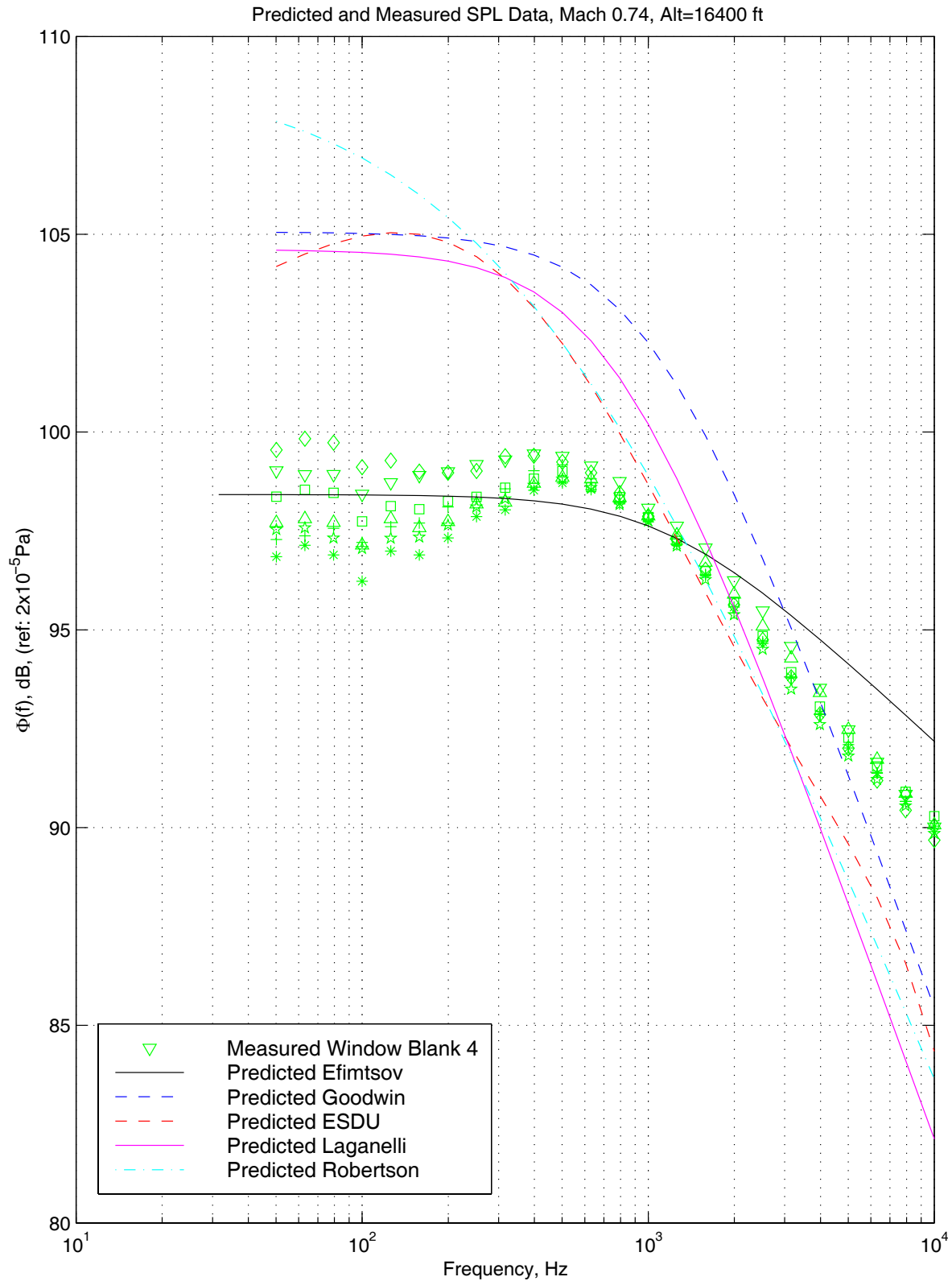
Figure 5 Comparison of the Five Investigated Models, Robertson, ESDU, Laganelli, Good-win, and Efimtsov, and Measured Data on Tu144 (M 0.74, 16,400 ft, Window Blank 4).
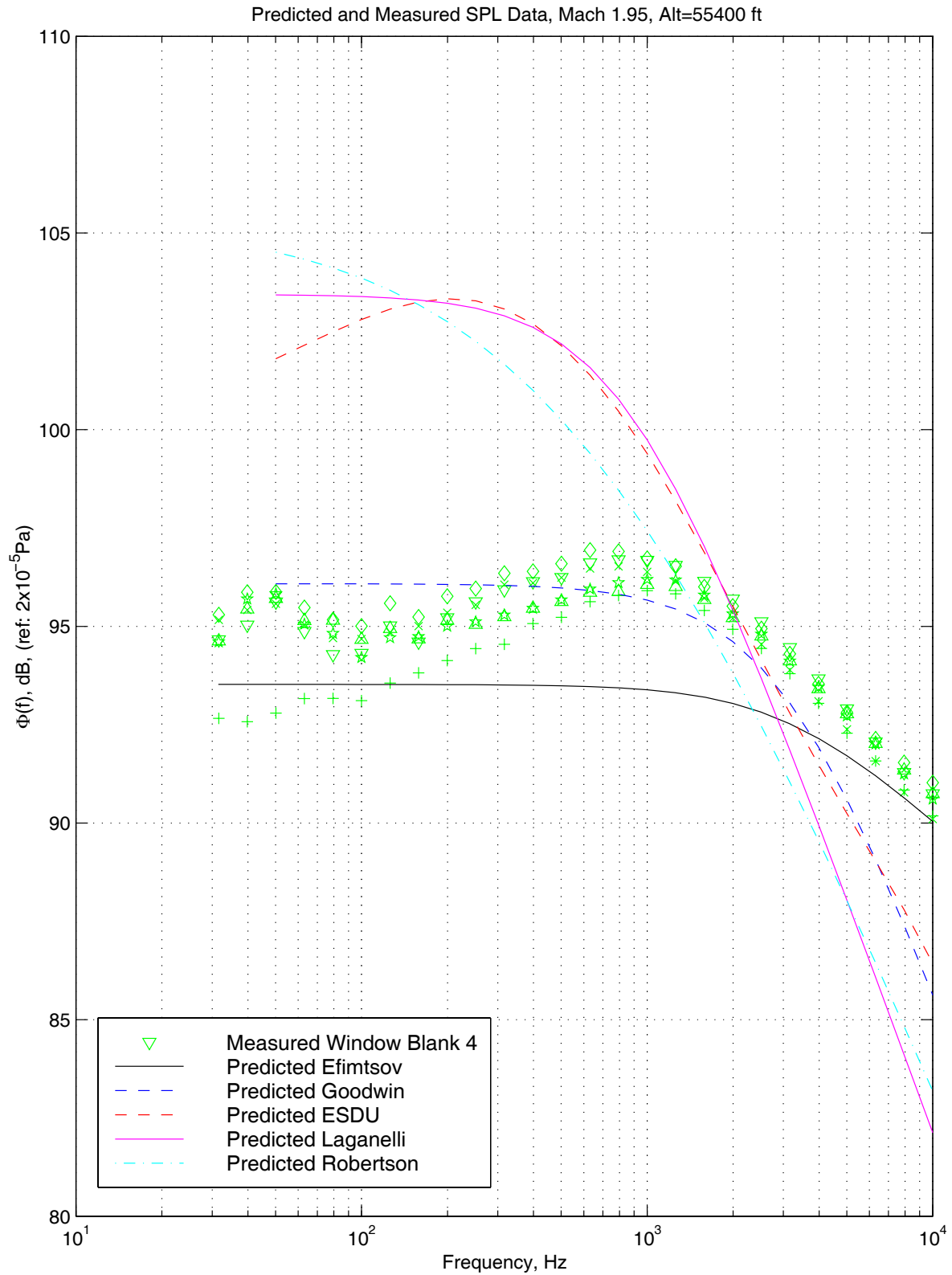
Figure 6 Comparison of the Five Investigated Models, Robertson, ESDU, Laganelli, Goodwin, and Efimtsov and Measured Data on Tu144 (M 1.95, 55,400 ft, Window Blank 4).
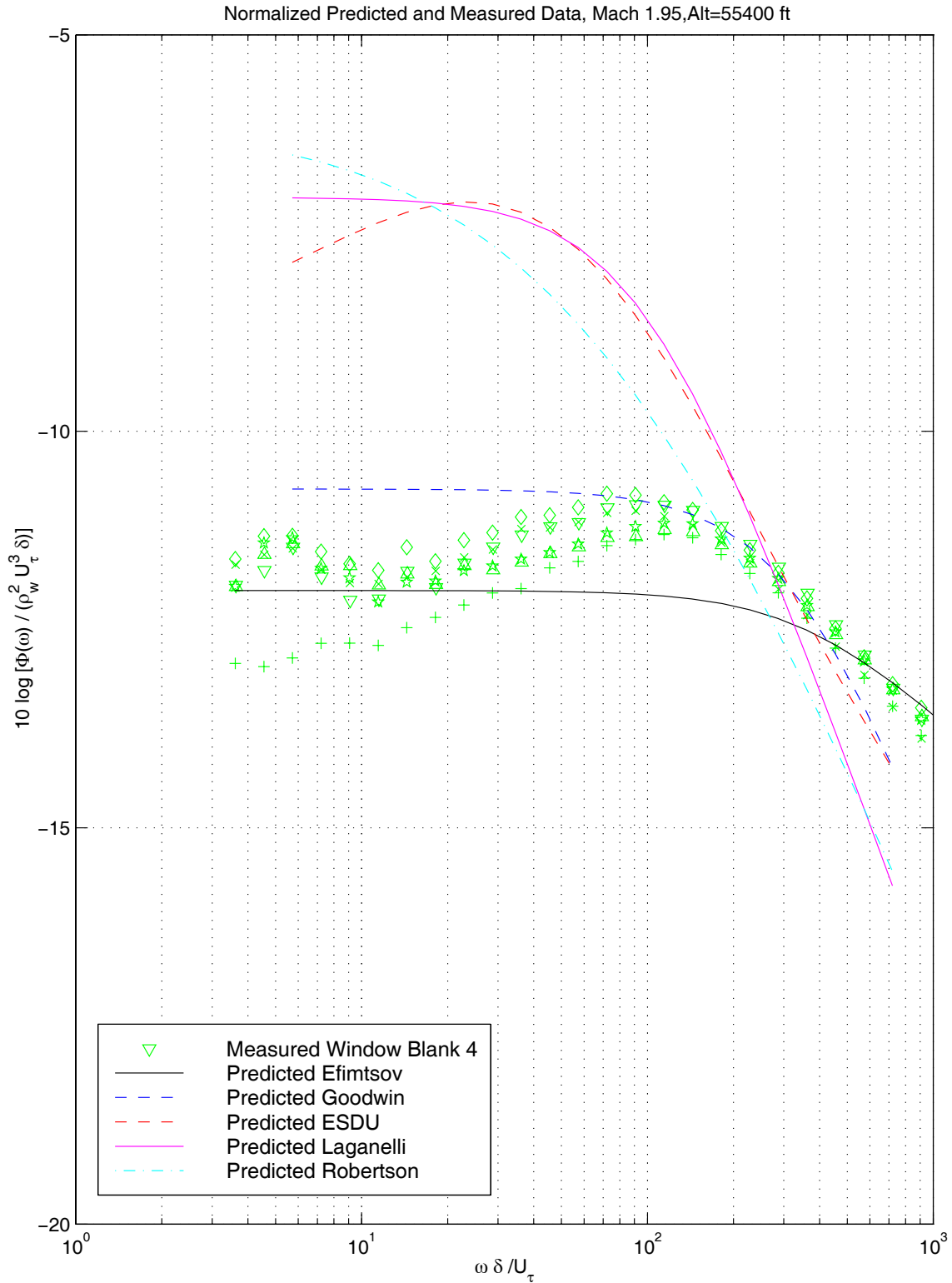
Figure 7 Normalized Comparison of the Five Investigated Models, Robertson, ESDU, Laganelli, Goodwin, and Efimtsov and Measured Data on Tu144 (M 1.95, 55,400 ft, Window Blank 4).
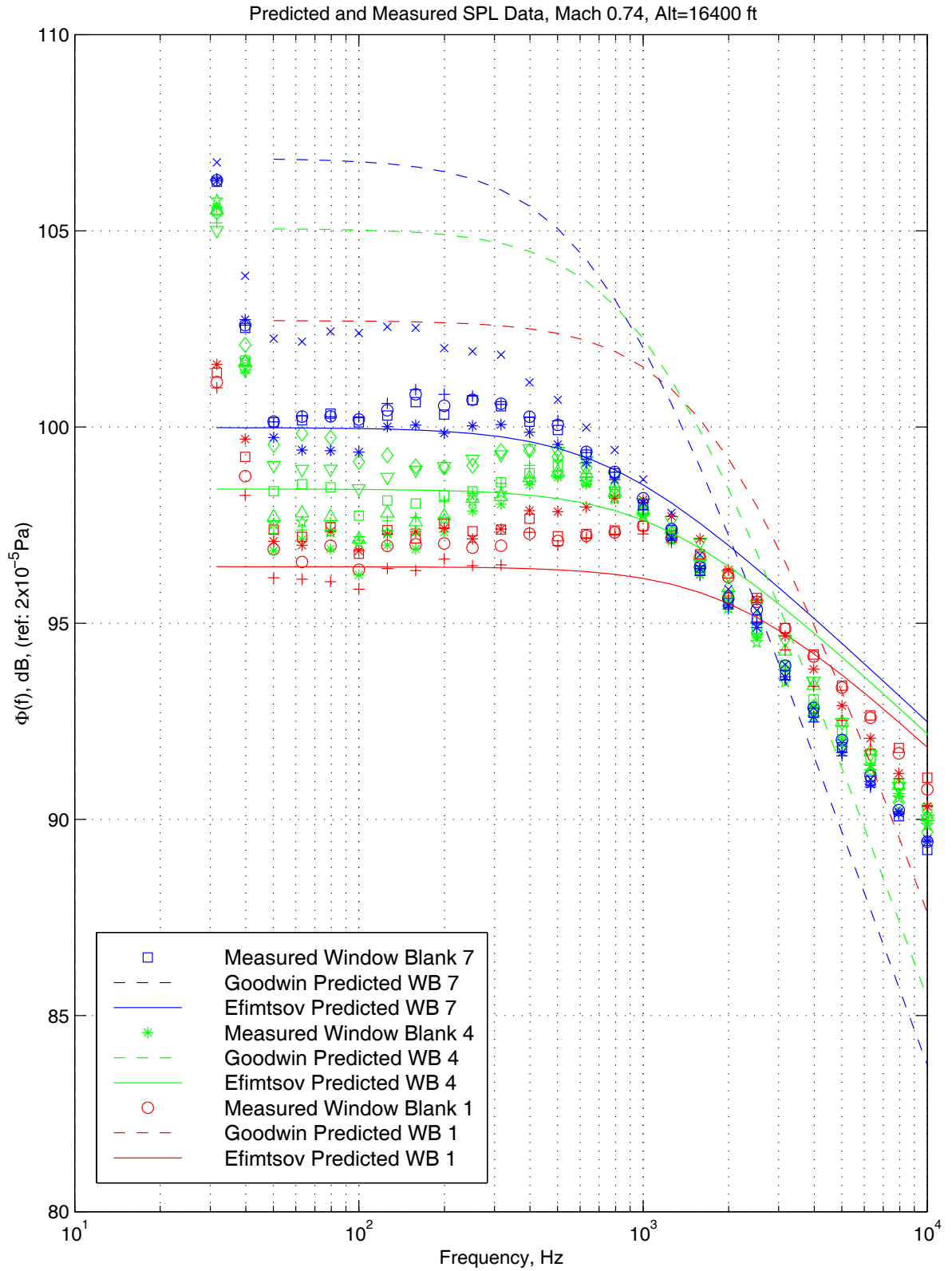
Figure 8 Closer Comparison of Efimtsov and Goodwin Models and In-Flight SPL Data (M 0.74, 16,400 ft, Window Blanks 1, 4, and 7)
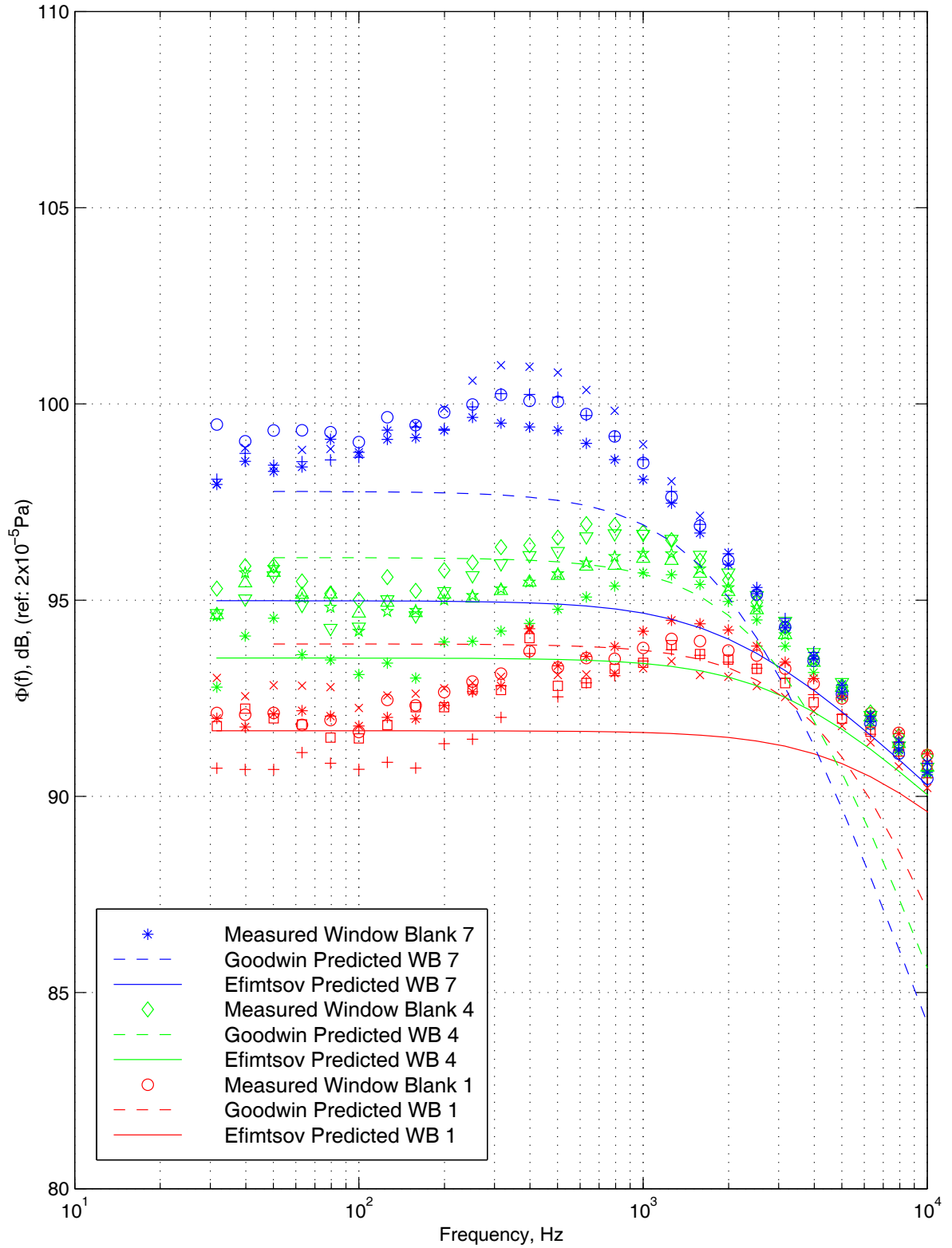
Figure 9 Closer Comparison of Efimtsov and Goodwin Models and In-Flight SPL Data (M 1.95, 55,400 ft, Window Blanks 1, 4, and 7)

5.2 Cross-Functions

All measured cross-functions presented here were computed using the entire 1 minute time history records available in the TU-144LL data. The cross-correlations use the entire frequency band available: from about 2 Hz to 11.2 KHz. The cross-spectra were calculated on a narrow band basis (2.44 Hz) and then averaged over one third octave bands, corrected to a 1 Hz bandwidth.

A correction for transducer size was not applied (analogous to the Corcos [Ref. 14] correction for auto spectra). This would have required applying digital filters to amplify the high frequency portion of the two input time histories being cross-analyzed.

5.2.1 Cross-Correlations

Cross-correlations are defined by

$$\varphi\left(\mathbf{x},\boldsymbol{\xi},\tau\right)=\frac{\lim_{T\to\infty}\frac{1}{2T}\int_{-T}^{T}p(\mathbf{x},t)p(\mathbf{x}+\boldsymbol{\xi},t+\tau)d\tau}{\left[p(\mathbf{x})\right]_{rms}\left[p(\mathbf{x}+\boldsymbol{\xi})\right]_{rms}}$$

where p is the fluctuating surface pressure, $\mathbf{x}$ is a location on the fuselage, $\boldsymbol{\xi}=(\xi_1,\xi_2)$ is a spatial separation vector, t is the time, and τ is a time delay. In the following text the location on the fuselage is omitted and implied by context.

All the cross-correlations exhibit expected behavior:

- For longitudinal separations (stream-wise) the peak occurs at a time delay corresponding to the convection velocity, and the magnitude at the peak decreases with increasing separation. The cross-correlations are well behaved and show discernible correlations even at the largest separation distance of 1741 mm (5.7 feet). The convection velocity can be calculated by dividing the separation distance into the time delay of the correlation peak. The result is shown in Figure 19.

- For lateral separations, the peaks occur close to zero time delay.

- For equal separation distances, the magnitude for longitudinal separations is much greater than for lateral separations.

The angle of local surface stream lines was not known; therefore, no corrections have been applied for the flow not being aligned with the transducers. For some lateral separations, the peak occurs slightly before zero time delay which may be explained by the flow direction not being perpendicular to the line between the transducers.

5.2.1.1 Cross-Correlations at Front Fuselage

Figure 10 and Figure 11 show cross-correlations with longitudinal (stream-wise) separation distance as a parameter, for transducers on window blank 1.

Figure 12 and Figure 13 show cross-correlations, with lateral (cross stream) separation distance as a parameter, for transducers on window blank 1.
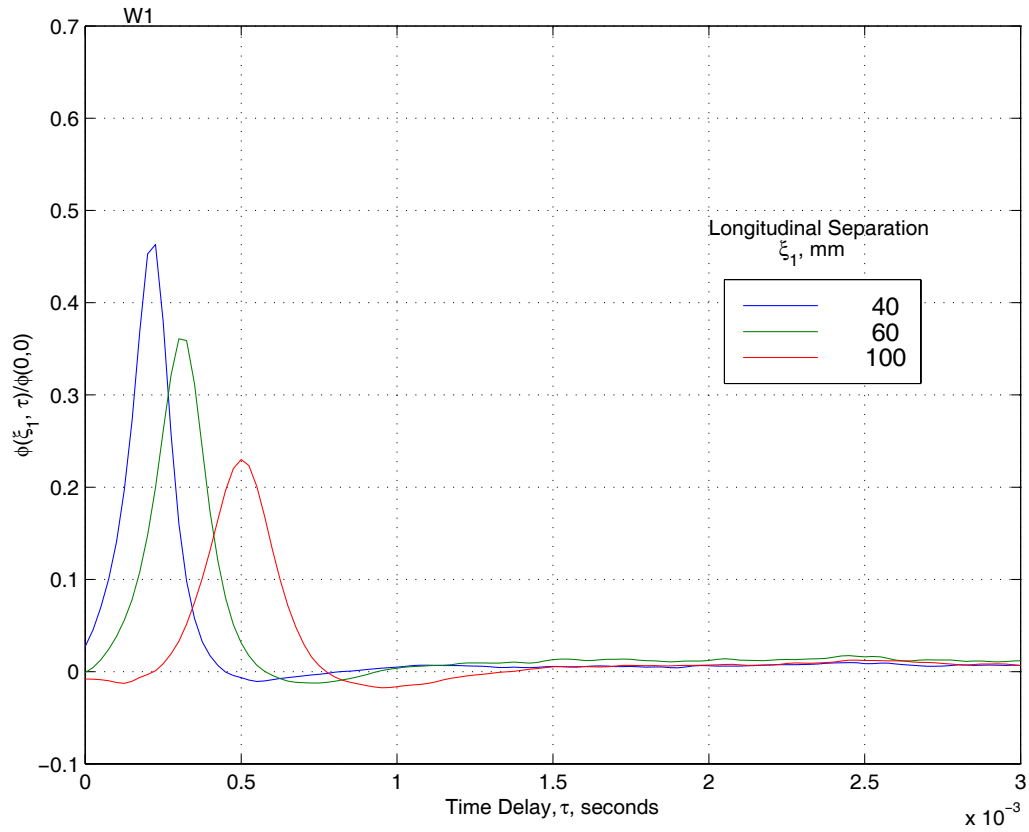
Figure 10 Cross-correlations - Longitudinal, Window Blank 1, Wide Band, Mach 0.74
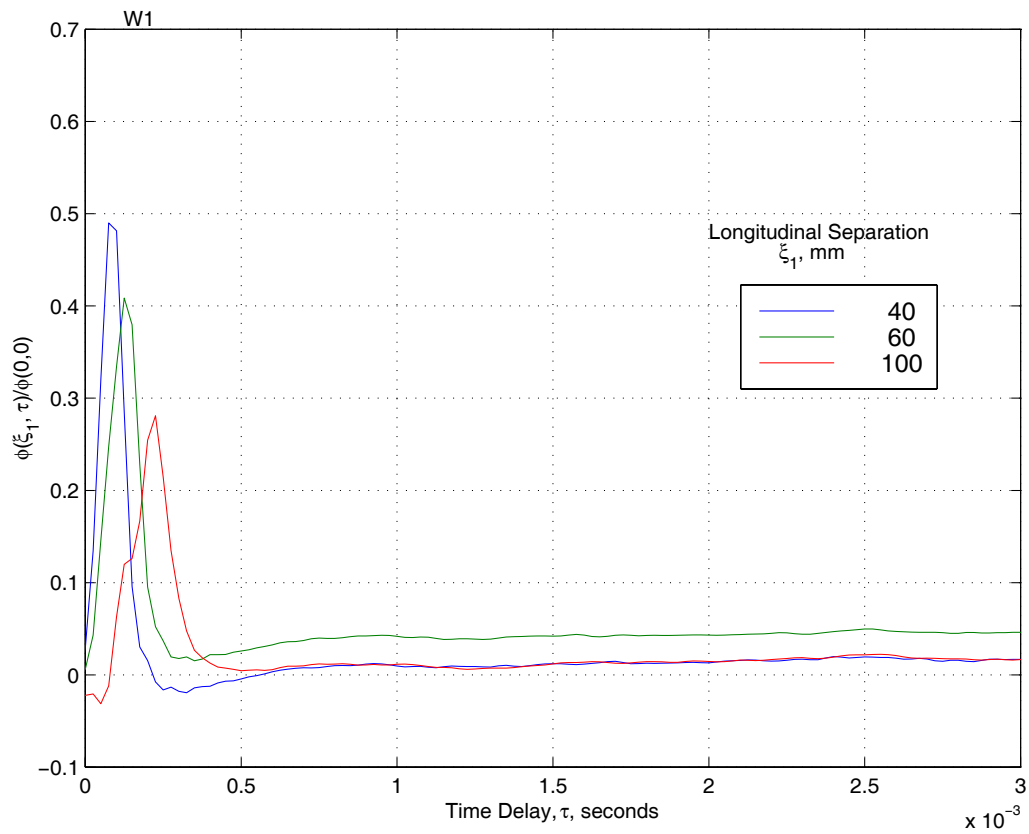
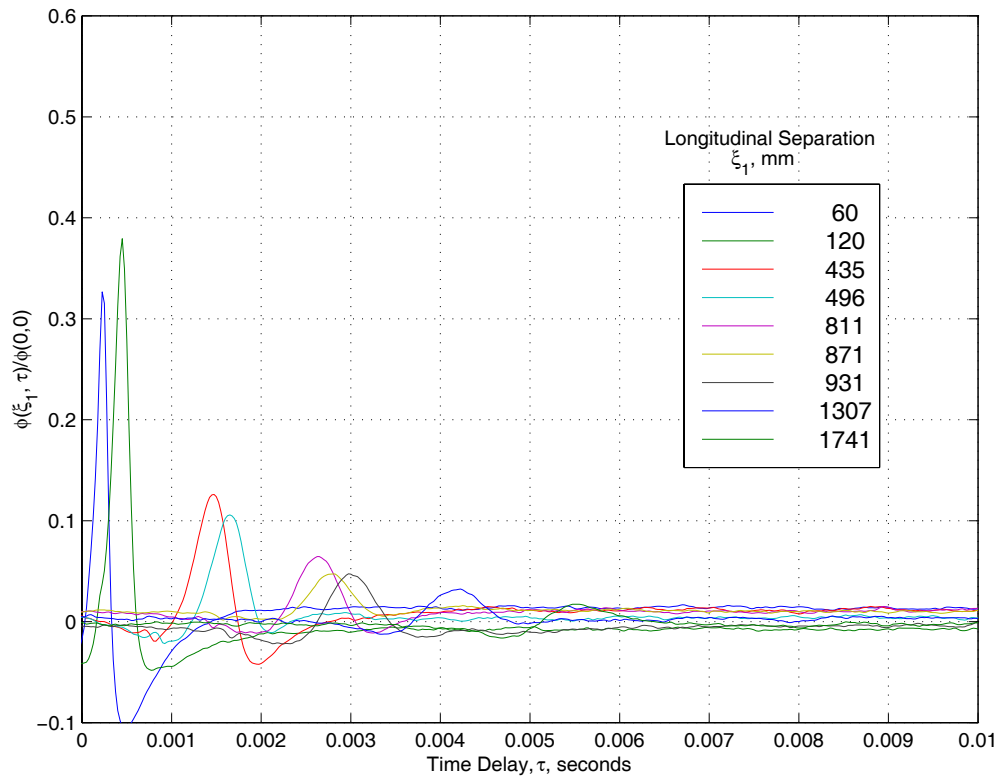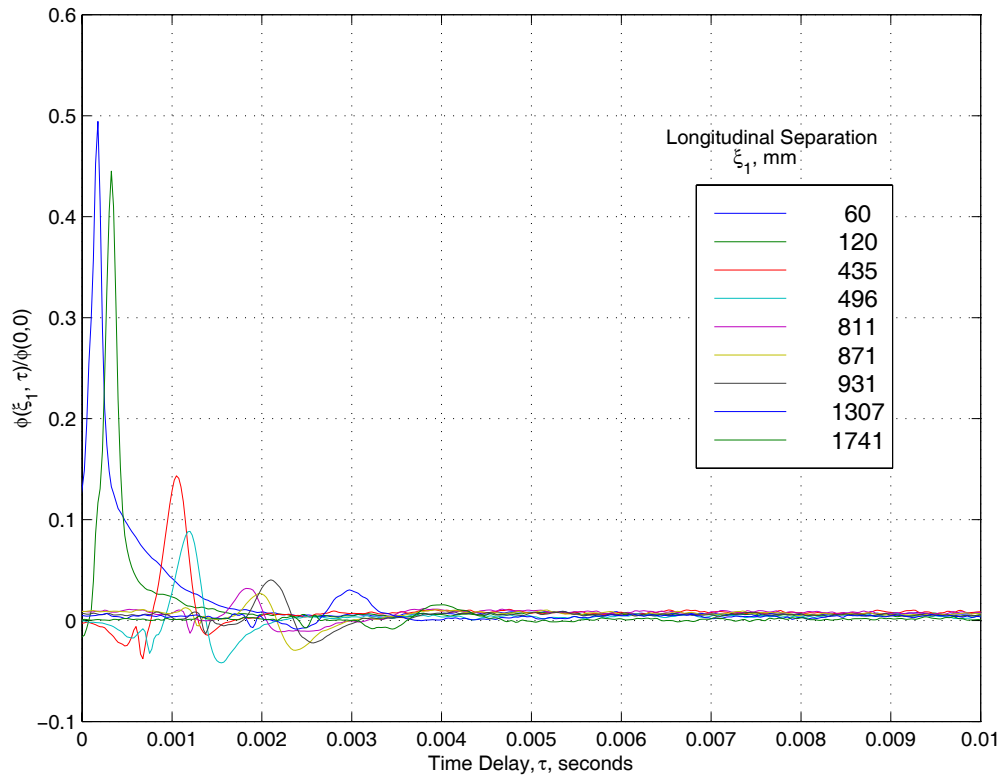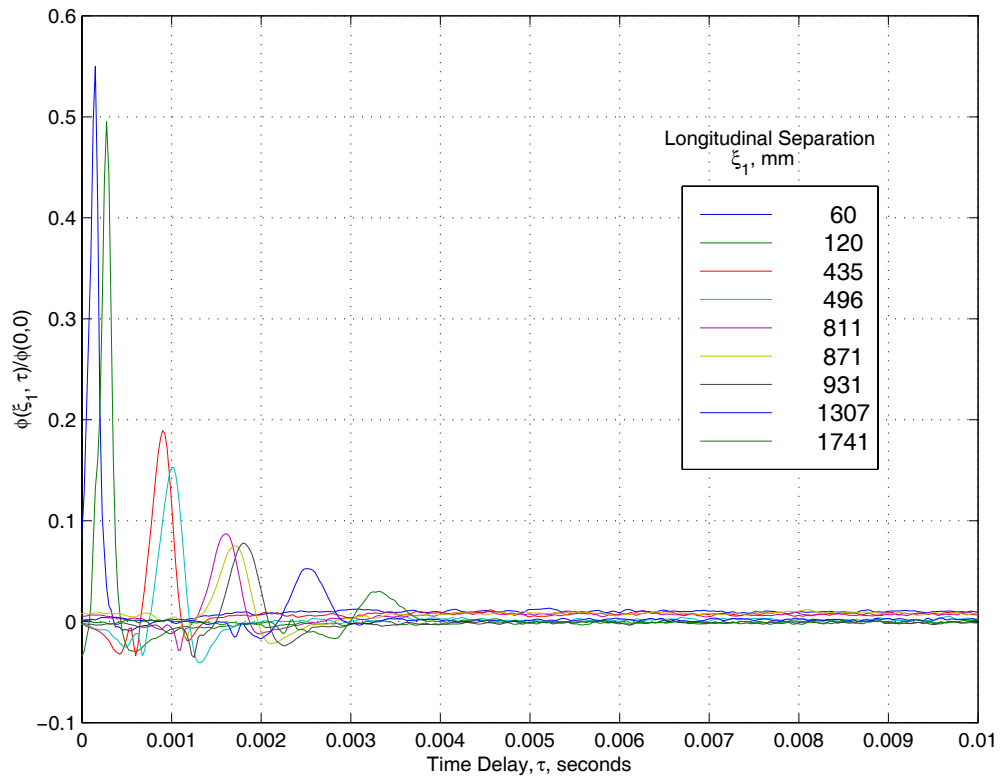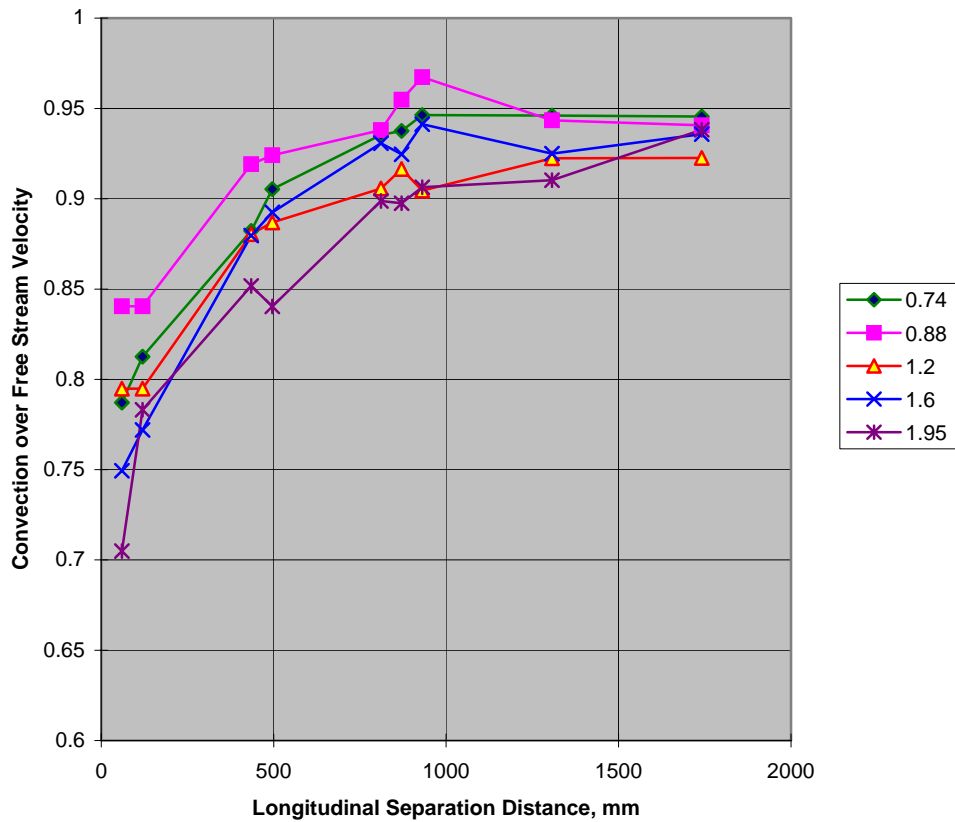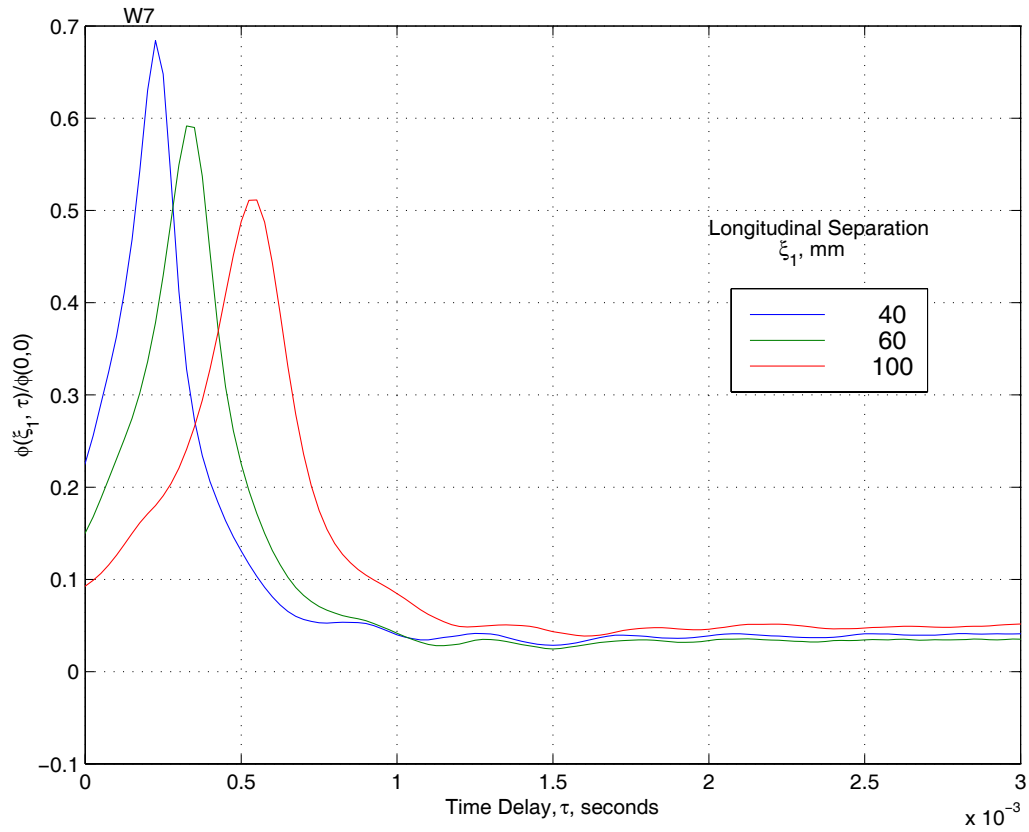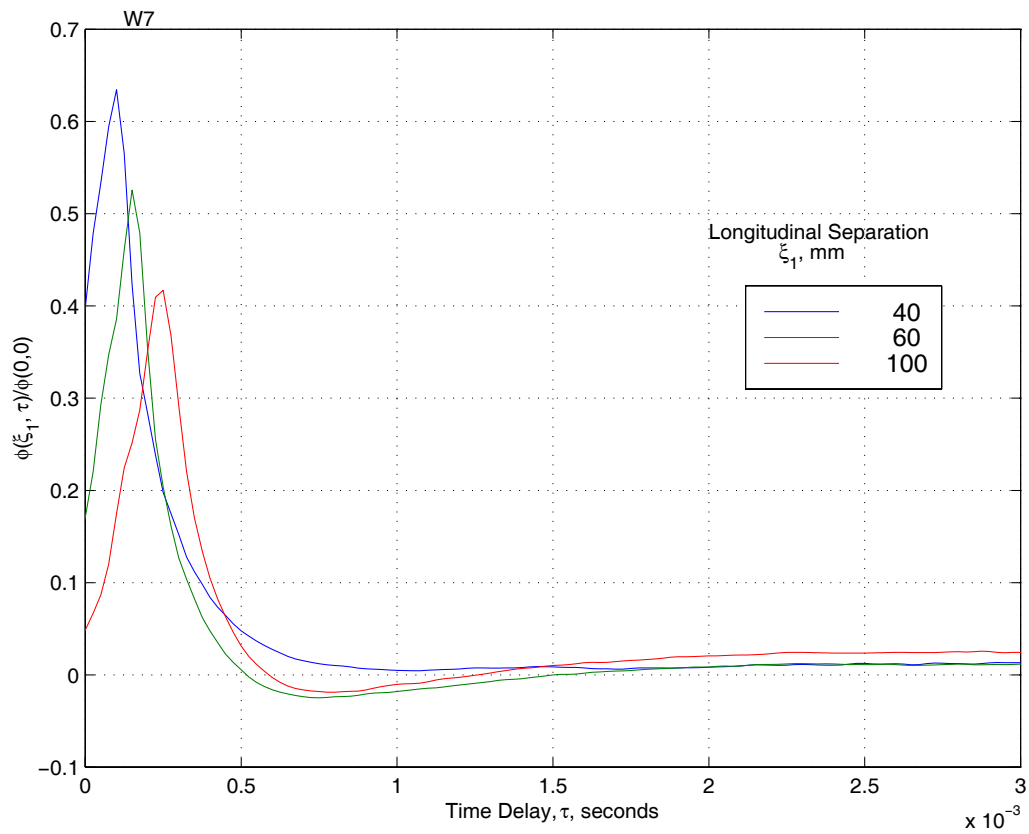**Figure 11 Cross-correlations - Longitudinal, Window Blank 1, Wide Band, Mach 1.95**
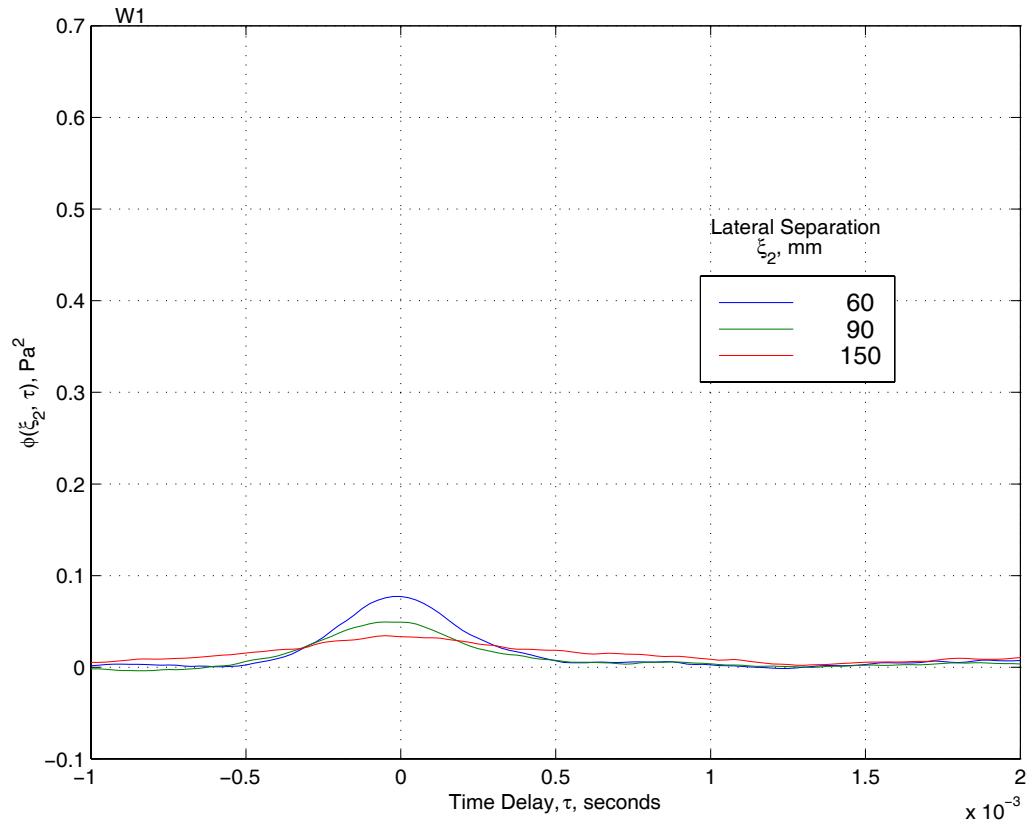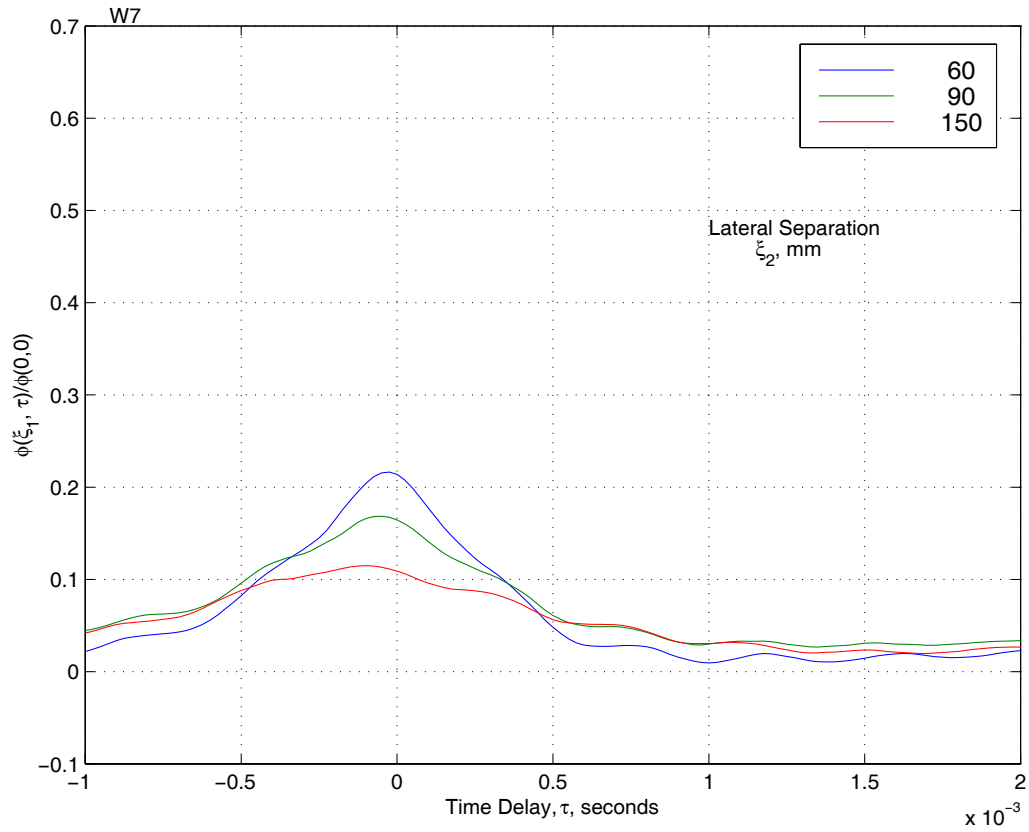
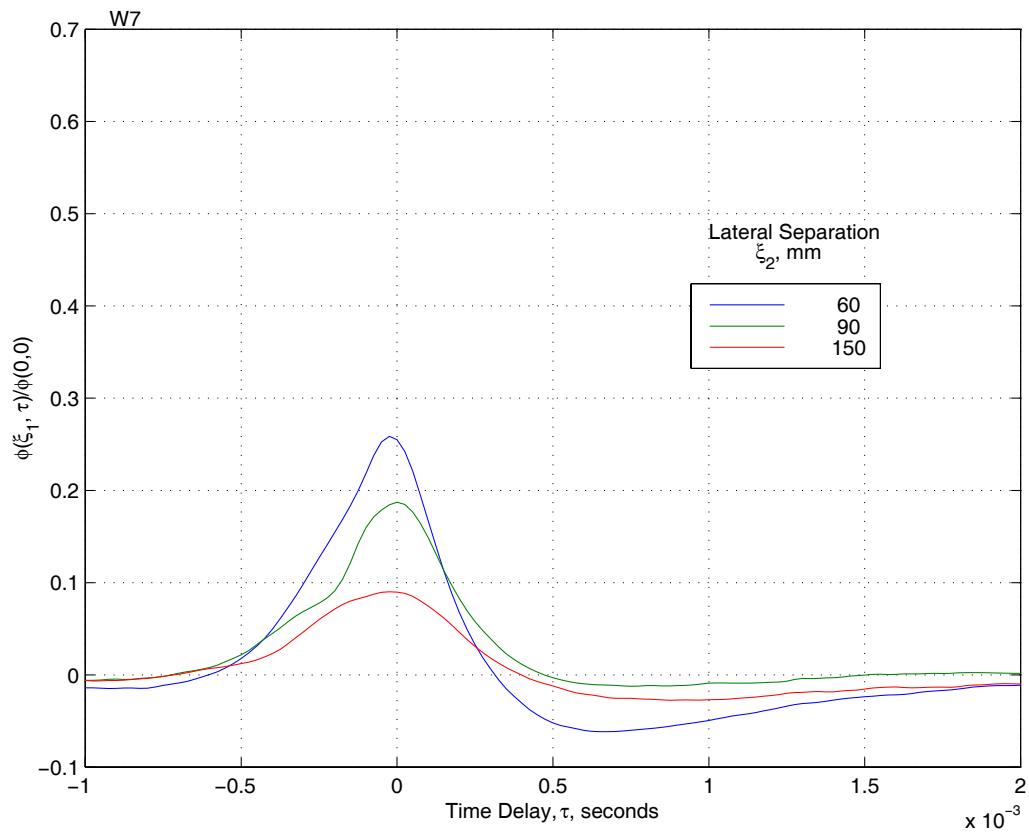**Figure 12 Cross-correlations - Lateral, Window Blank 1, Wide Band, Mach 0.74**
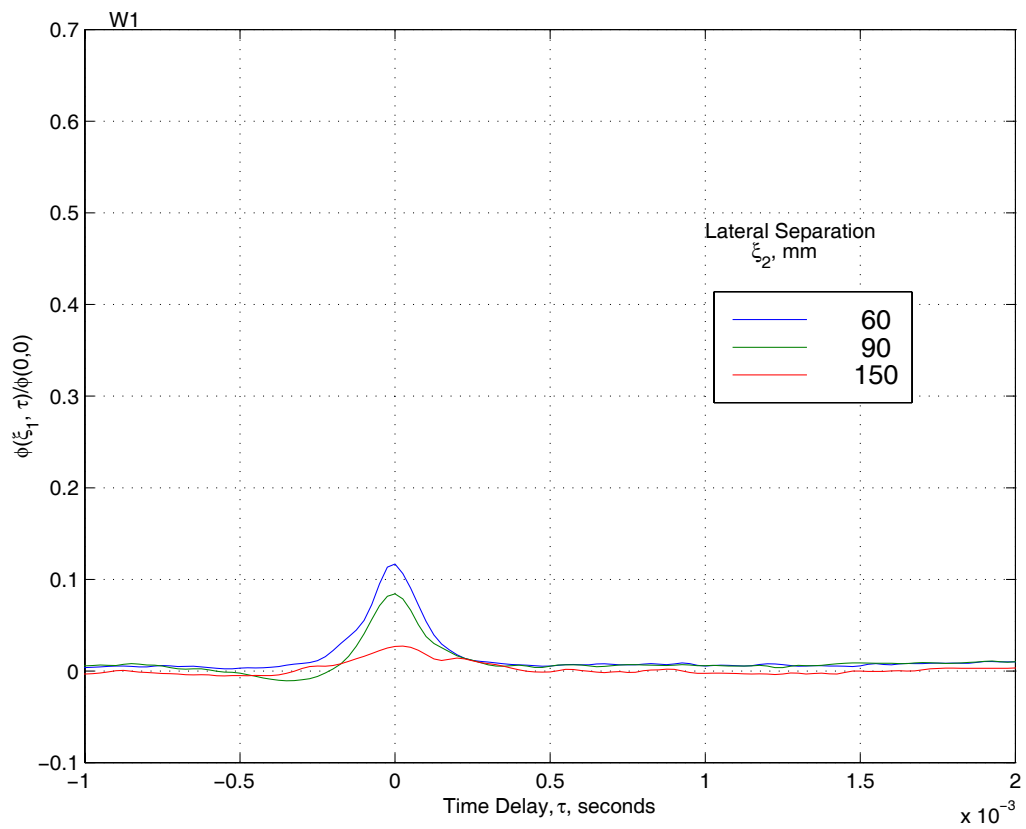
Figure 13 Cross-correlations - Lateral, Window Blank 1, Wide Band, Mach 1.95

5.2.1.2 Cross-Correlations at Center Fuselage

Figure 14 through Figure 18 show cross-correlations which are functions of time delay, with separation distance as a parameter, for transducers on window blanks 3 through 5, and between them.

The increase in peak value of the correlation going from 60mm to 120mm spacing, as shown in Figure 14 and in Figure 16, can be explained by the inaccurate auto spectrum measured on transducer N4.1 (discussed in Section 3.1.3).
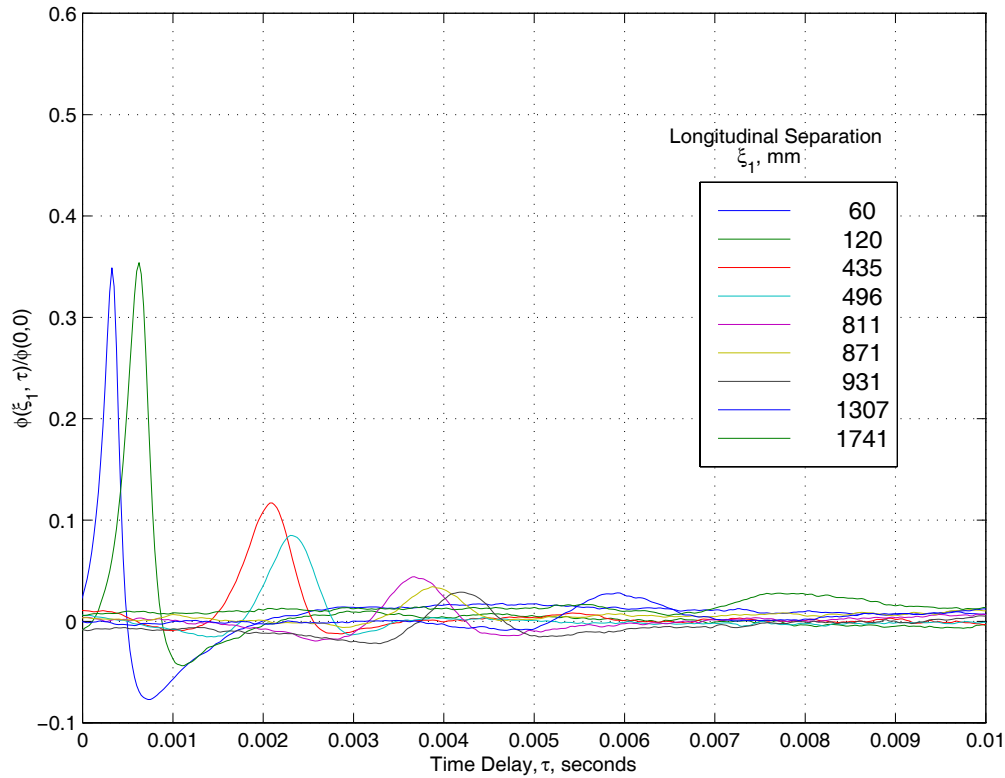
**Figure 14
Cross-correlations -
Longitudinal,
Window Blanks
3/4/5, Wide
Band, Mach
0.74**
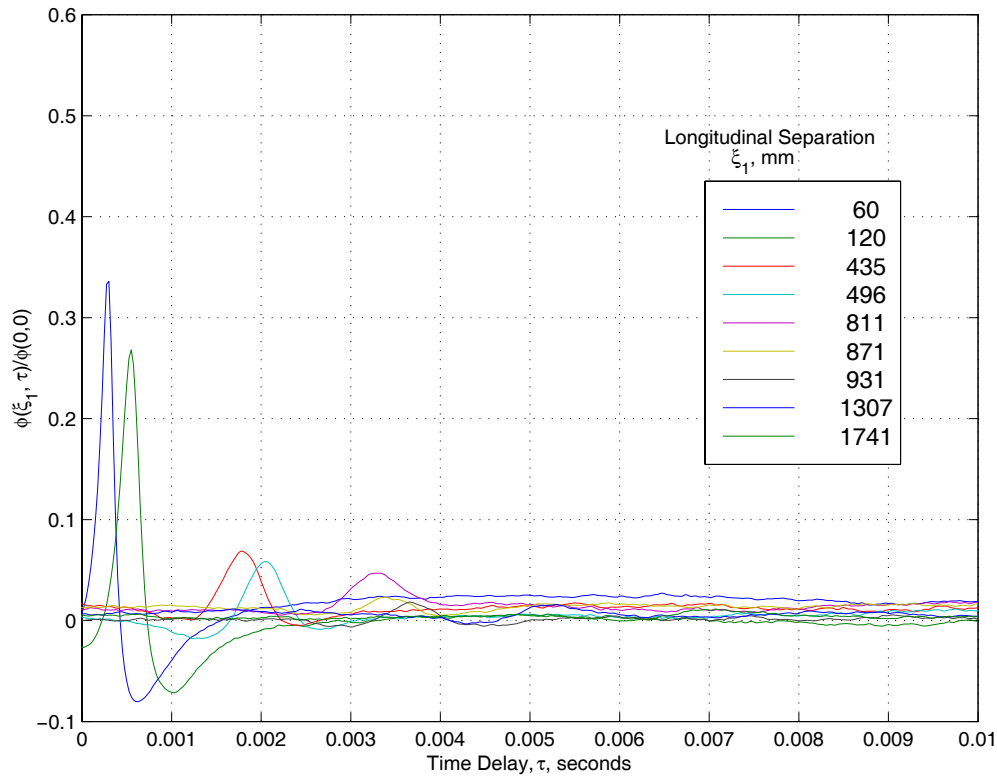
**Figure 15
Cross-correlations -
Longitudinal,
Window Blanks
3/4/5, Wide
Band, Mach
0.88**

**Figure 16
Cross-correlations -
Longitudinal,
Window Blanks
3/4/5, Wide
Band, Mach 1.2**

Figure 17 Cross-correlations - Longitudinal, Window Blanks 3/4/5, Wide Band, Mach 1.6

Figure 18 Cross-correlations - Longitudinal, Window Blanks 3/4/5, Wide Band, Mach 1.95

21

Figure 19 Convection Velocity as a Function of Separation Distance and Mach Number, Window Blanks 3/4/5

5.2.1.3 Cross-Correlations at Rear Fuselage

Figure 20 and Figure 21 show cross-correlations, with longitudinal separation distance as a parameter, for transducers on window blank 7.

Figure 22 and Figure 23 show cross-correlations, with lateral separation distance as a parameter, for transducers on window blank 7.

Figure 20 Cross-correlations - Longitudinal, Window Blank 7, Wide Band, Mach 0.74

Figure 21 Cross-correlations - Longitudinal, Window Blank 7, Wide Band, Mach 1.95

Figure 22 Cross-correlations - Lateral, Window Blank 7, Wide Band, Mach 0.74

Figure 23 Cross-correlations - Lateral, Window Blank 7, Wide Band, Mach 1.95

5.2.2 Cross-Spectra

The cross-spectral density is defined as the Fourier transform of the cross-correlation. In Section 5.2.1, the cross-correlation is defined with normalization. Here, we define the cross-spectrum without normalization:

$$\Phi\left(\mathbf{x},\xi,f\right)=\int_{-\infty}^{\infty}\left[\lim_{T\to\infty}\frac{1}{2T}\int_{-T}^{T}p(\mathbf{x},t)\,p(\mathbf{x}+\xi,t+\tau)dt\right]e^{-2\pi i f\tau}d\tau$$

where f is frequency. Again, the location vector $\mathbf{x}$ is omitted below and is implied by context (window blank).

As shown in Figure 2, window blanks 1 and 7 only offer three longitudinal and two lateral separation distances. The cluster of transducers in and between window blanks 3 to 5 offer a much greater range of longitudinal separations, but only two in the lateral direction.

All cross-spectra have dimensions Pascal-squared per Hertz. Ref. 13 was used to compute the predicted values.

5.2.2.1 Cross-Spectra at Forward Window Blank

Figure 24 through Figure 29 contain measured and predicted cross-spectral values as a function of longitudinal separations with frequency as the parameter, one set for a mach number of 0.74, another set for mach 1.95. Measured magnitudes are generally lower than predicted ones. At the subsonic Mach number, decay rates with distance are comparable. At the supersonic speed, the measured cross spectra show little decay. Phases compare well in all cases.

Figure 30 and Figure 31 show cross-spectral comparisons (magnitude only) for laterally separated transducers. Again, the measured magnitudes and decay rates are lower than the predicted ones. At Mach 1.95, predicted cross-spectral values coincide for all frequencies; the measured values tend to cluster closer together than at Mach 0.74.
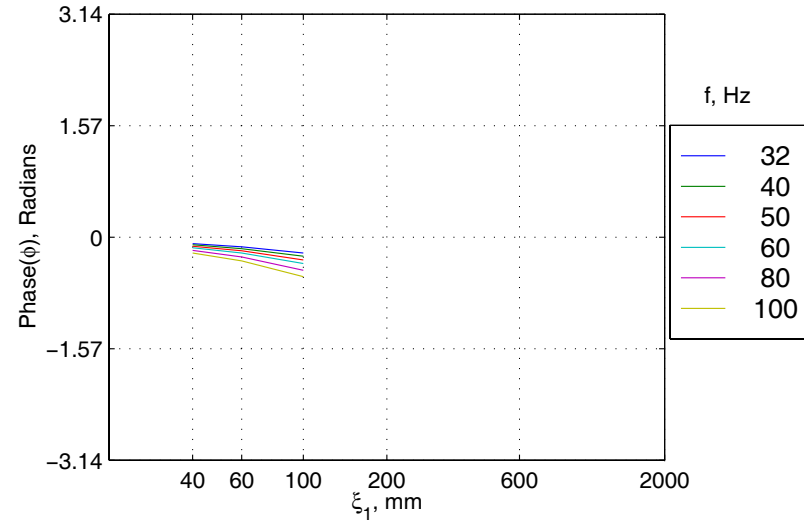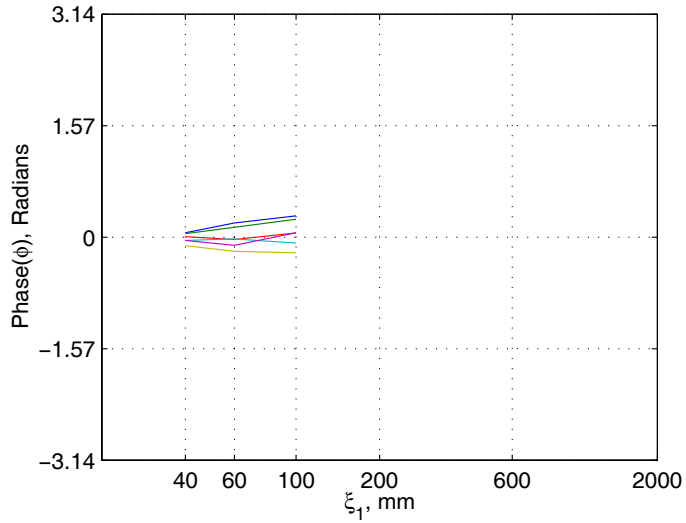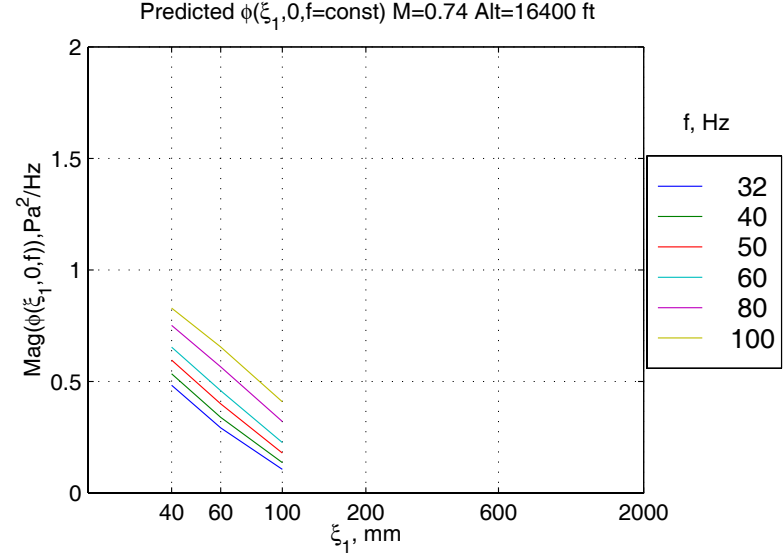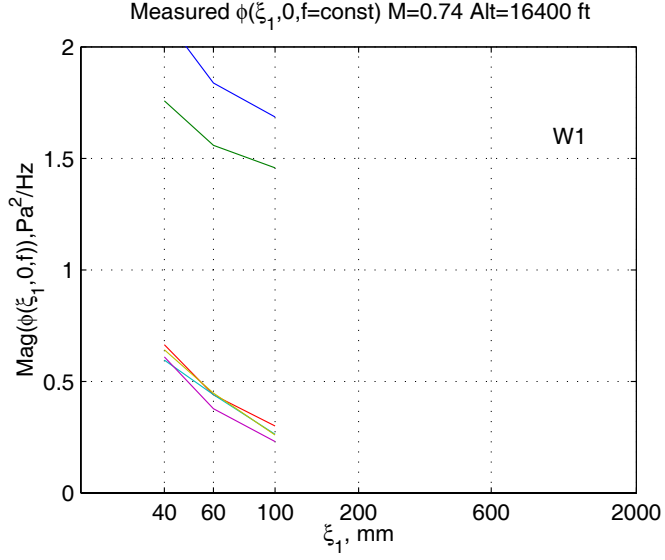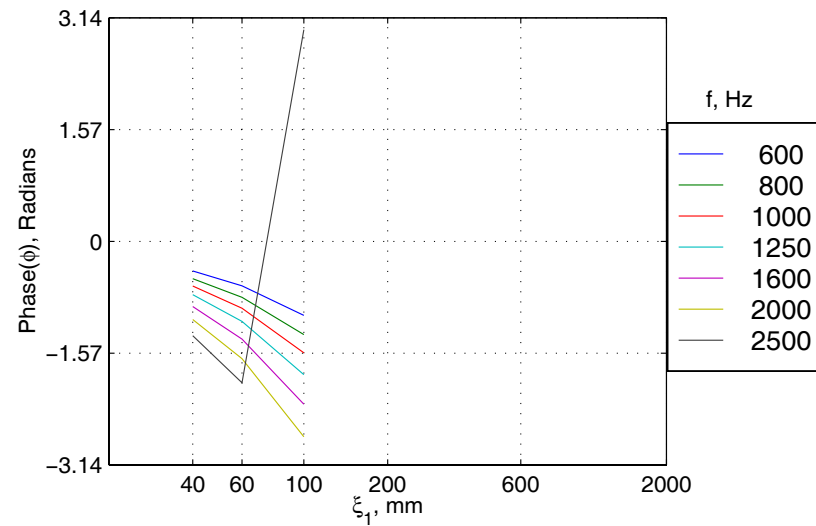
Figure 24 Cross-Spectra - Longitudinal, Window Blank 1, Measured and Predicted at Mach 0.74, 32 to 100 Hz
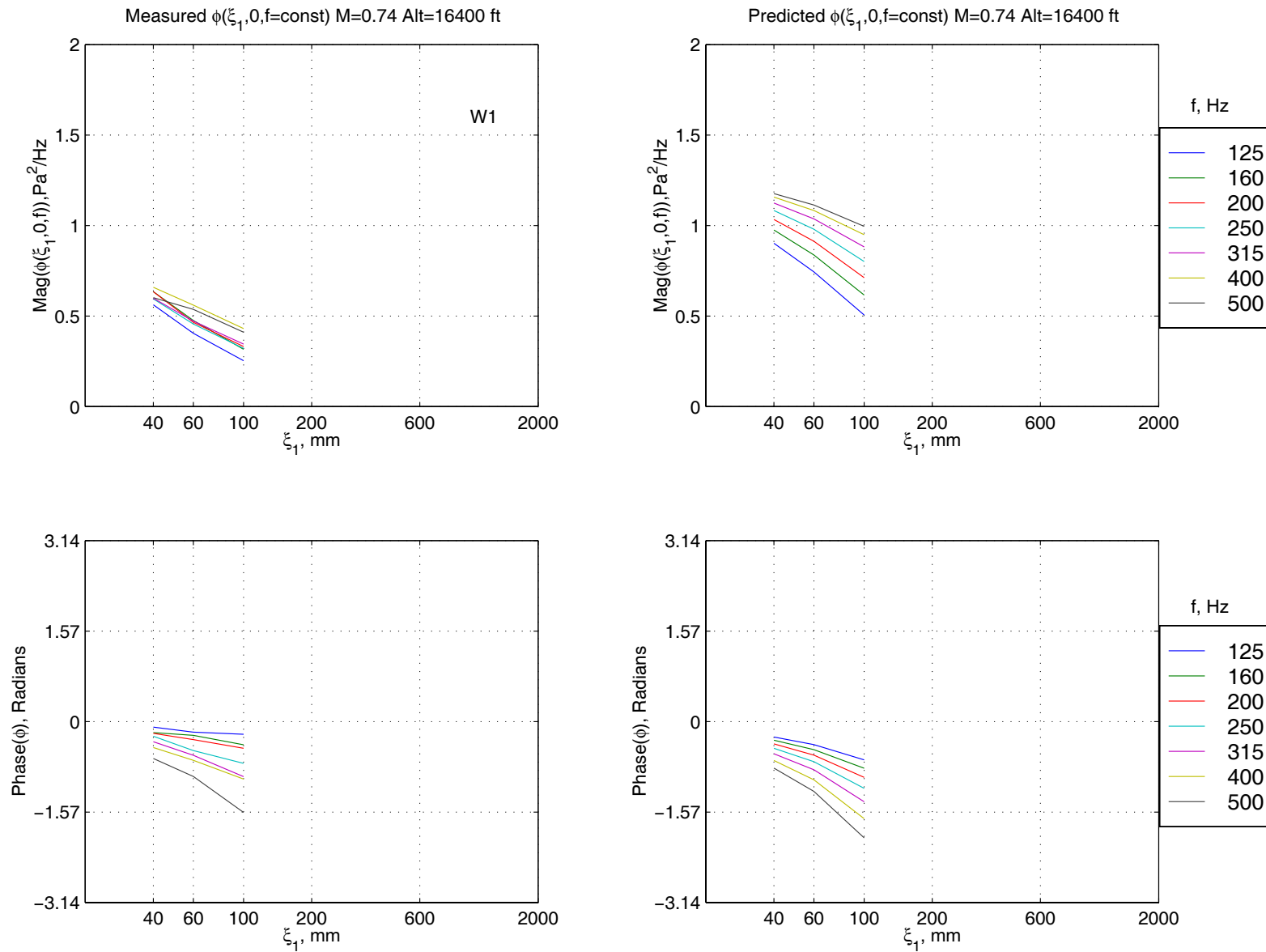
Figure 25 Cross-Spectra - Longitudinal, Window Blank 1, Measured and Predicted at Mach 0.74, 125 to 500 Hz
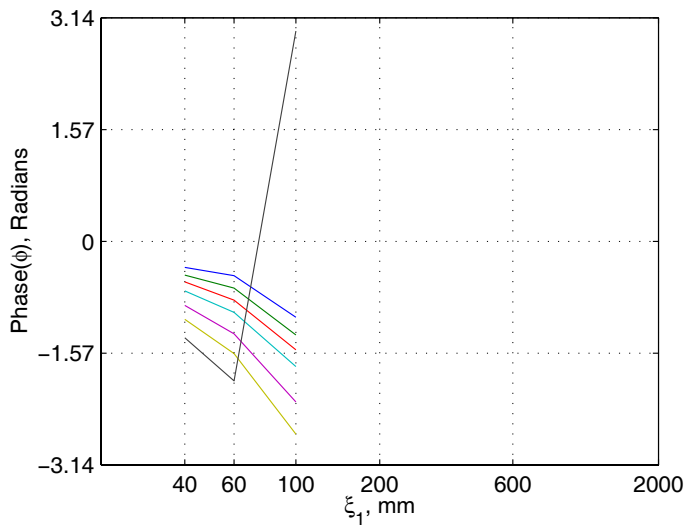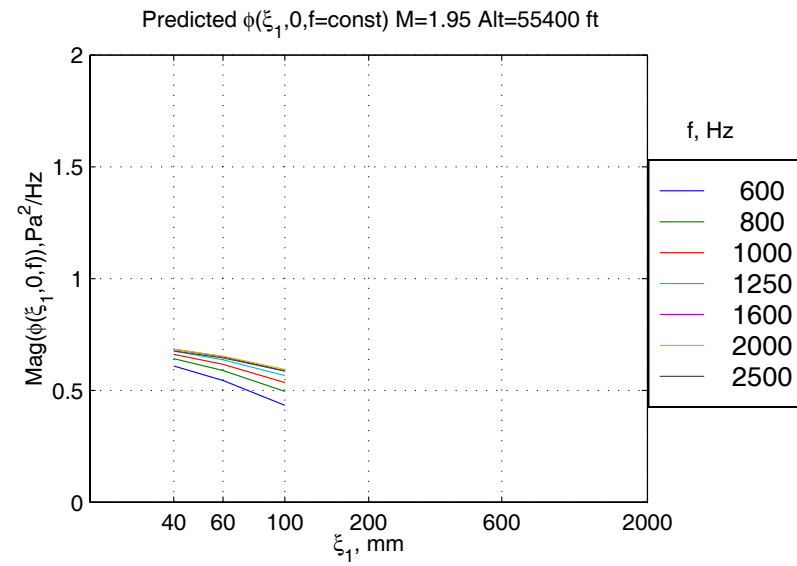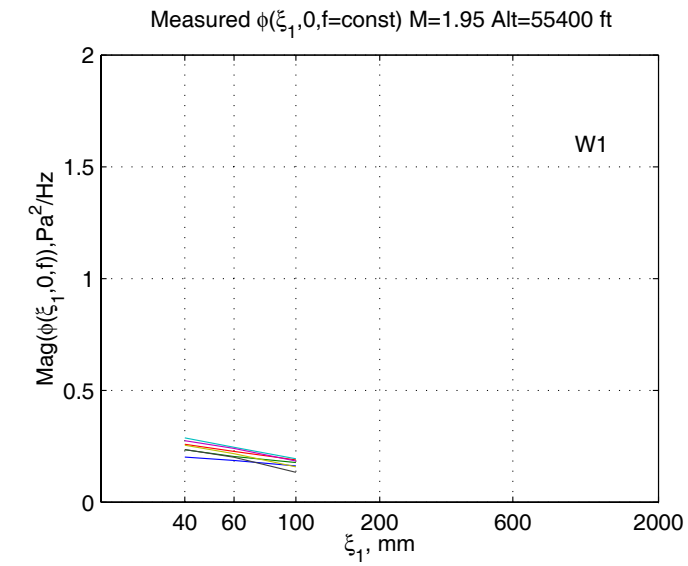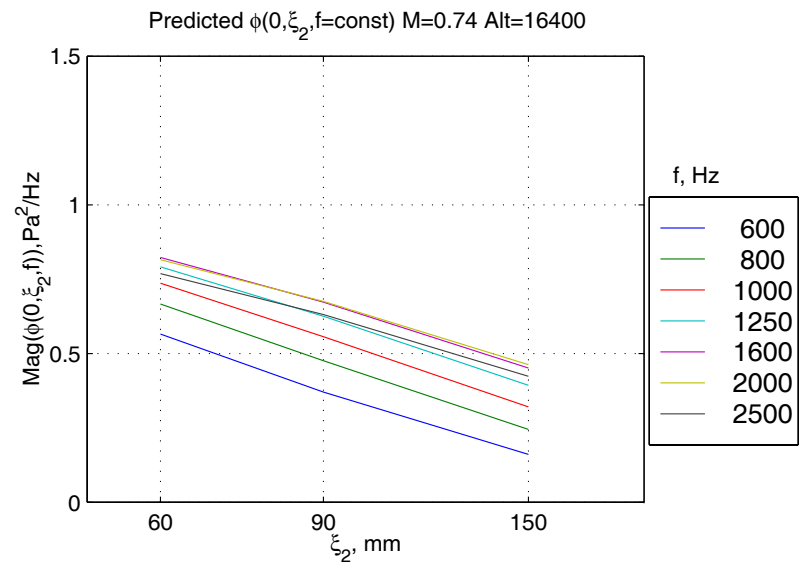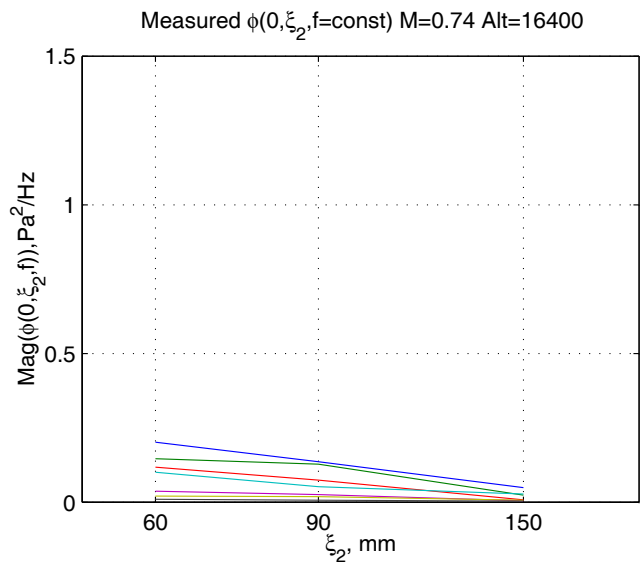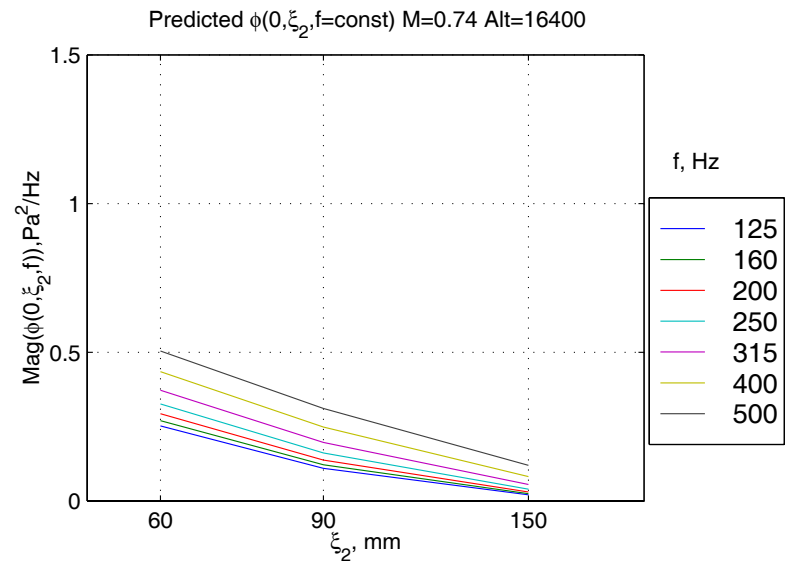
27
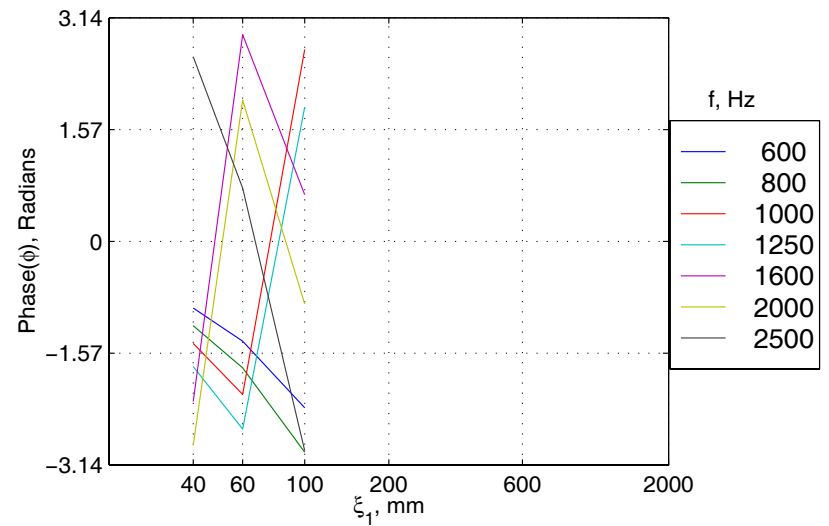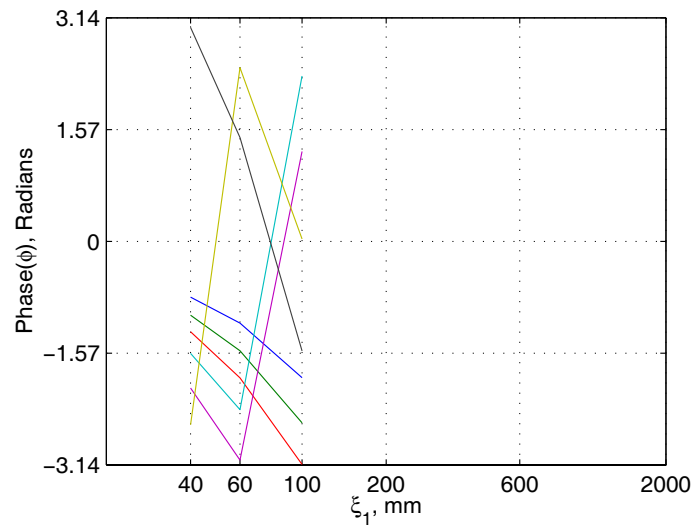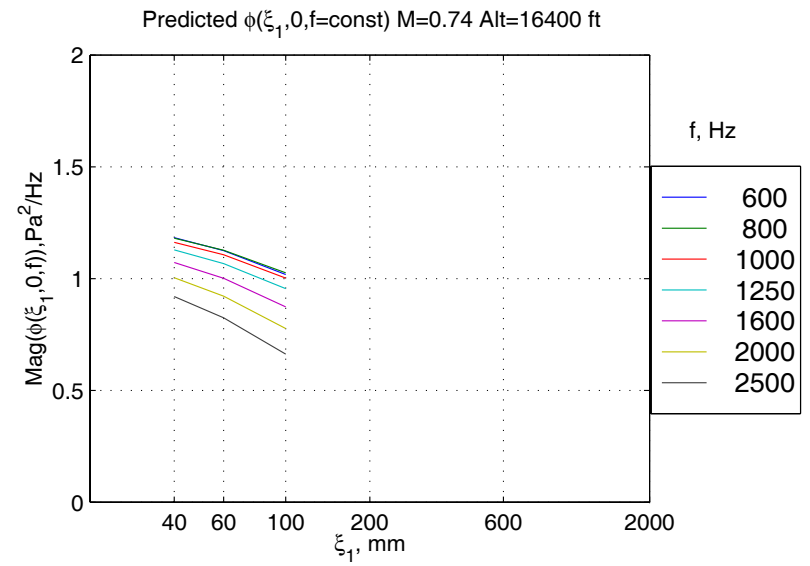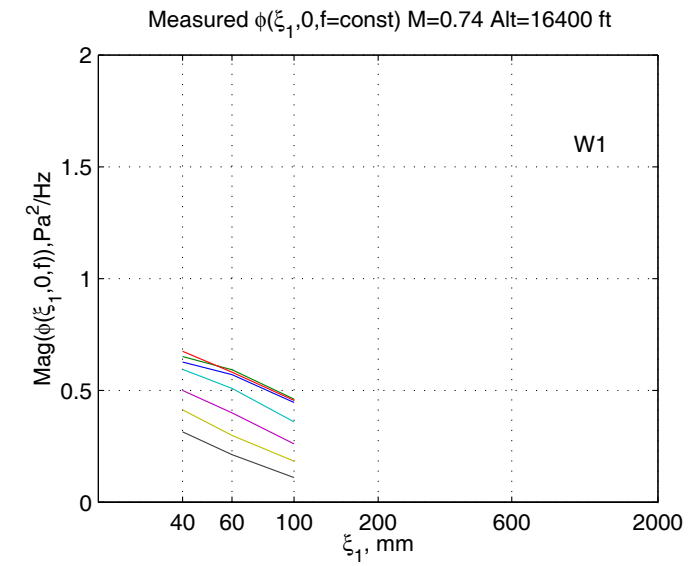
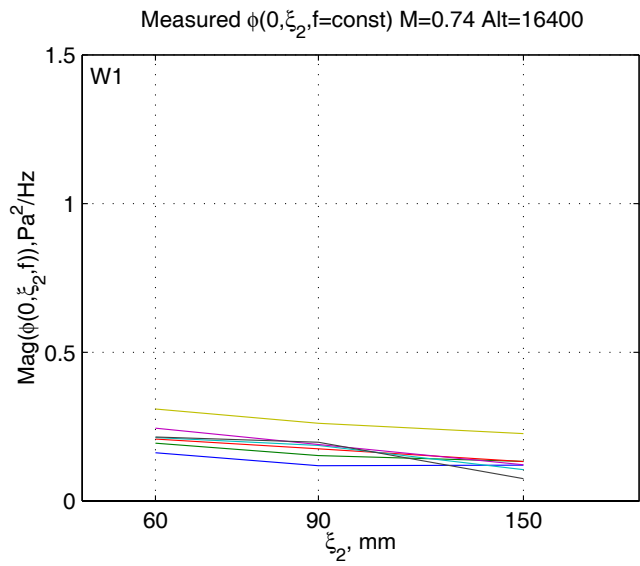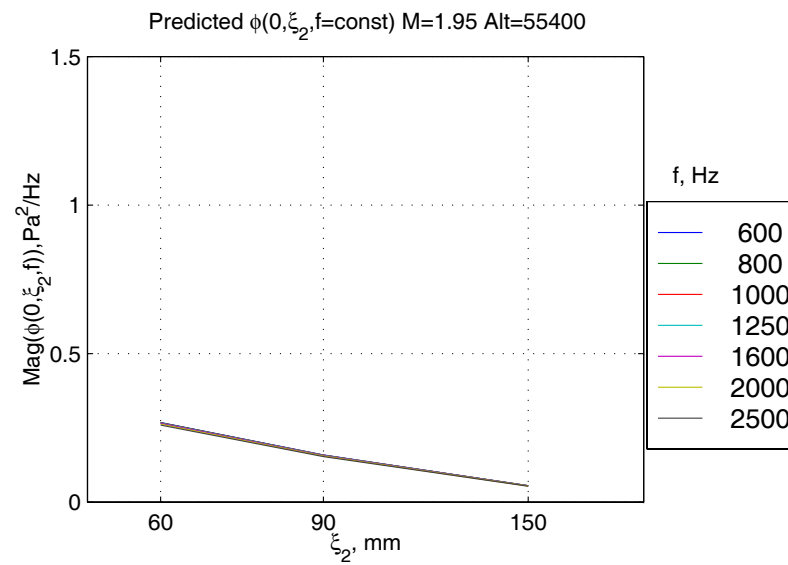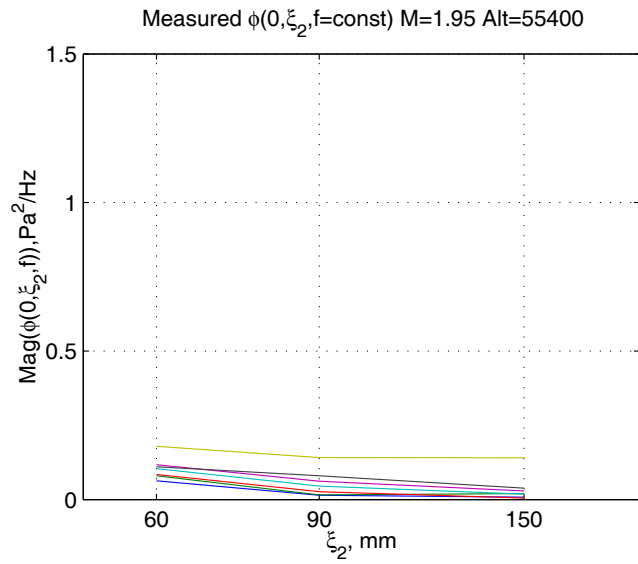**Figure 26 Cross-Spectra - Longitudinal, Window Blank 1, Measured and Predicted at Mach 0.74, 600 to 2500 Hz**
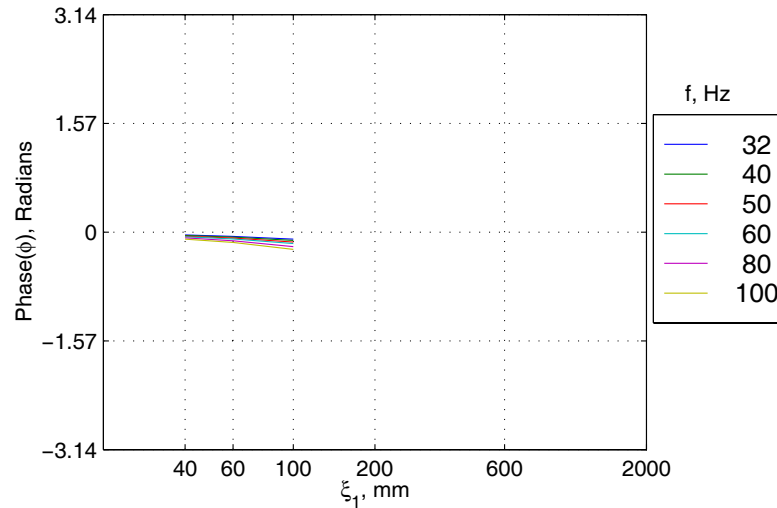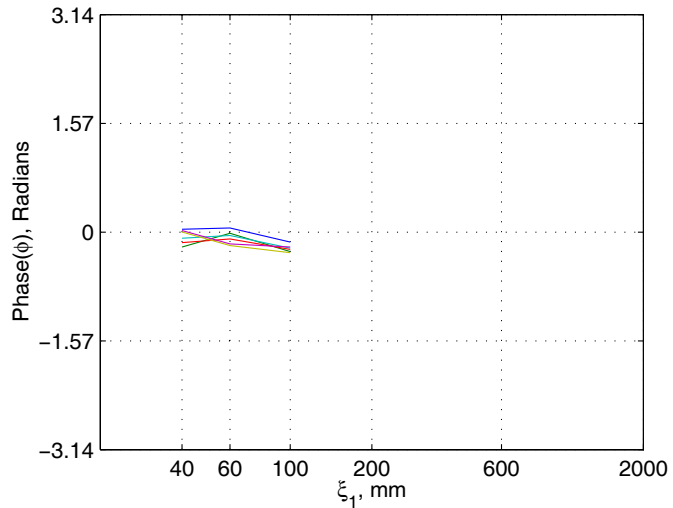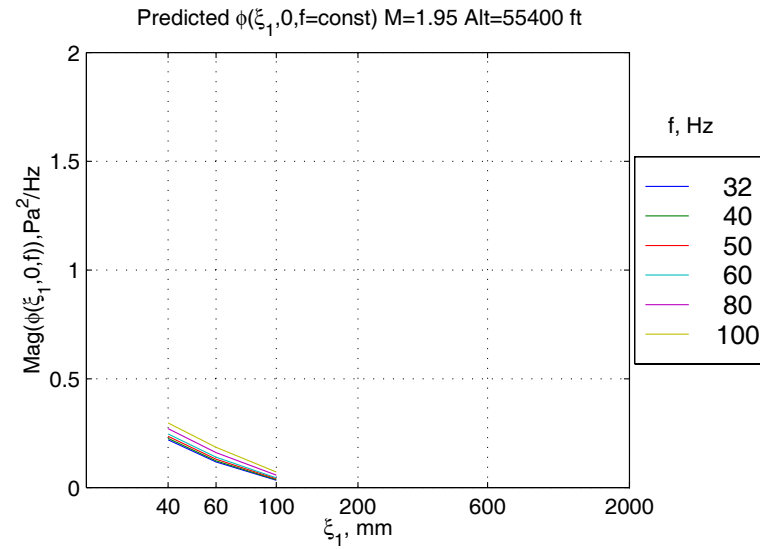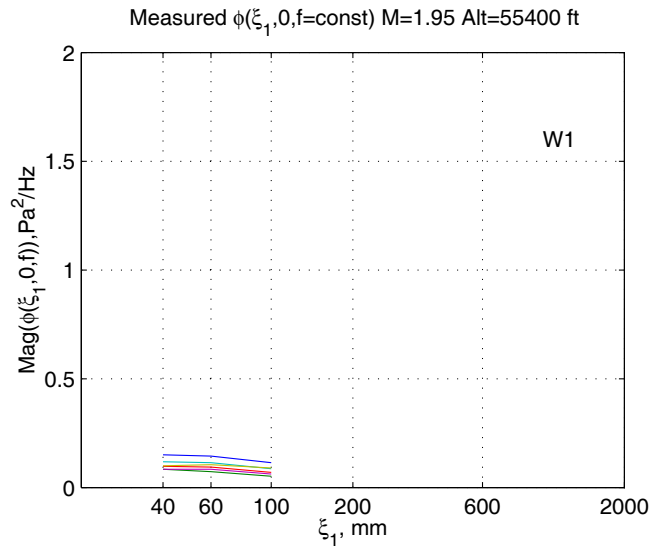
Figure 27 Cross-Spectra - Longitudinal, Window Blank 1, Measured and Predicted at Mach 1.95, 32 to 100 Hz

29
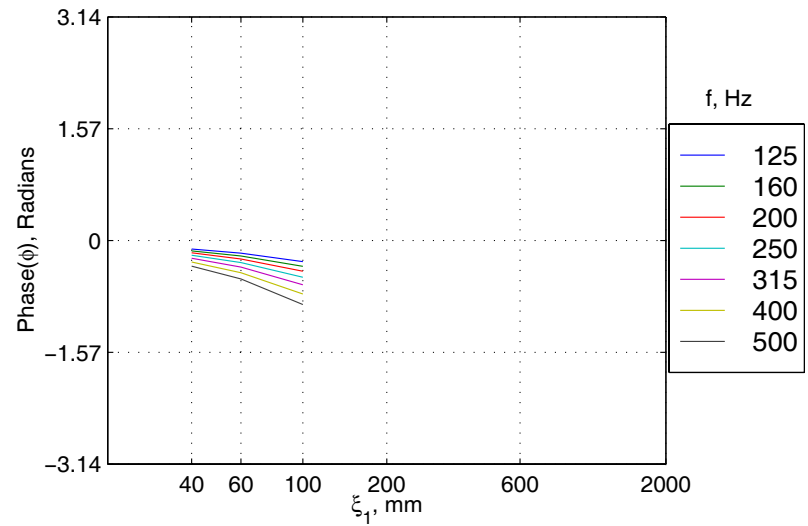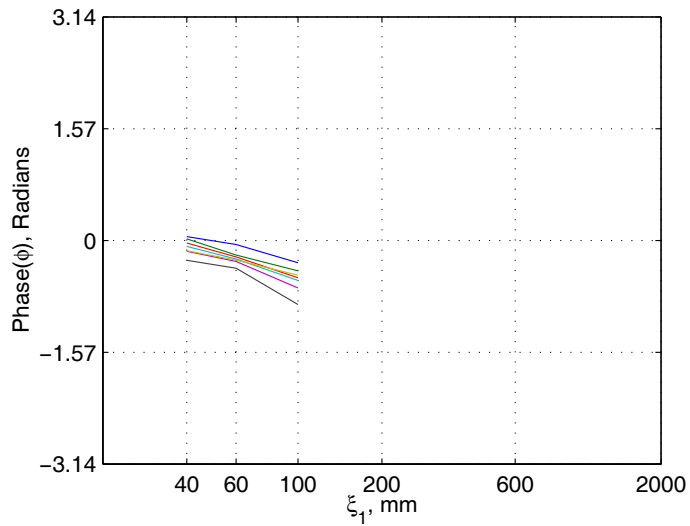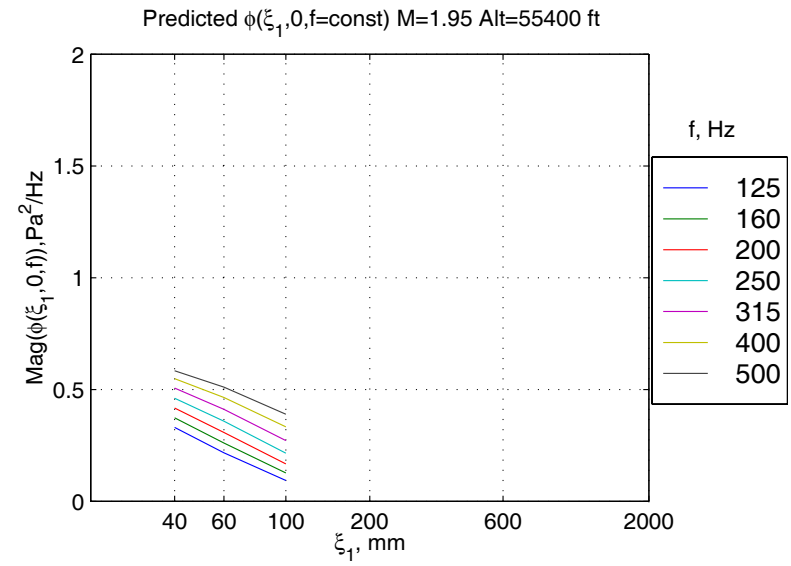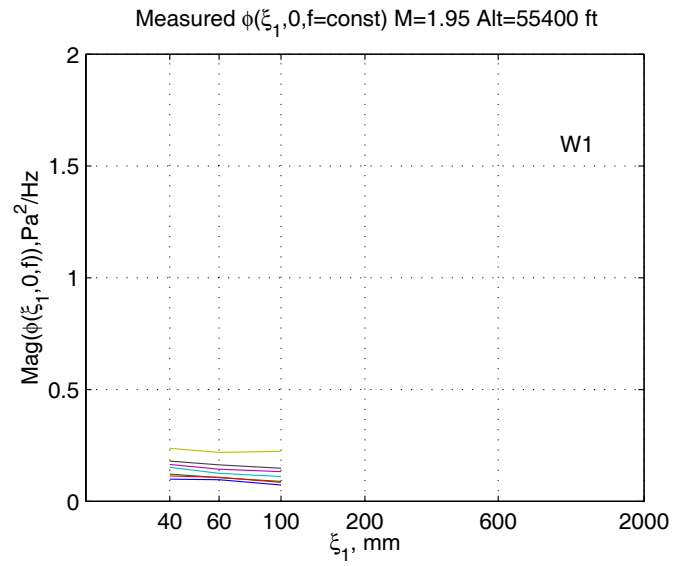
Figure 28 Cross-Spectra - Longitudinal, Window Blank 1, Measured and Predicted at Mach 1.95, 125 to 500 Hz

Figure 29 Cross-Spectra - Longitudinal, Window Blank 1, Measured and Predicted at Mach 1.95, 600 to 2500 Hz

31

Figure 30 Cross-Spectra - Lateral, Window Blank 1, Measured and Predicted at Mach 0.74
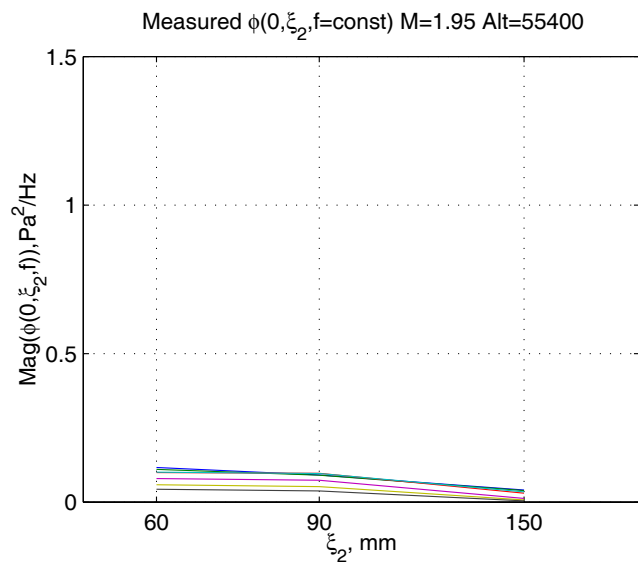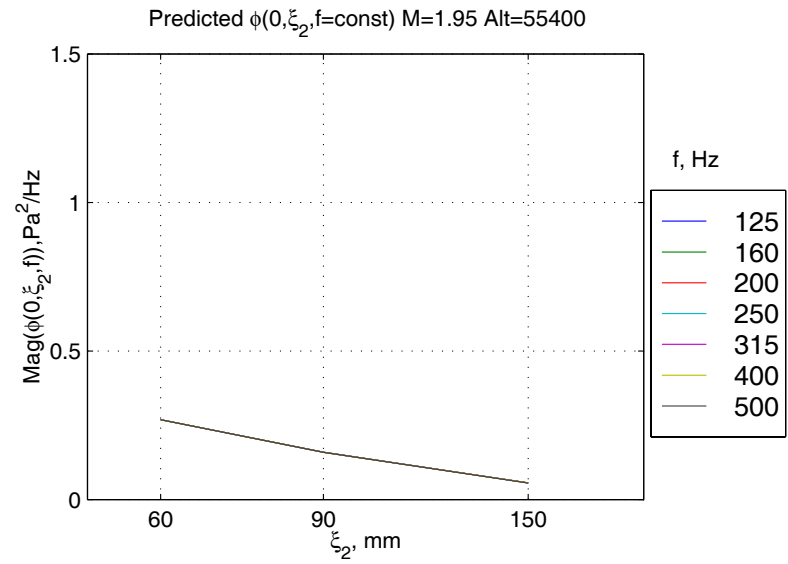
Figure 31 Cross-Spectra - Lateral, Window Blank 1, Measured and Predicted at Mach 1.95

5.2.2.2 Cross-spectra at Center Window Blank Cluster

Figure 32 through Figure 46 show cross-spectral values plotted as a function of longitudinal (stream-wise) separation distance obtained at window blanks 3 through 5, and at transducers S1 and S2 between windows. The measured narrow band cross spectral real and imaginary parts were averaged over third octave bands. Measured and predicted (using Efimtsov's model) magnitude and phase are shown for three different frequency regions on three separate graphs for each of five Mach numbers. We chose **not** to normalize the data (by dividing by the rms value for the selected frequency band) in order to provide magnitude comparisons between frequencies and between Mach numbers. Here are some observations:

- Comparisons of measured with predicted data is more favorable at Mach numbers away from Mach 1 (0.74 and 1.95) than for Mach 0.88 and 1.2.

- Predicted magnitude is usually higher than measured at smaller separations. Regarding decay rates, predicted magnitude decreases with increasing separation faster than measured.

- The Mach 1.6 case (starting at Figure 41) shows abnormally high cross-spectral values. The measured low frequency phase behaves much more like the predicted than at other Mach numbers. We have no explanation for this occurrence.

- Measured cross spectral values often peak around 500 Hz for all separation distances. This is in agreement with predictions.

- The measured phase behaves much more erratically than the predicted one in the low frequencies. In the mid frequencies, measured and predicted phases often compare well. As one would expect, phase behavior at the higher frequencies is hard to discern.

Figure 47 and Figure 48 show cross-spectral values (magnitude only) plotted as a function of lateral (cross-stream) separation distance obtained at window blank 4. Only two such separations were available: 60 and 120 mm. Some observations:

- At Mach 0.74, the magnitude is much smaller than predicted, whereas it is comparable at Mach 2.

- The slopes with separation distance are generally comparable to the prediction for Mach 0.74, but not for Mach 1.95.

- At Mach 1.95, the prediction almost independent of frequency; the measured data shows a definite frequency dependence.

- Measured and predicted data both exhibit a trend towards lower values with increasing Mach number.

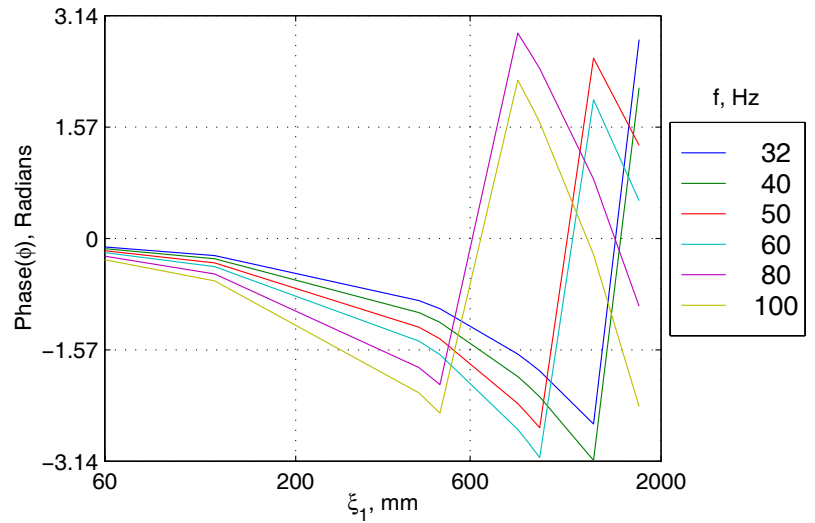No attempt was made to improve upon the cross functional model.
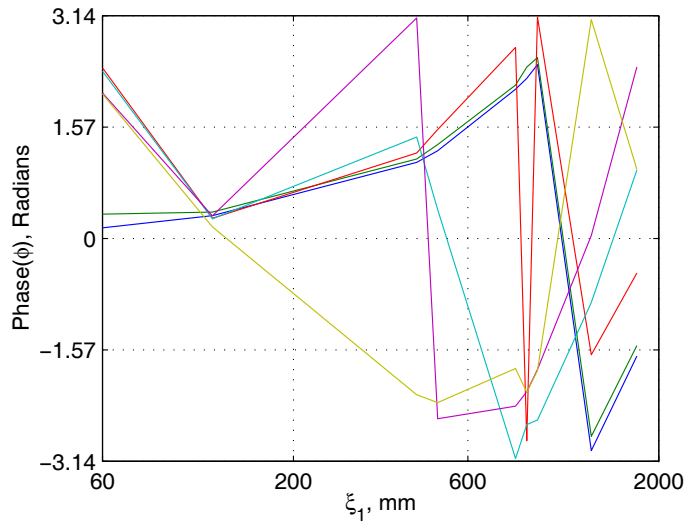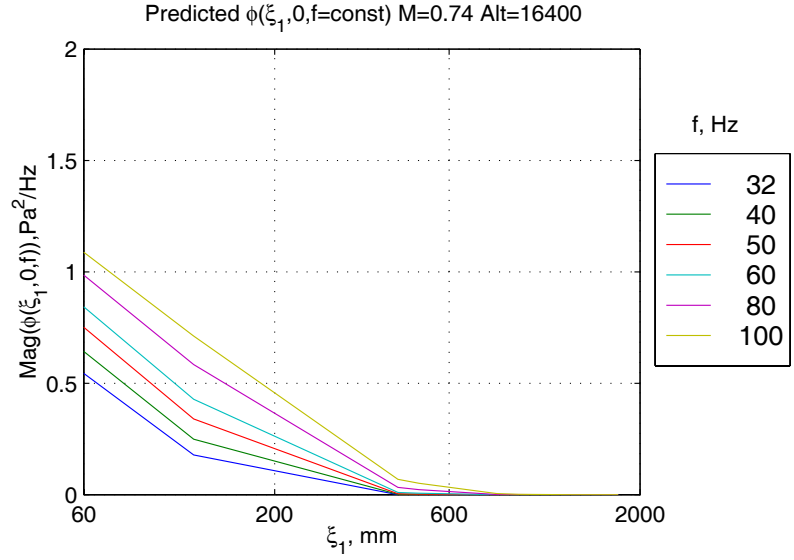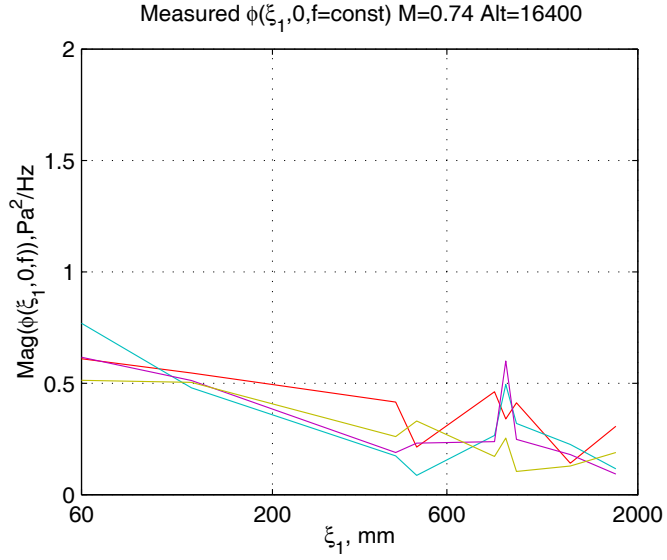
Figure 32 Cross-Spectra - Longitudinal, Central Window Blanks, Measured and Predicted at Mach 0.74, 32 to 100 Hz
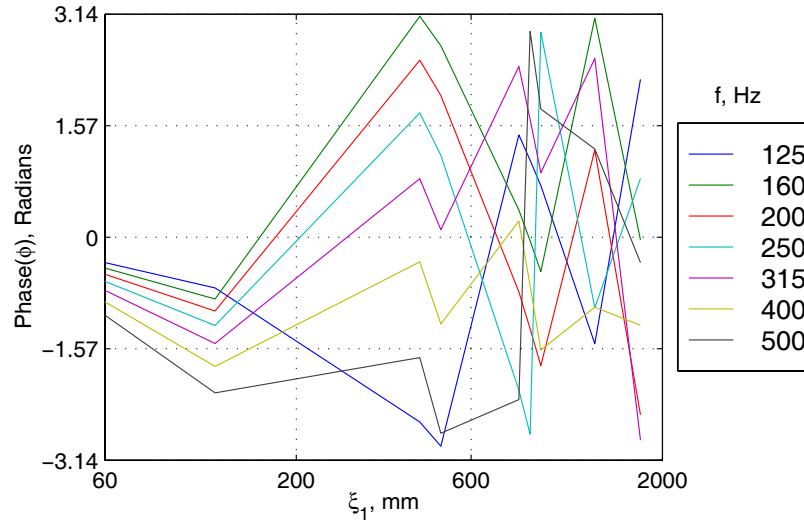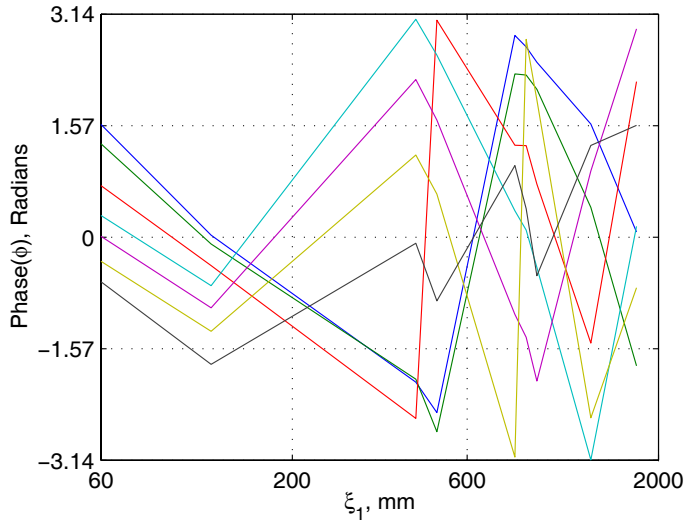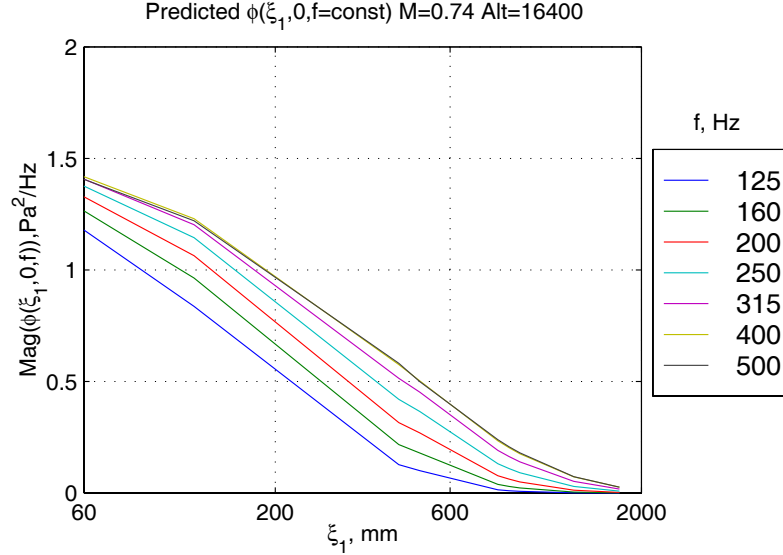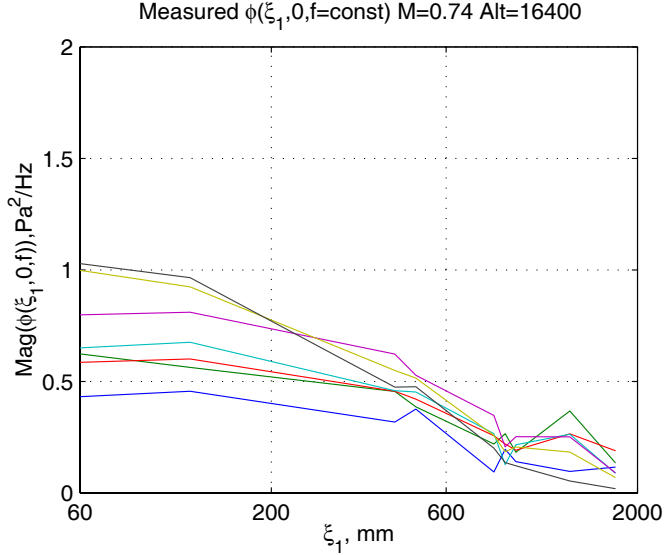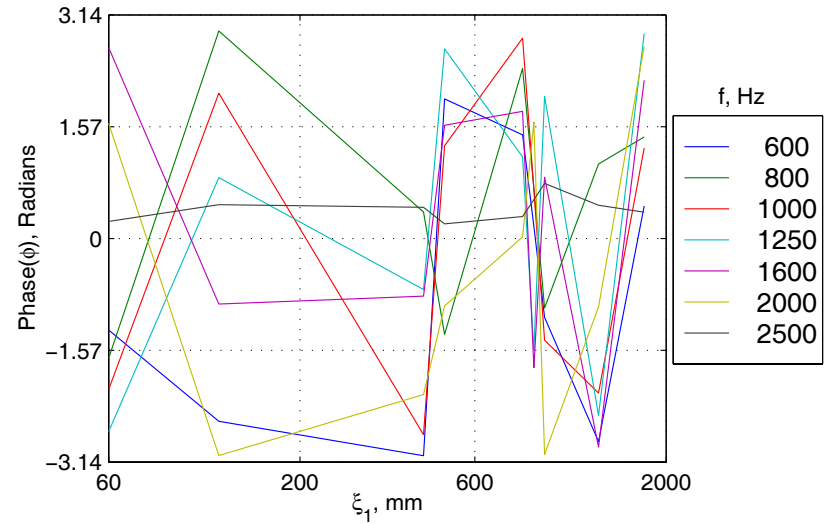
Figure 33 Cross-Spectra - Longitudinal, Central Window Blanks, Measured and Predicted at Mach 0.74, 125 to 500 Hz
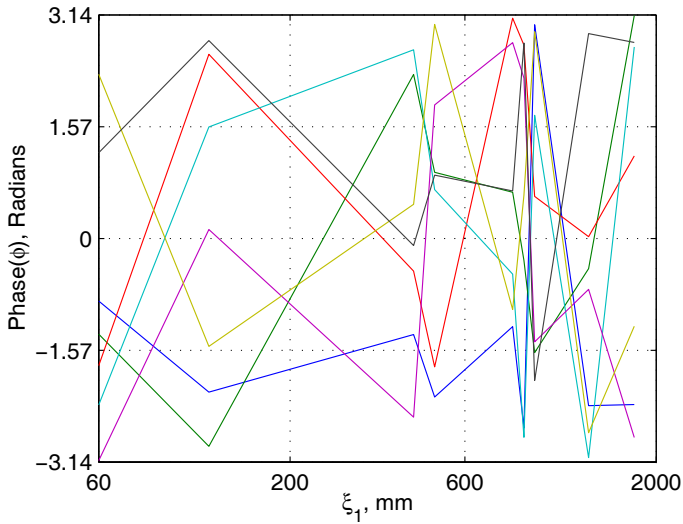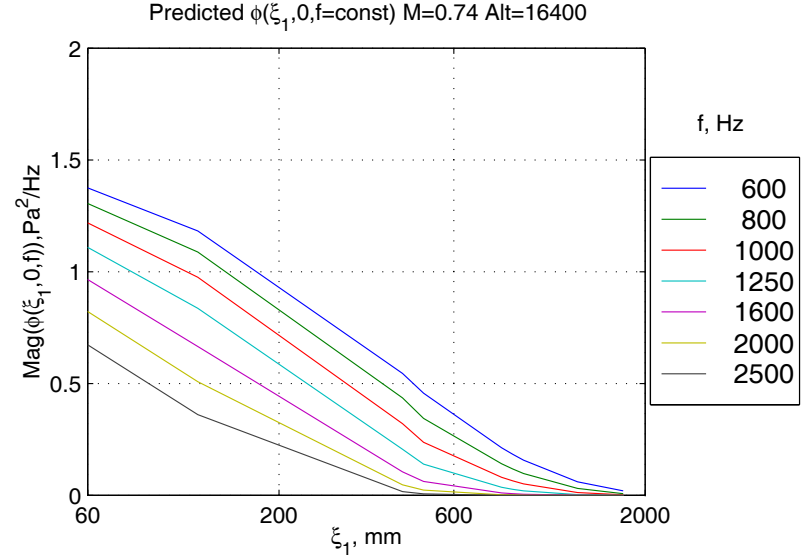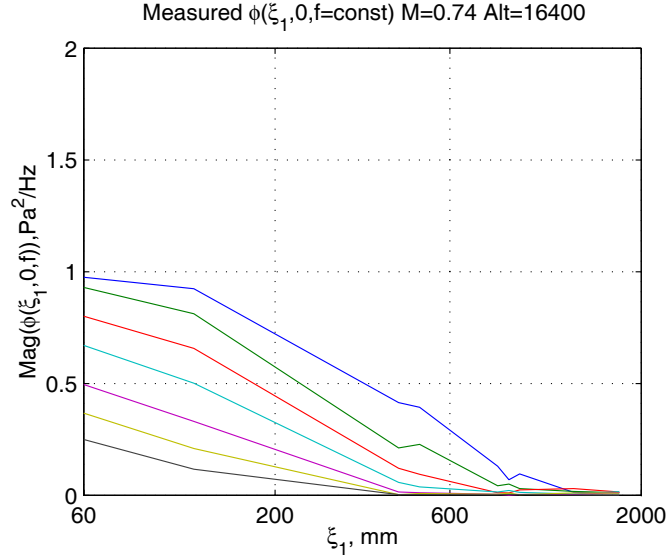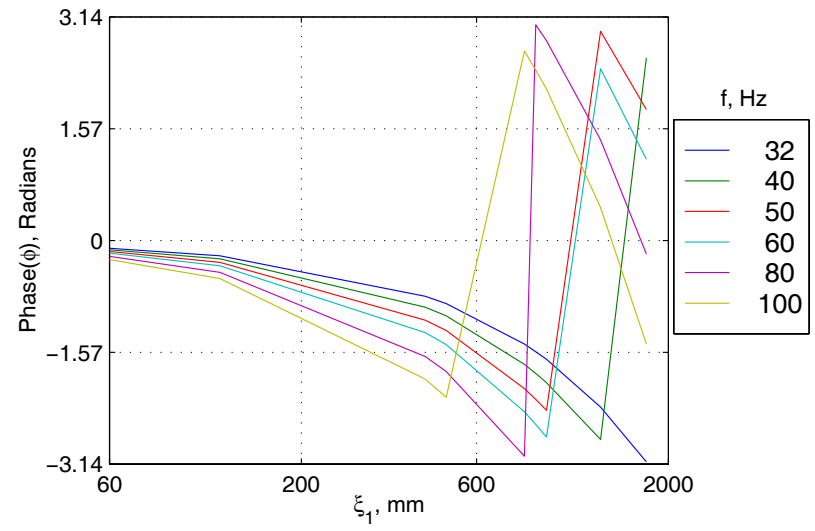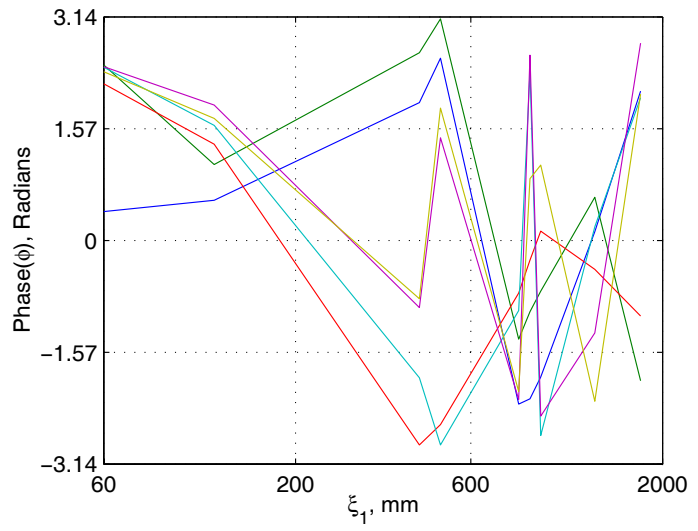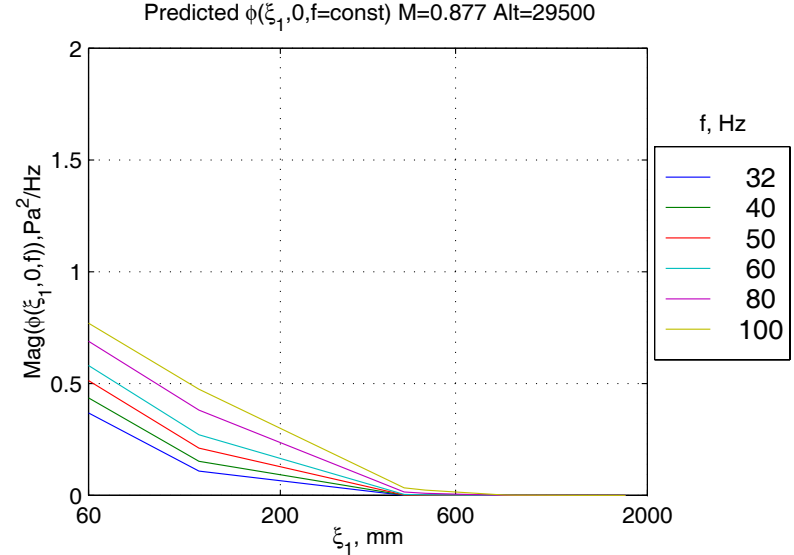
Figure 34 Cross-Spectra - Longitudinal, Central Window Blanks, Measured and Predicted at Mach 0.74, 600 to 2500 Hz
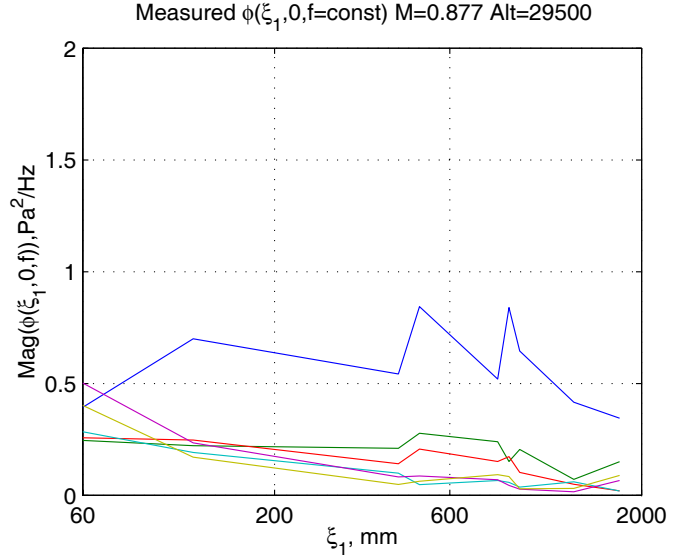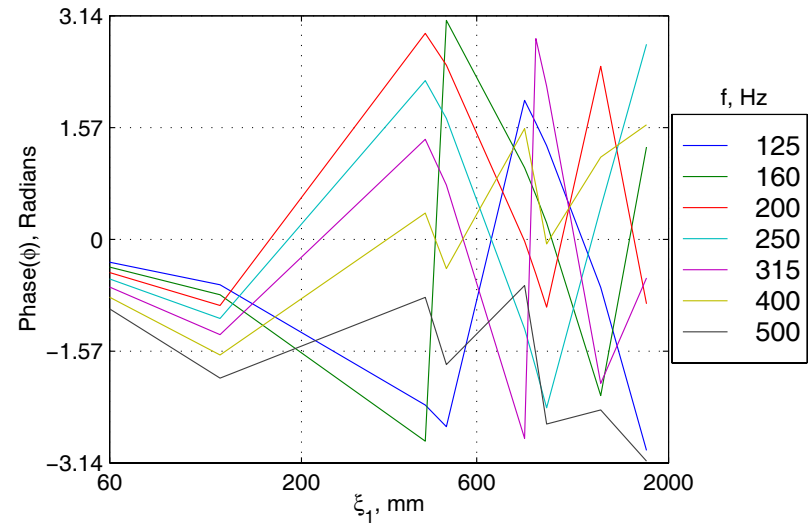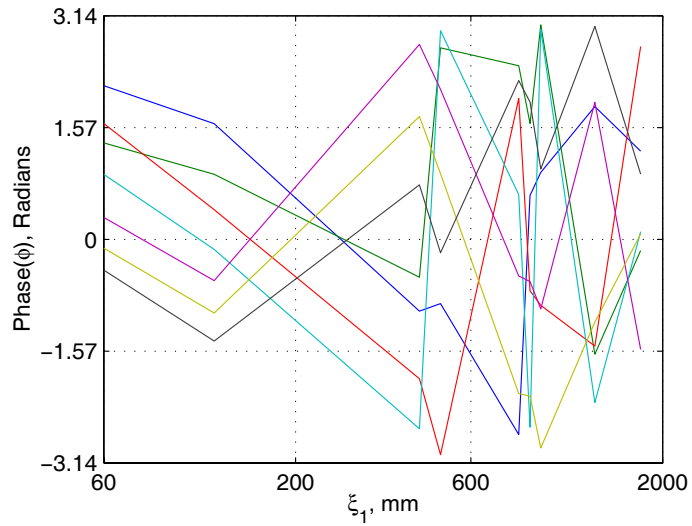
Figure 35 Cross-Spectra - Longitudinal, Central Window Blanks, Measured and Predicted at Mach 0.88, 32 to 100 Hz
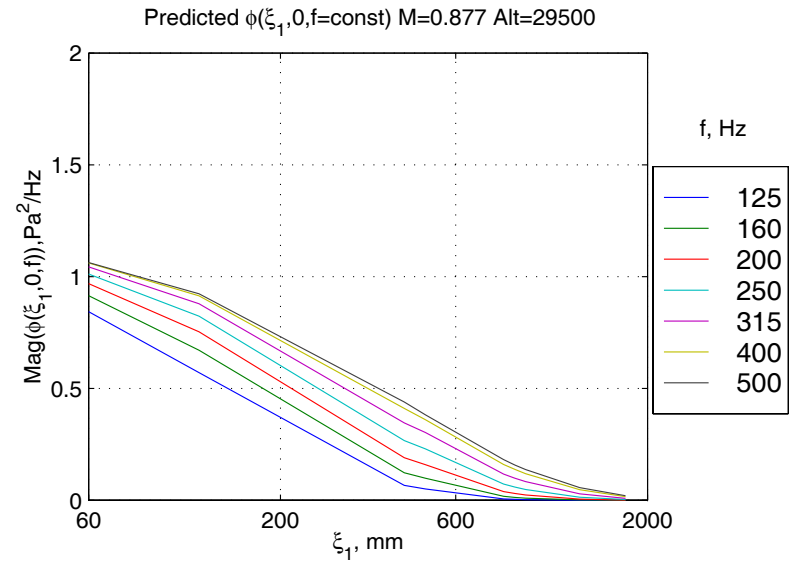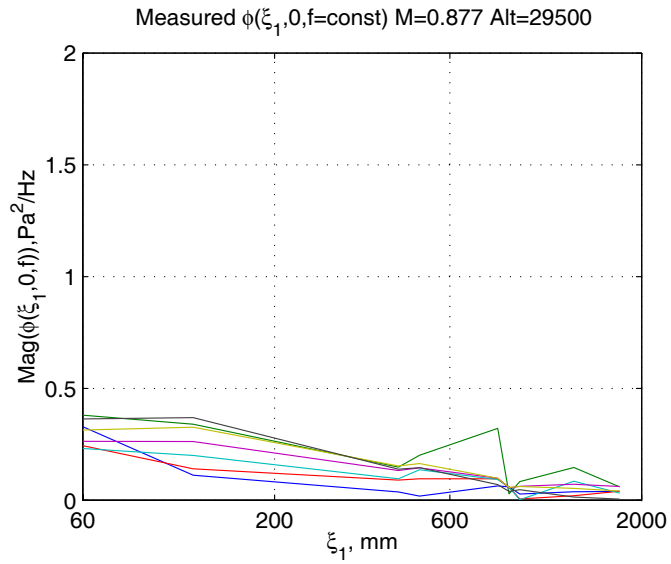
Figure 36 Cross-Spectra - Longitudinal, Central Window Blanks, Measured and Predicted at Mach 0.88, 125 to 500 Hz
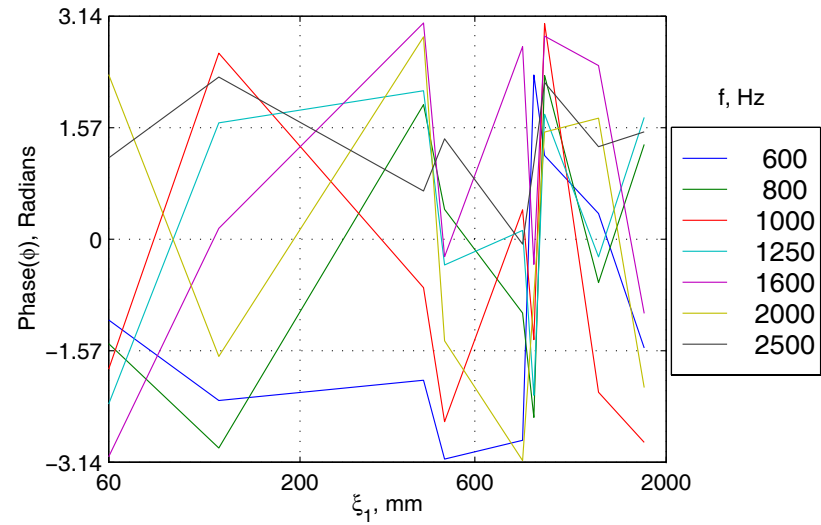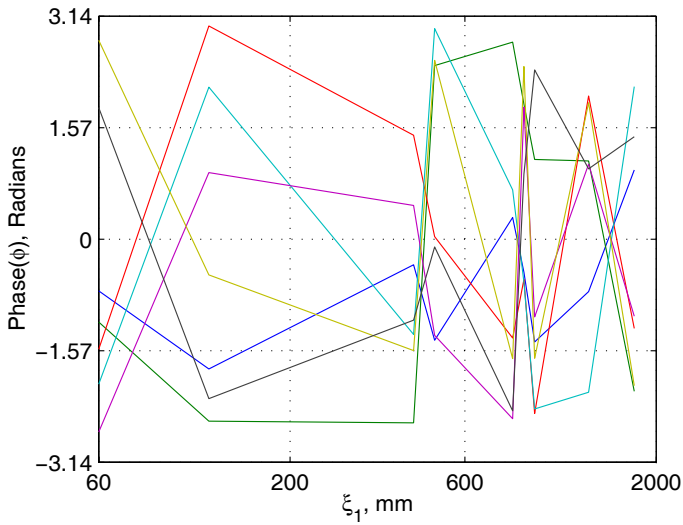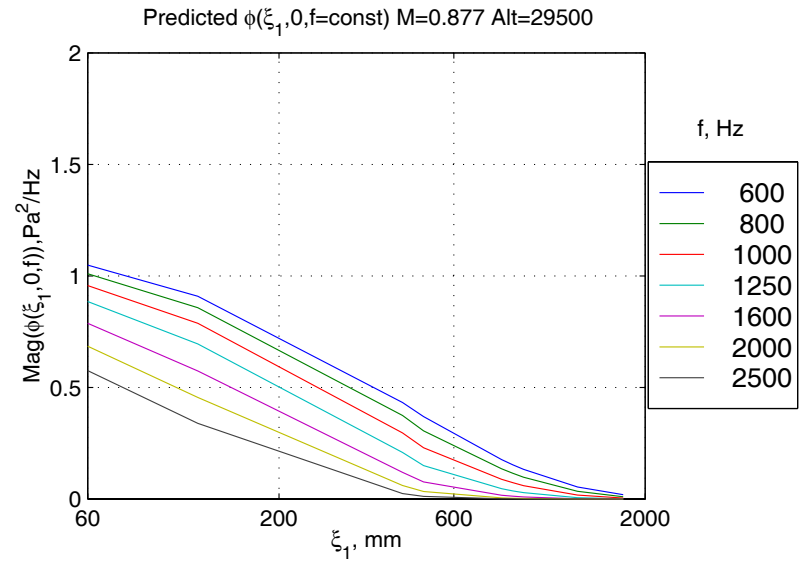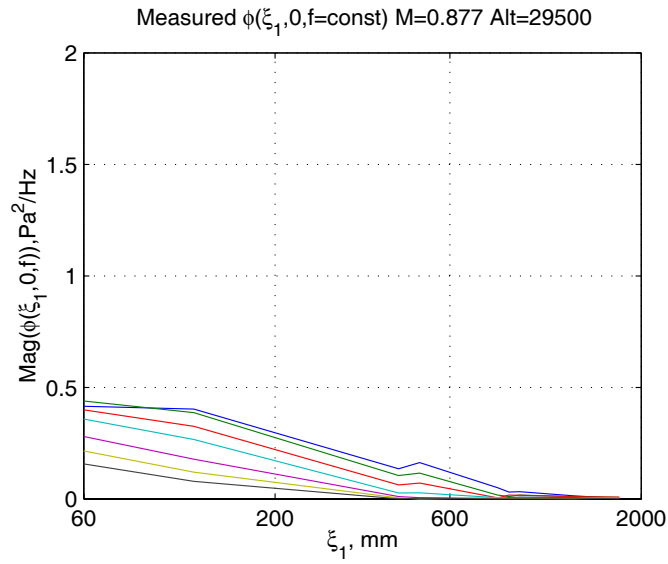
Figure 37 Cross-Spectra - Longitudinal, Central Window Blanks, Measured and Predicted at Mach 0.88, 600 to 2500 Hz

Figure 38 Cross-Spectra - Longitudinal, Central Window Blanks, Measured and Predicted at Mach 1.2, 32 to 100 Hz

Figure 39 Cross-Spectra - Longitudinal, Central Window Blanks, Measured and Predicted at Mach 1.2, 125 to 500 Hz
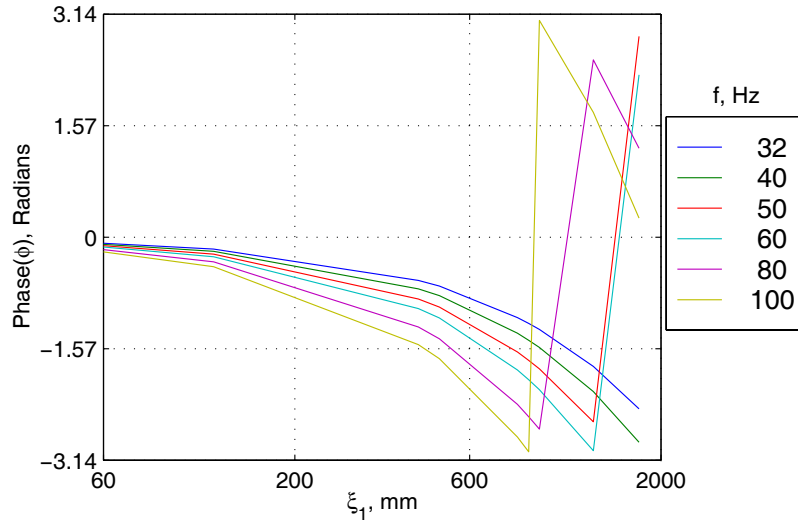
Figure 40 Cross-Spectra - Longitudinal, Central Window Blanks, Measured and Predicted at Mach 1.2, 600 to 2500 Hz
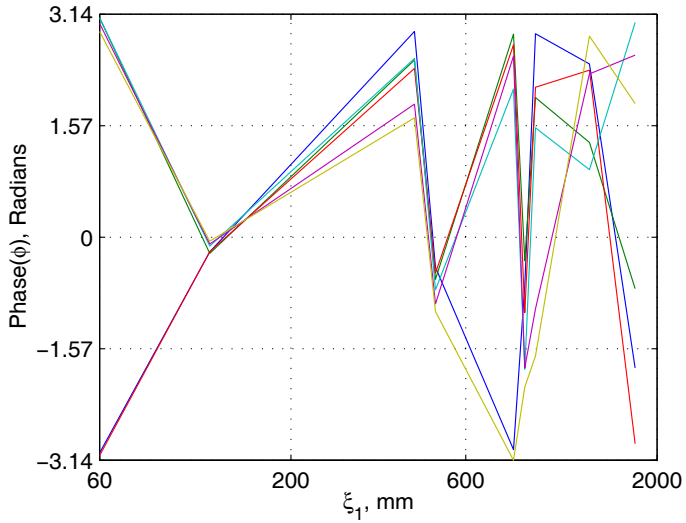
Figure 41 Cross-Spectra - Longitudinal, Central Window Blanks, Measured and Predicted at Mach 1.6, 32 to 100 Hz

Figure 42 Cross-Spectra - Longitudinal, Central Window Blanks, Measured and Predicted at Mach 1.6, 125 to 500 Hz

Figure 43 Cross-Spectra - Longitudinal, Central Window Blanks, Measured and Predicted at Mach 1.6, 600 to 2500 Hz
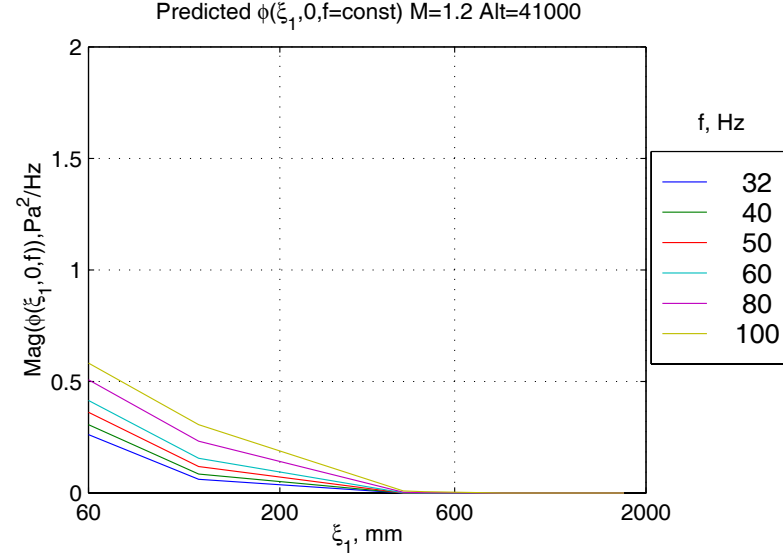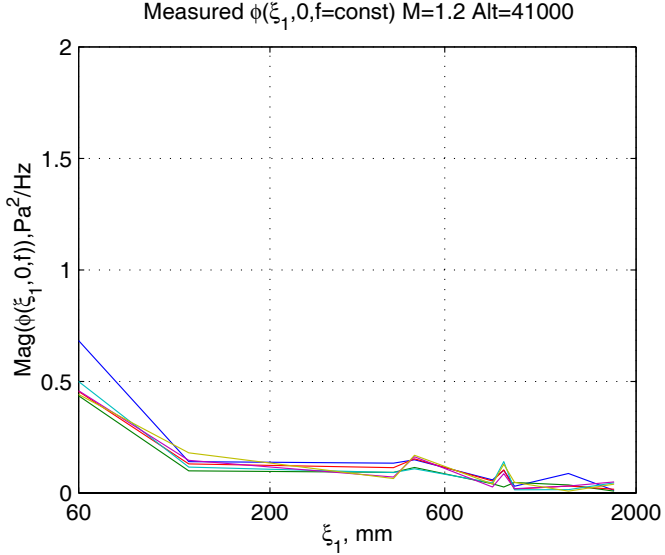
Figure 44 Cross-Spectra - Longitudinal, Central Window Blanks, Measured and Predicted at Mach 1.95, 32 to 100 Hz
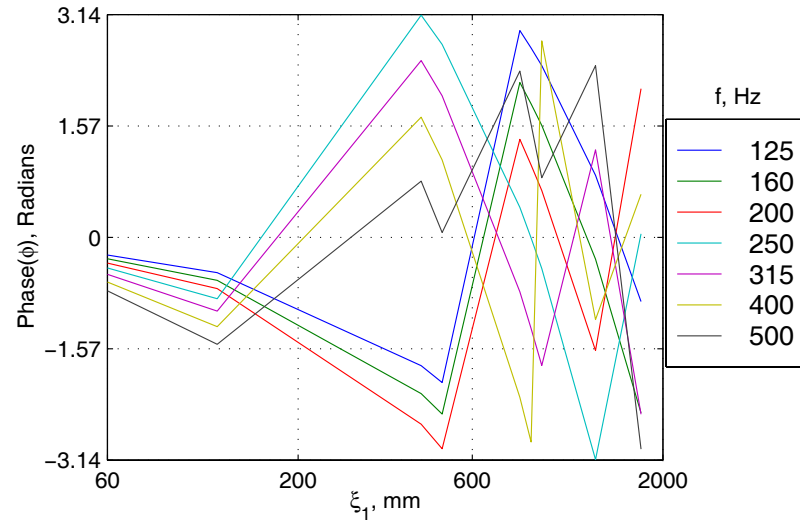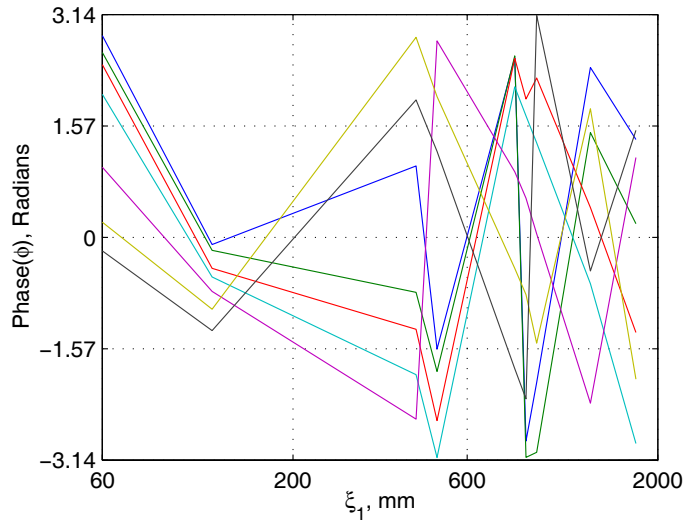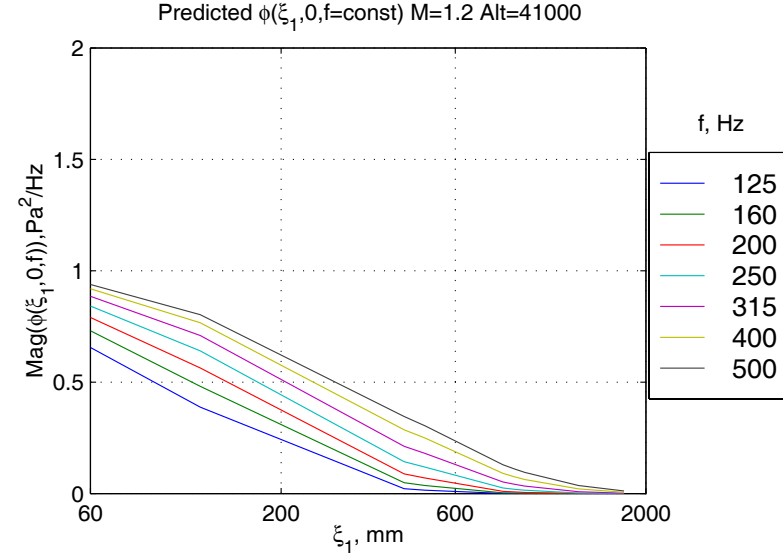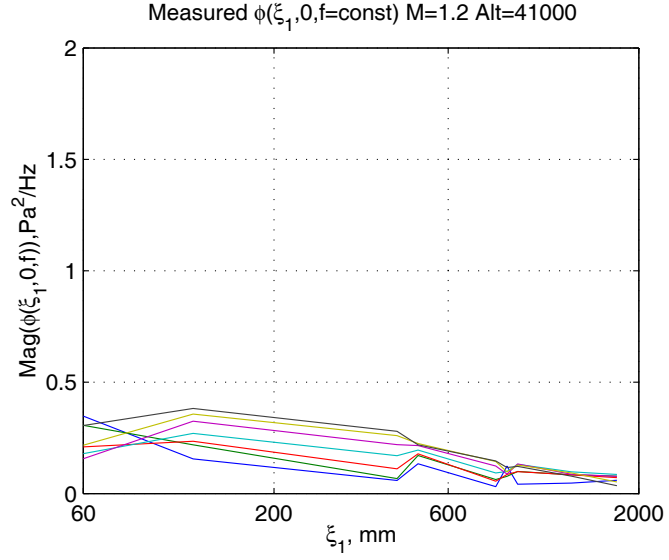
Figure 45 Cross-Spectra - Longitudinal, Central Window Blanks, Measured and Predicted at Mach 1.95, 125 to 500 Hz
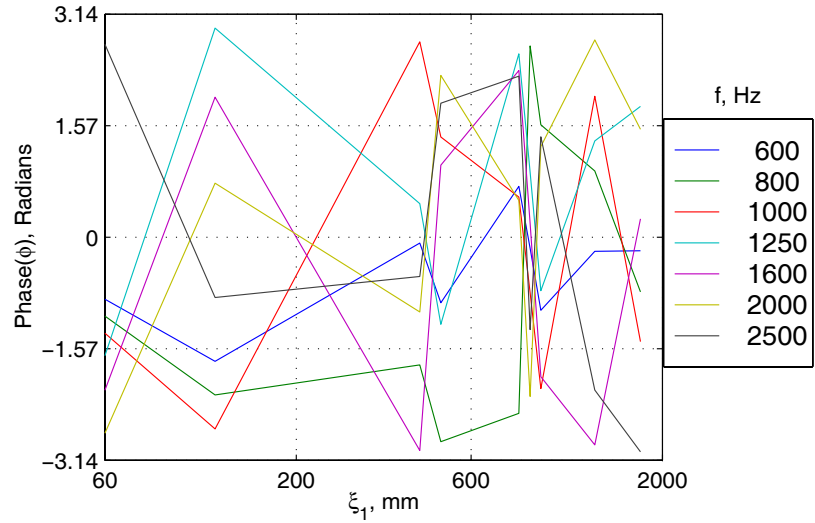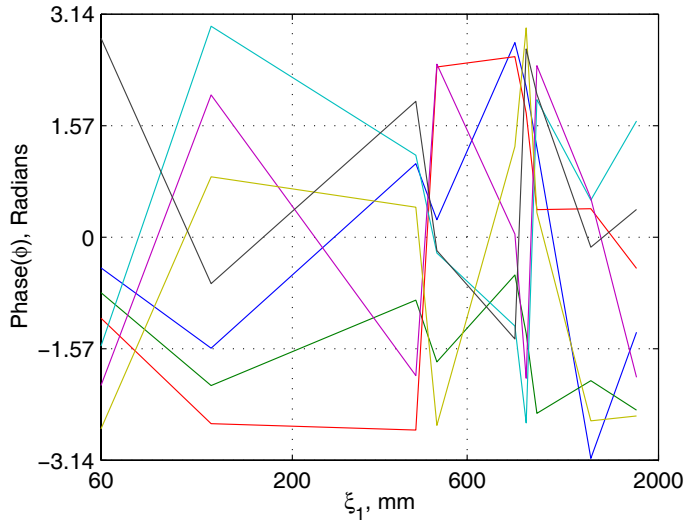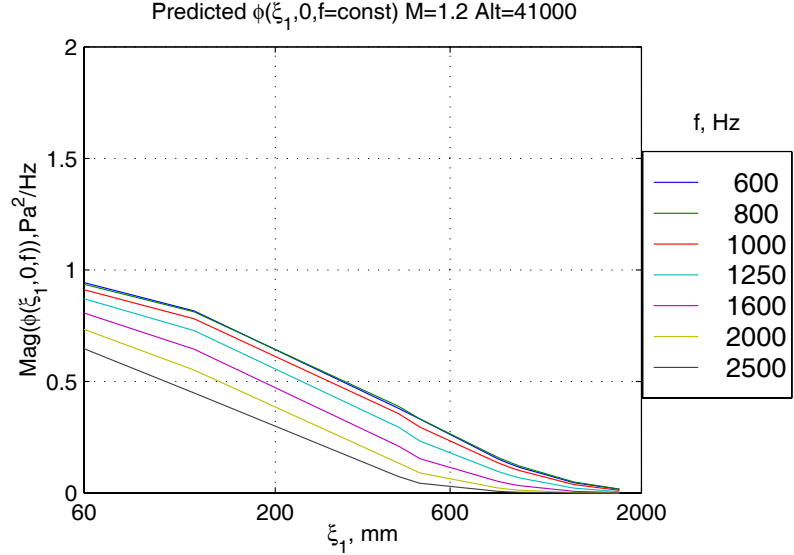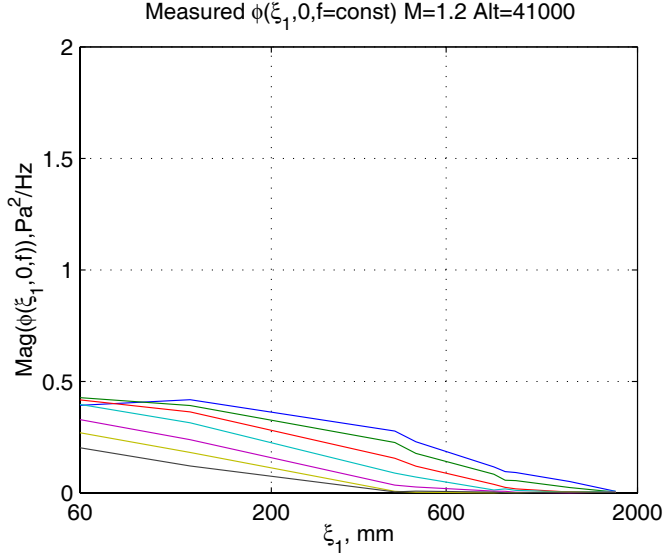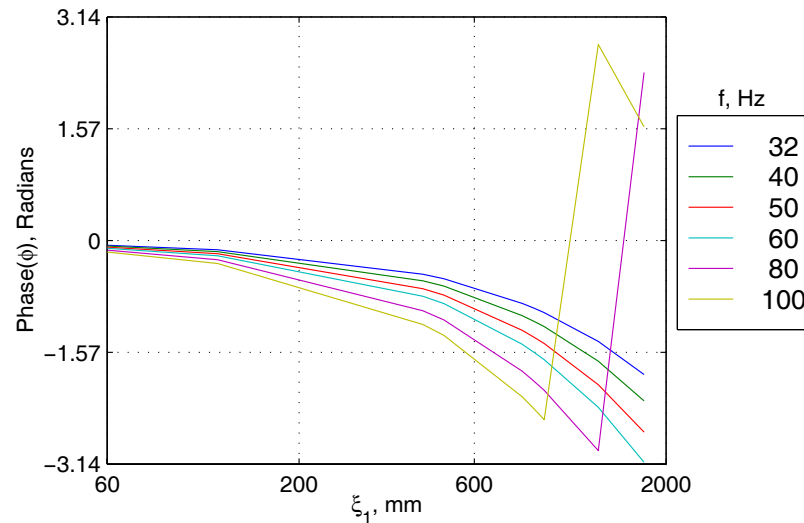
Figure 46 Cross-Spectra - Longitudinal, Central Window Blanks, Measured and Predicted at Mach 1.95, 600 to 2500 Hz
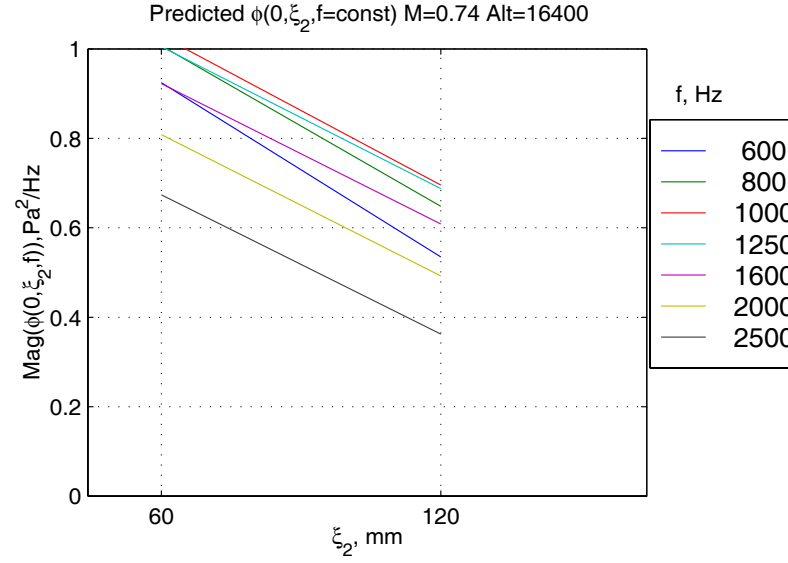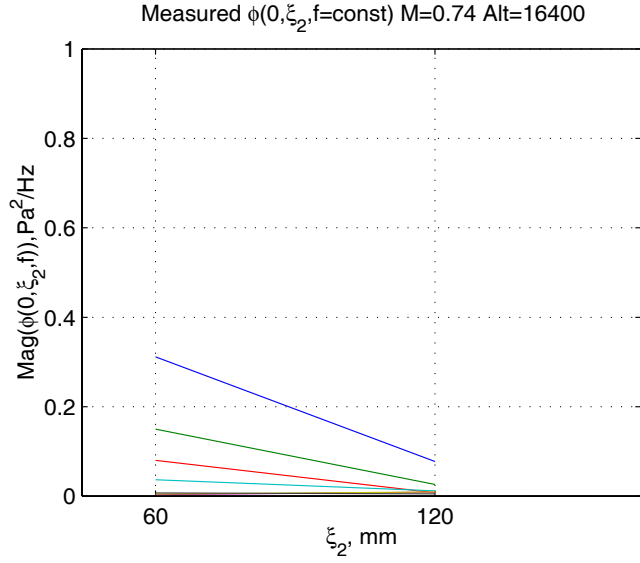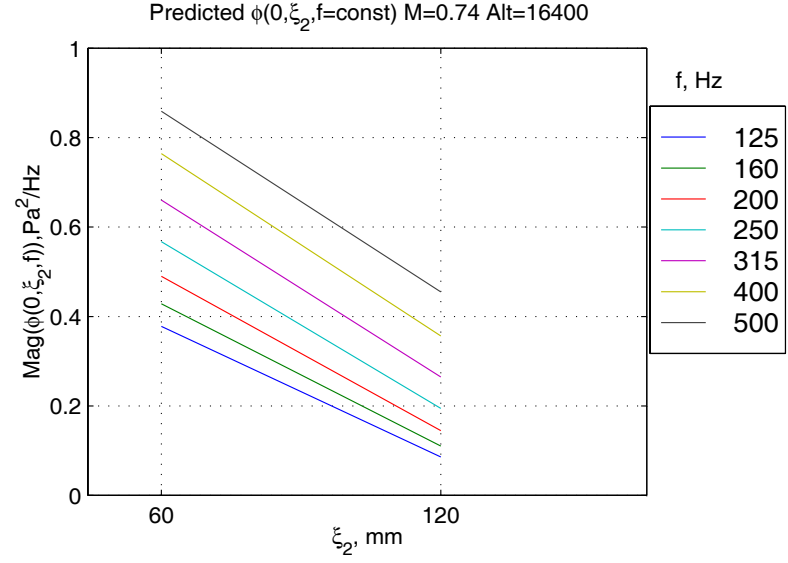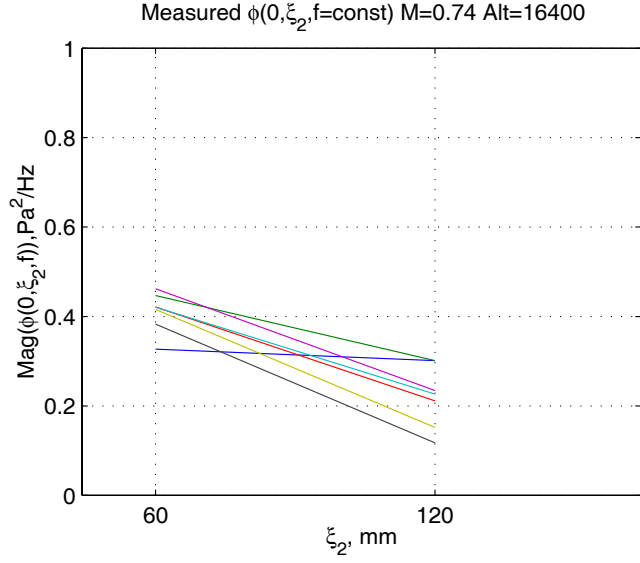
Figure 47 Cross-Spectra - Lateral, Central Window Blanks, Measured and Predicted at Mach 0.74

50
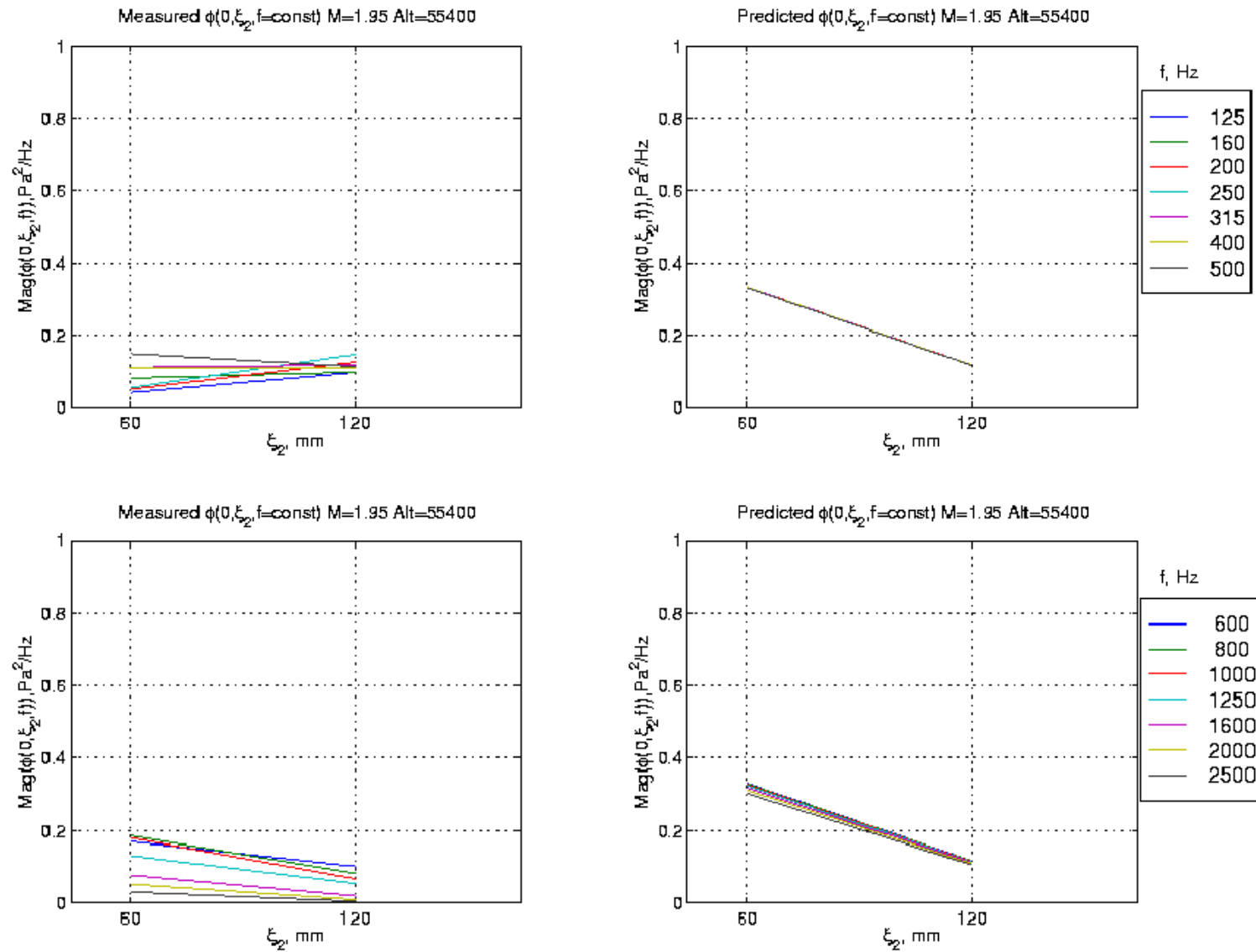
Figure 48 Cross-Spectra - Lateral, Central Window Blanks, Measured and Predicted at Mach 1.95

5.2.2.3 Cross-Spectra at Aft Window Blank

Figure 49 through Figure 54 contain cross-spectral values for longitudinal separations. At Mach 0.74, measured and predicted values (magnitude and phase) are comparable; measured decay rates are shallower. At Mach 1.95, the measured low frequency magnitudes for the smallest separation (40mm) are exceptionally high. At higher frequencies the range of values is much wider than the predicted ones. Phases compare very well except at the low frequencies.

Figure 55 and Figure 56 show cross-spectral values (magnitude only) for lateral separations. At Mach 0.74, the low frequency magnitudes and decay rates are comparable; high frequency measured magnitudes are significantly lower. As noted before, at Mach 1.95, the prediction is almost independent of frequency in contrast to the measurements.
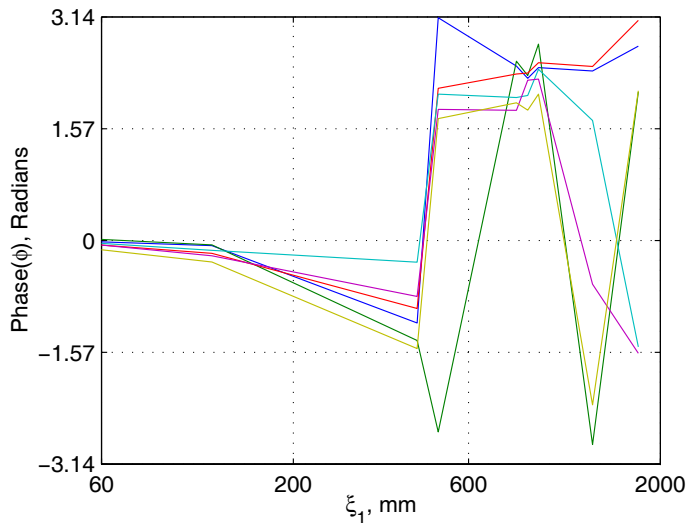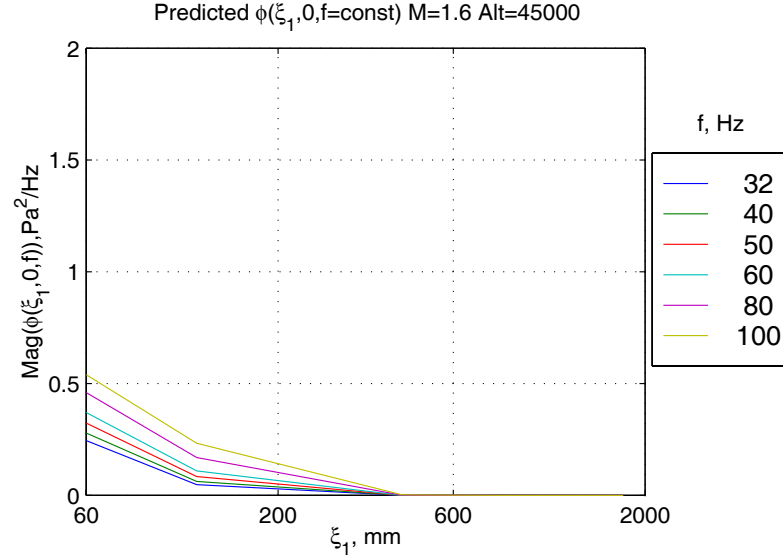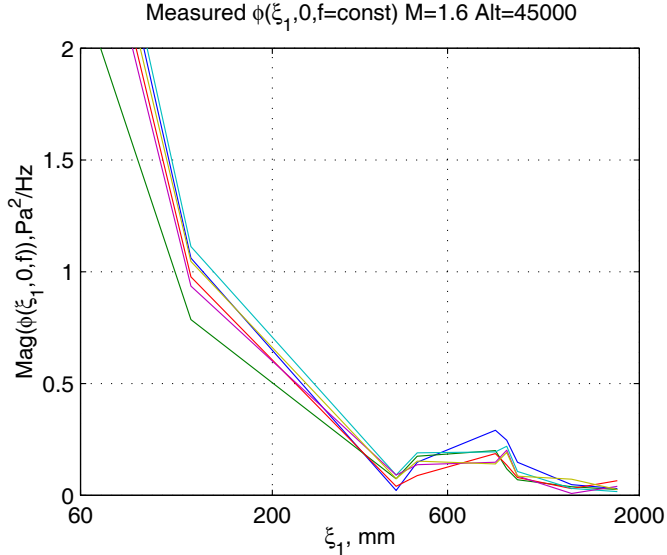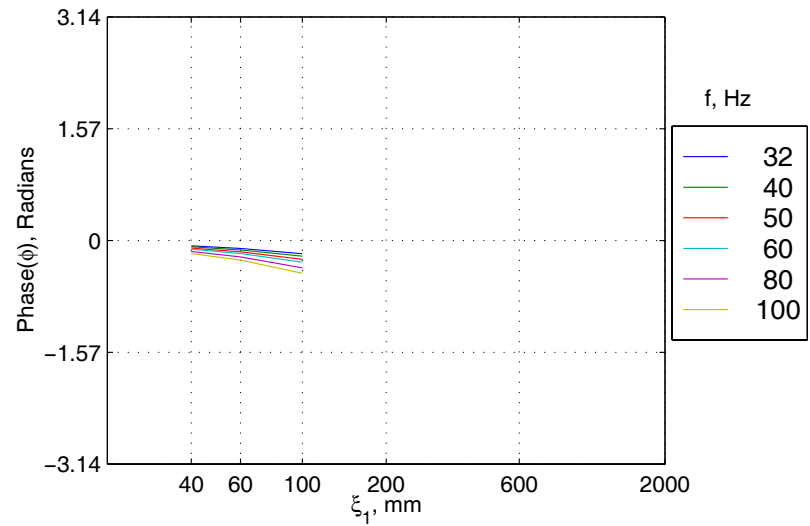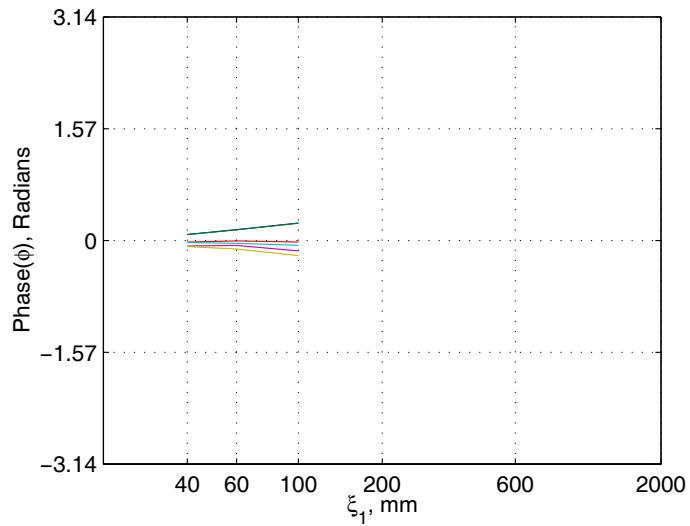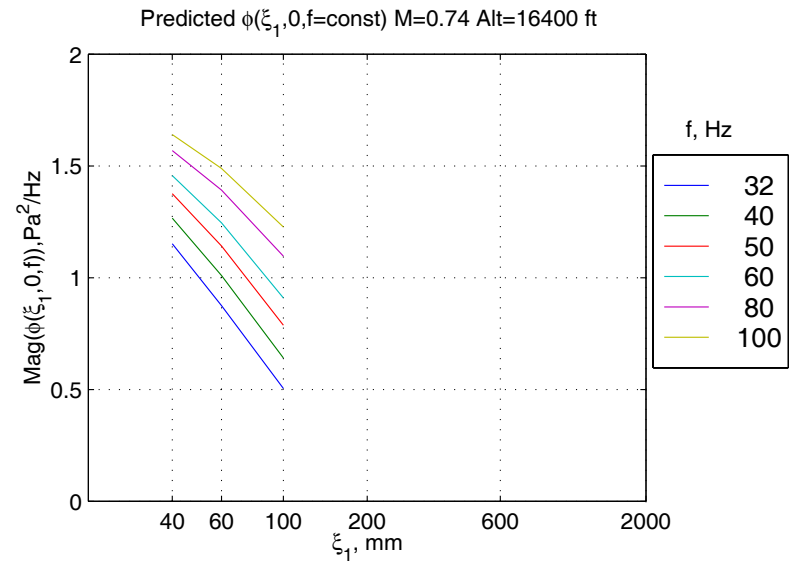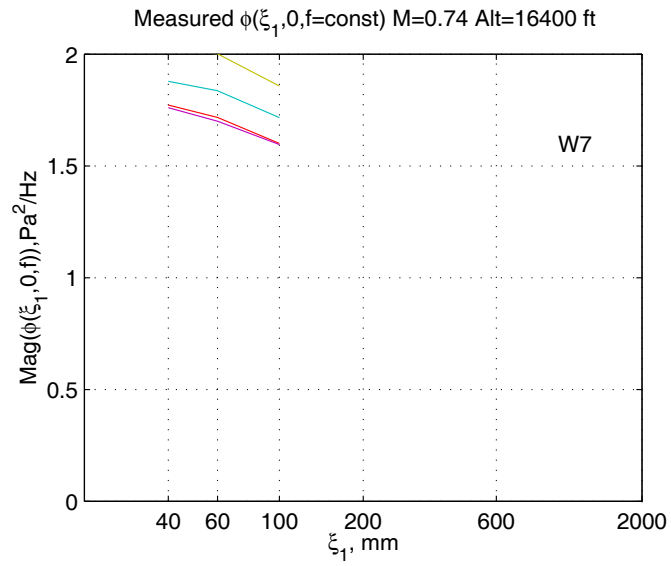
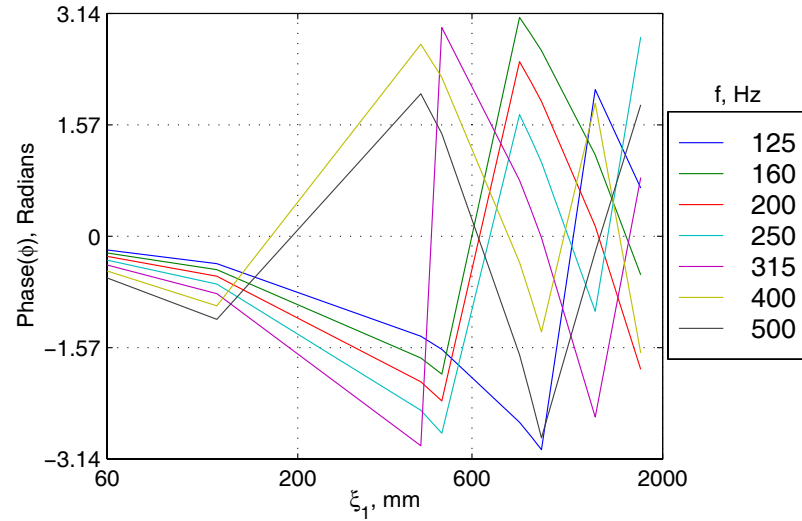**Figure 49 Cross-Spectra - Longitudinal, Window Blank 7, Measured and Predicted at Mach 0.74, 32 to 100 Hz**
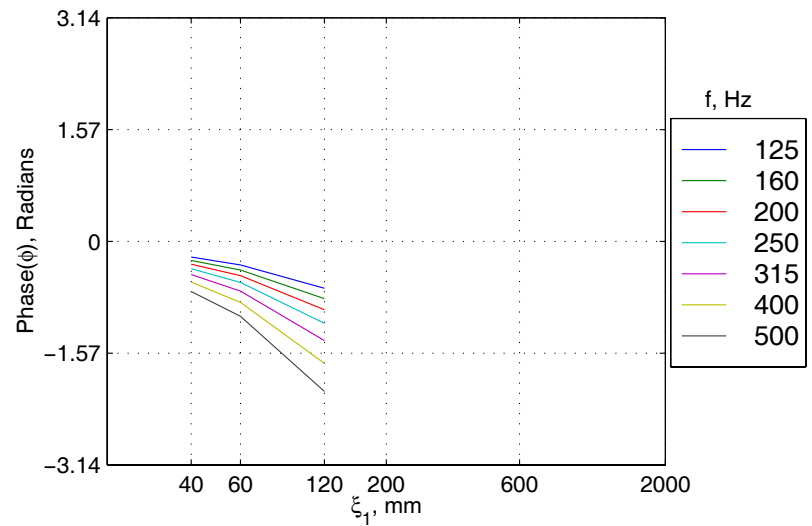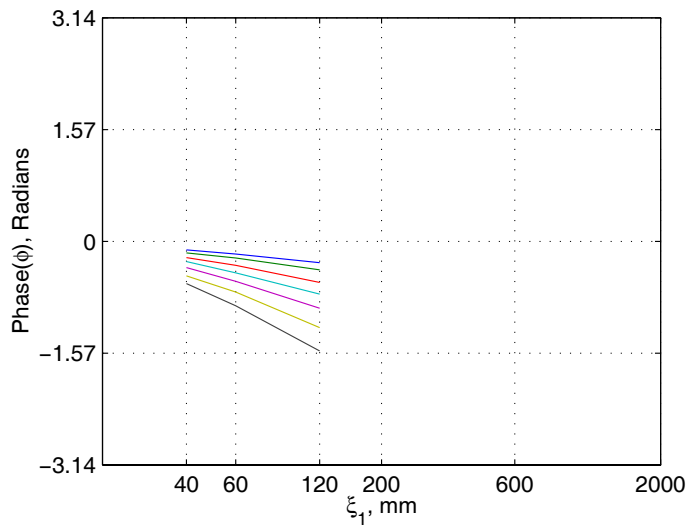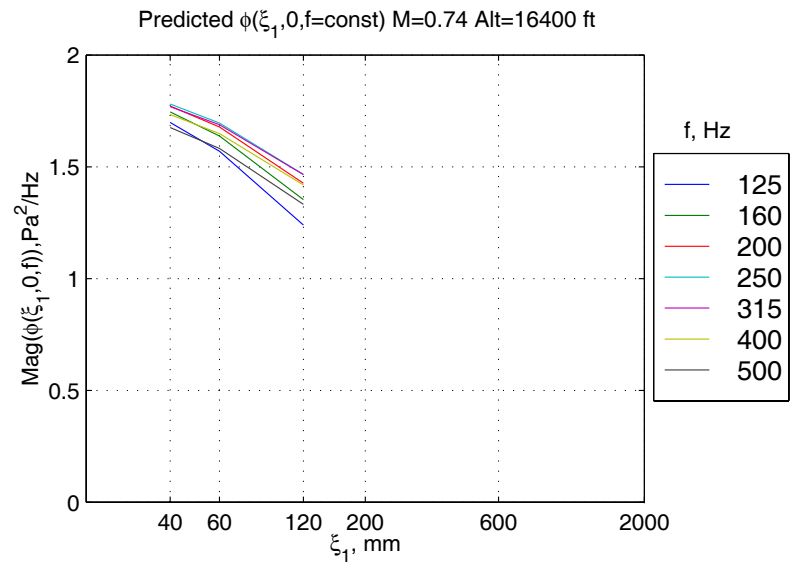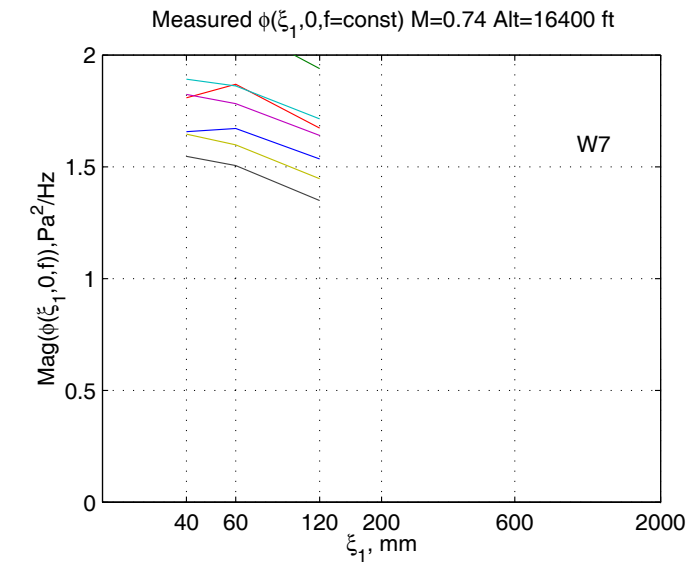
Figure 50 Cross-Spectra - Longitudinal, Window Blank 7, Measured and Predicted at Mach 0.74, 125 to 500 Hz
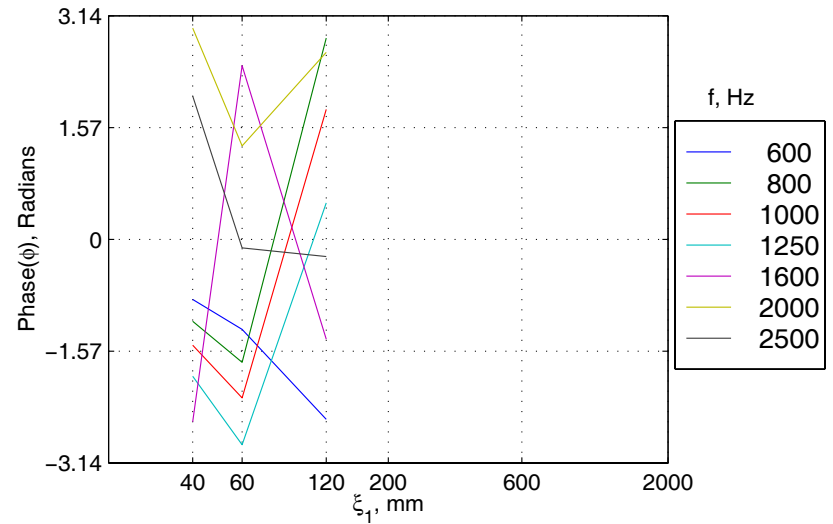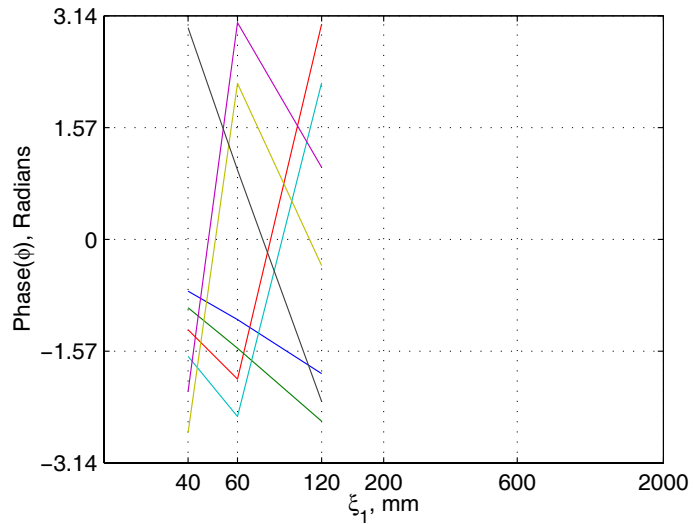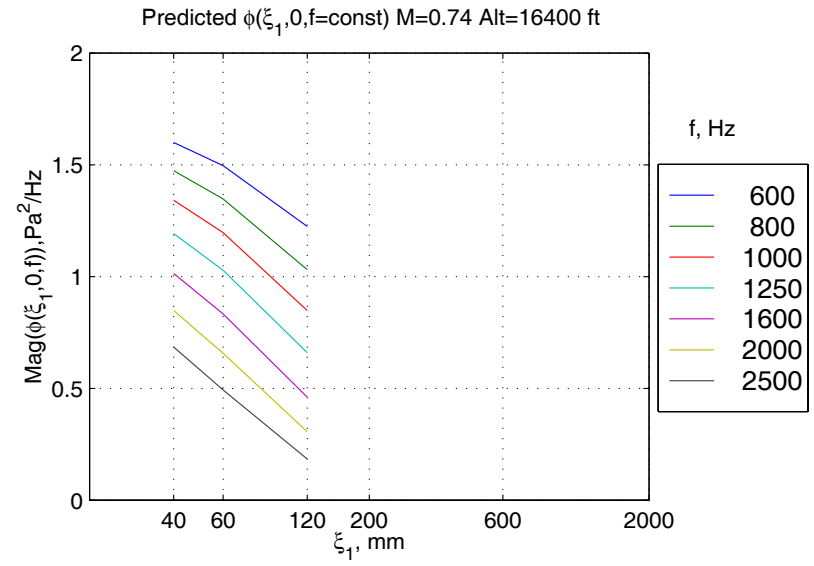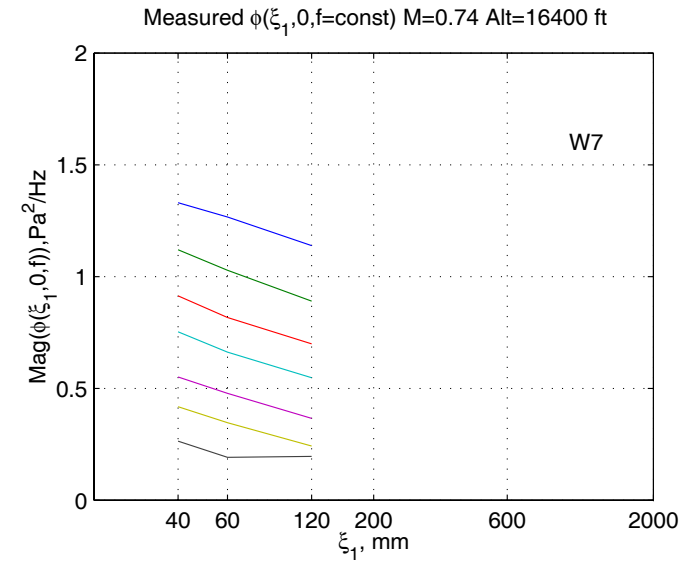
Figure 51 Cross-Spectra - Longitudinal, Window Blank 7, Measured and Predicted at Mach 0.74, 600 to 2500 Hz

55
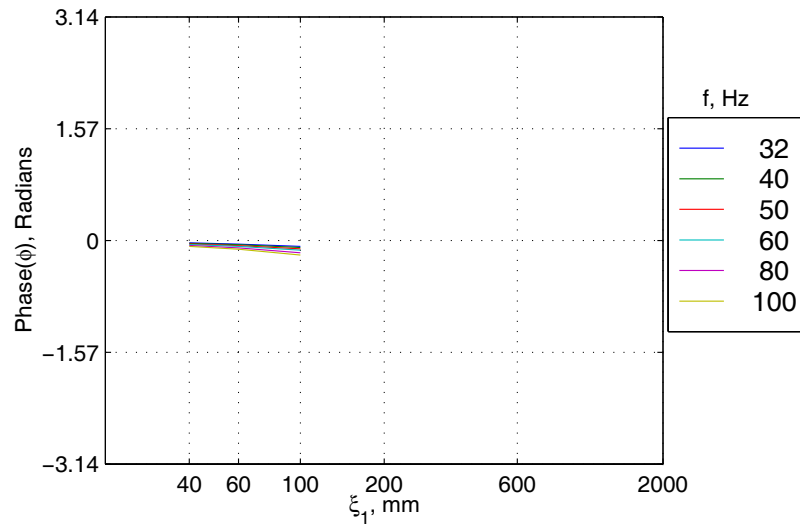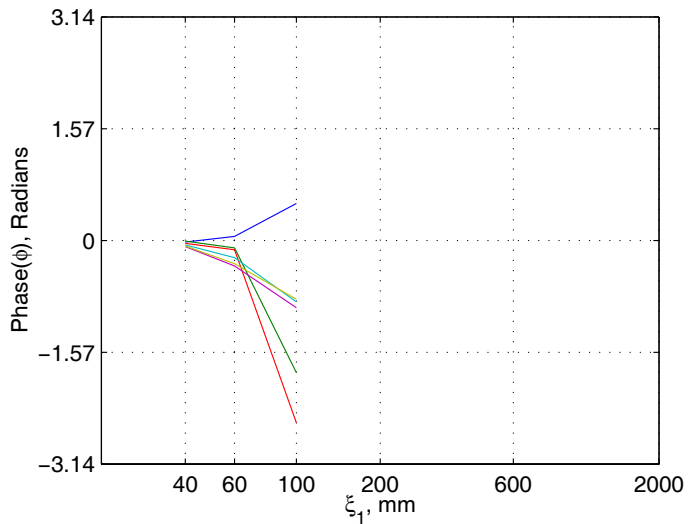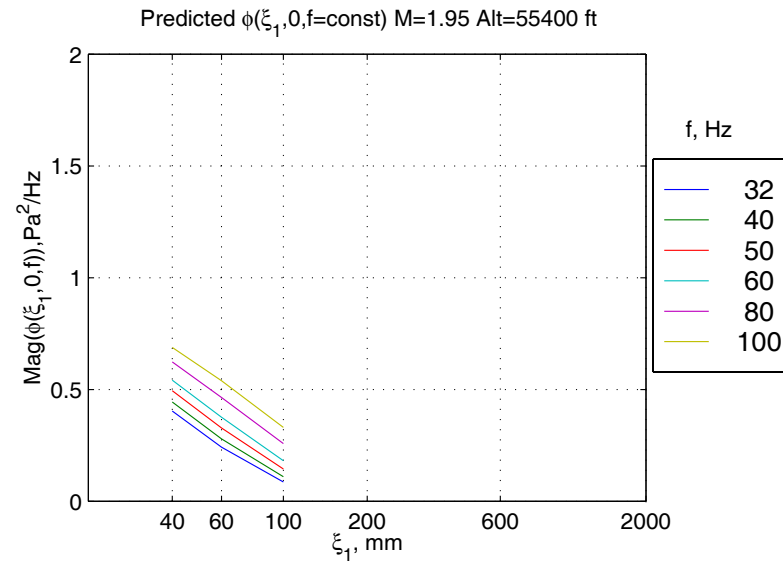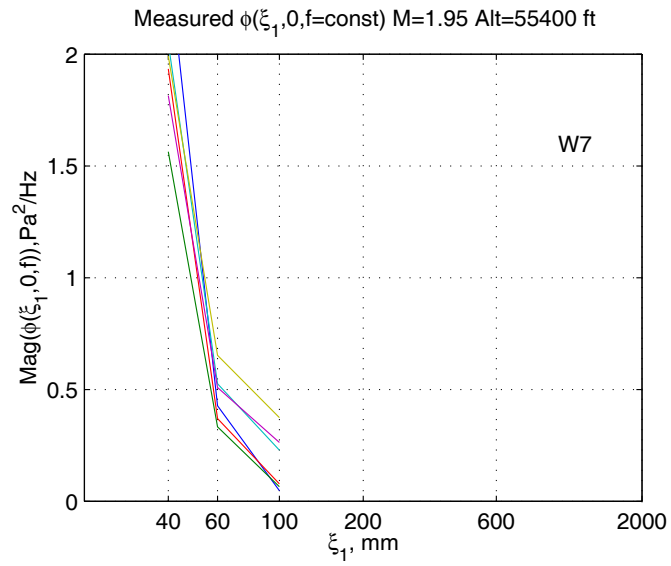
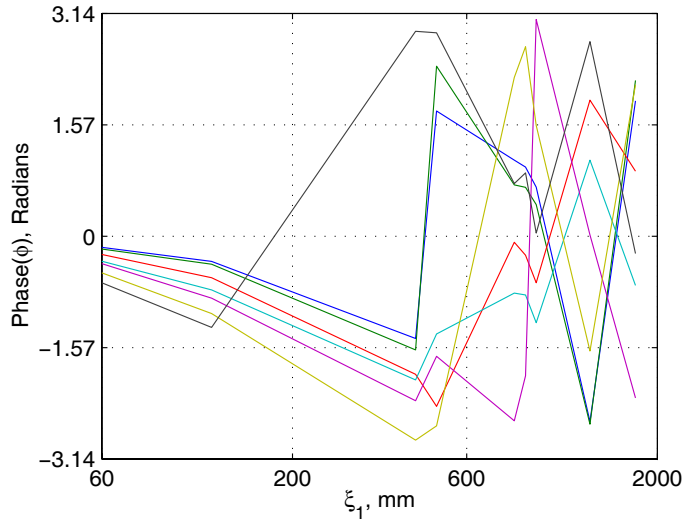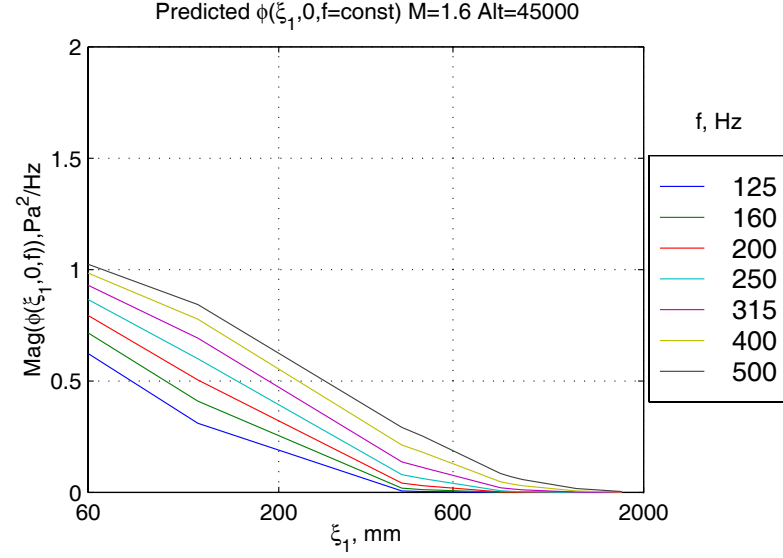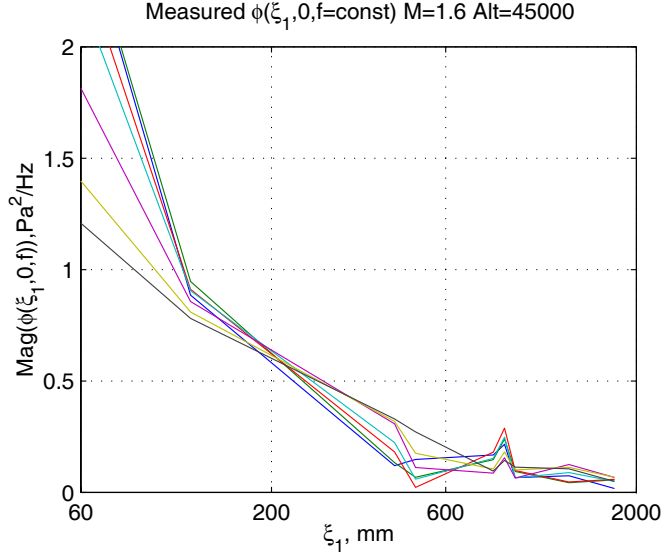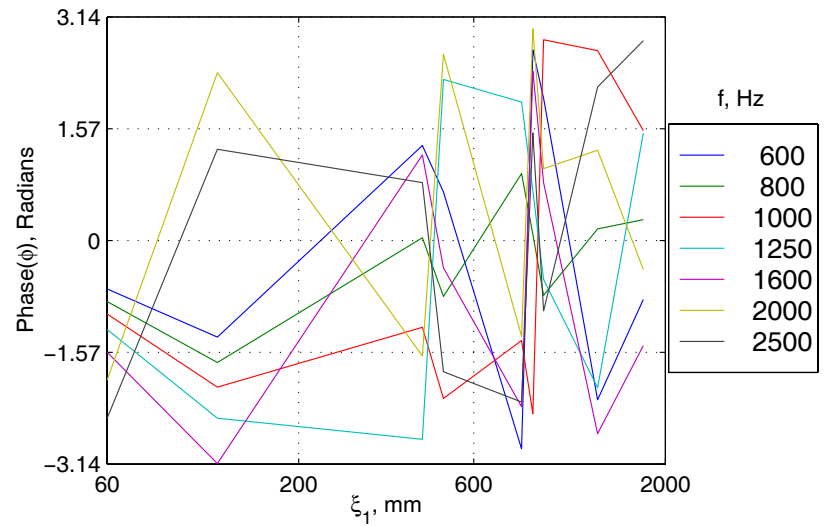**Figure 52 Cross-Spectra - Longitudinal, Window Blank 7, Measured and Predicted at Mach 1.95, 32 to 100 Hz**
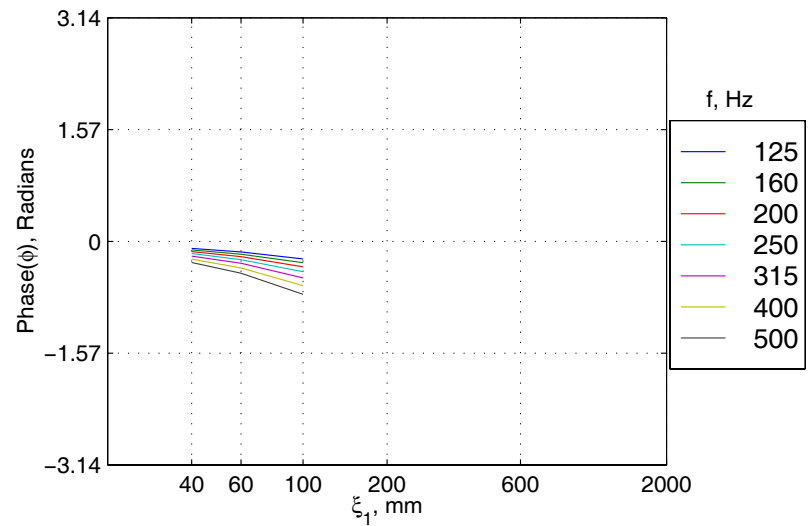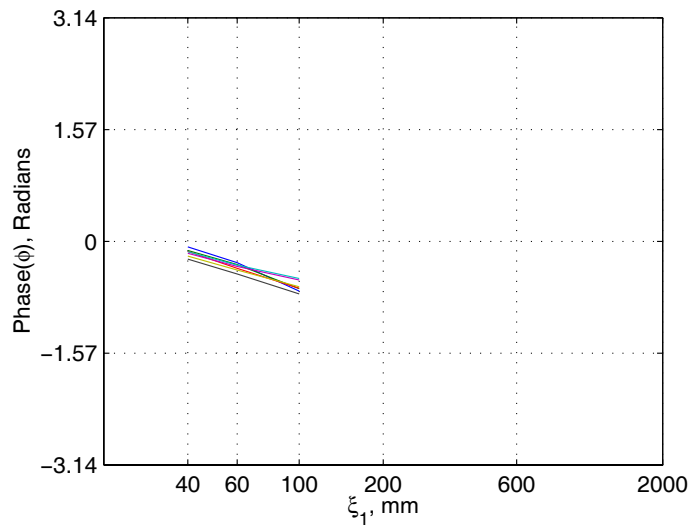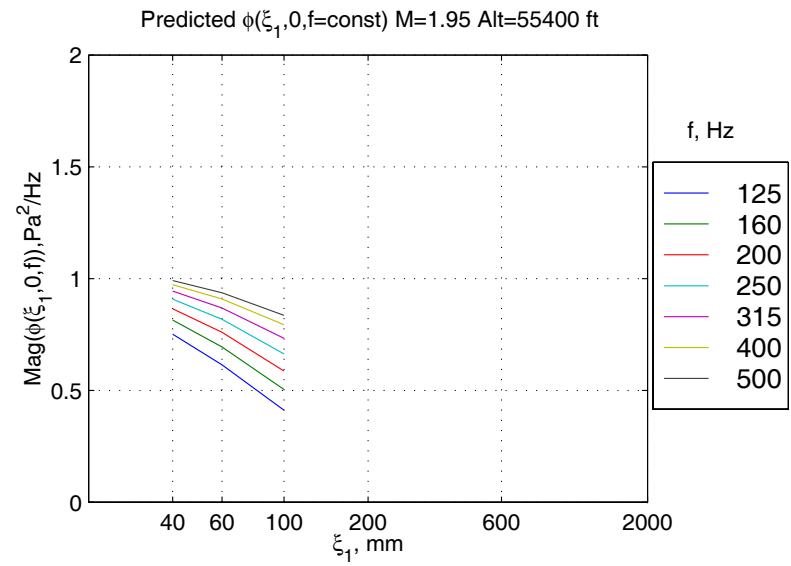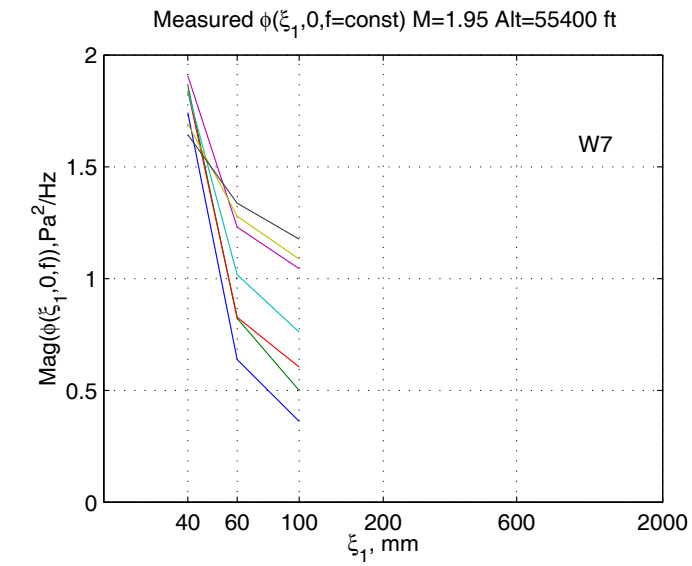
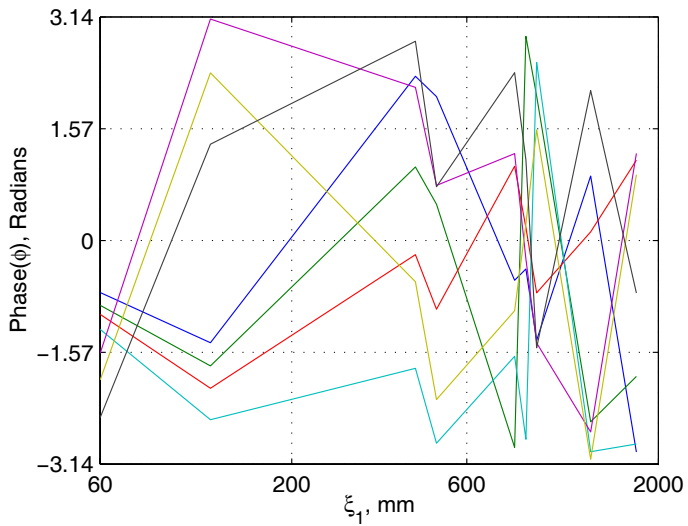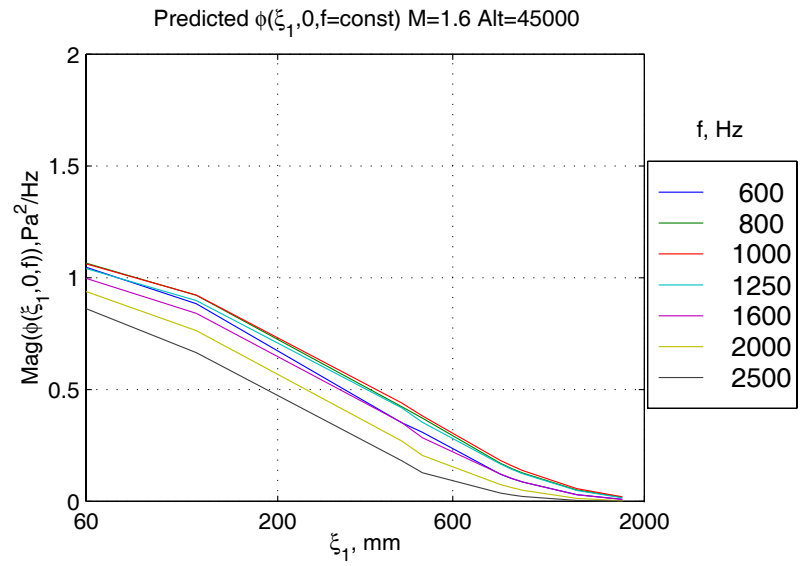**Figure 53 Cross-Spectra - Longitudinal, Window Blank 7, Measured and Predicted at Mach 1.95, 125 to 500 Hz**
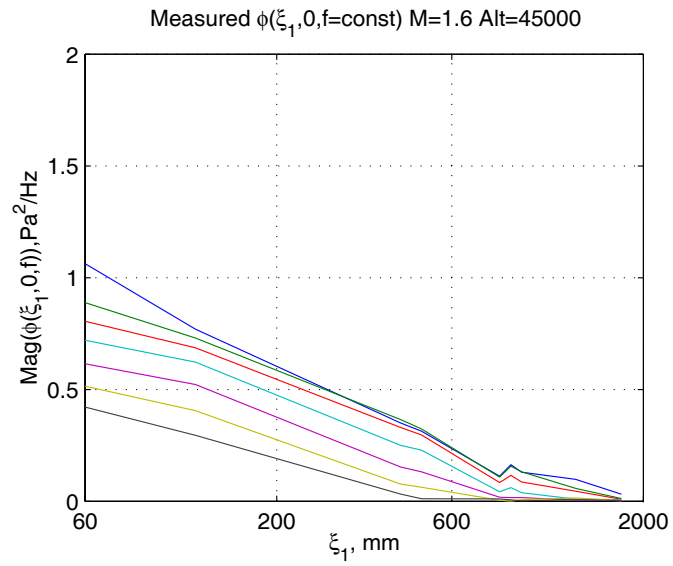
57
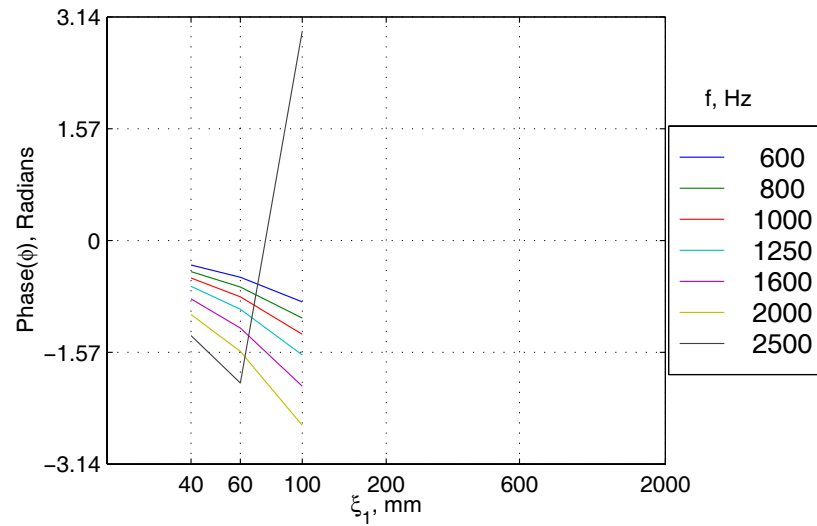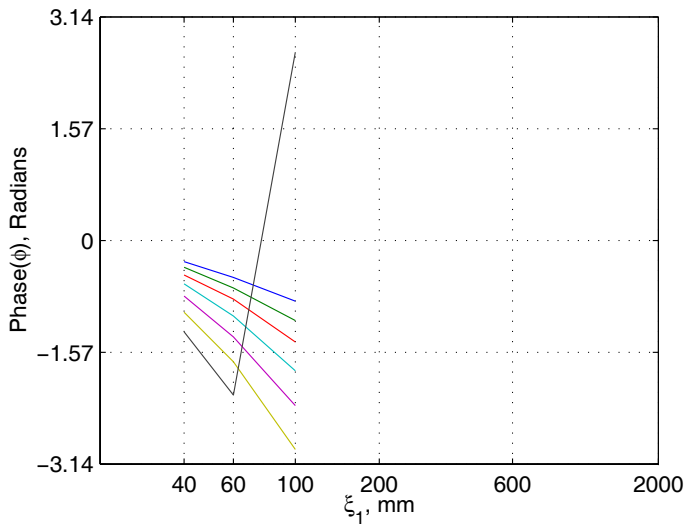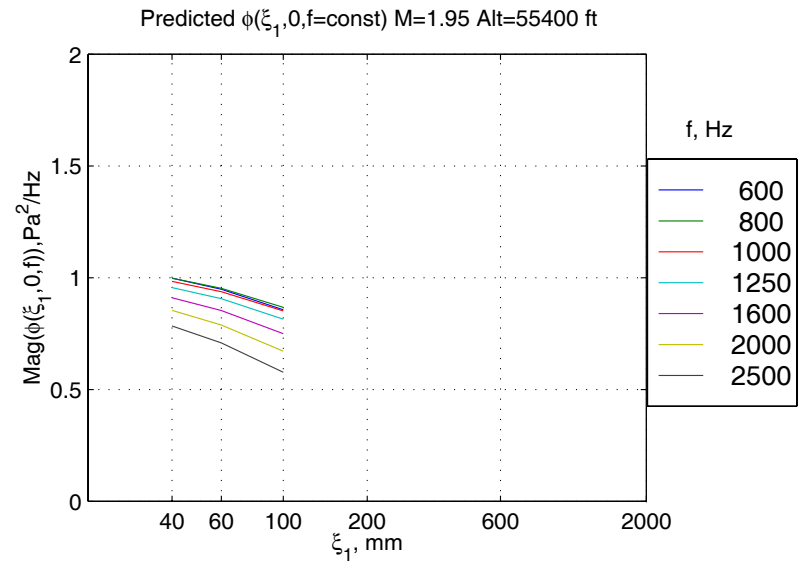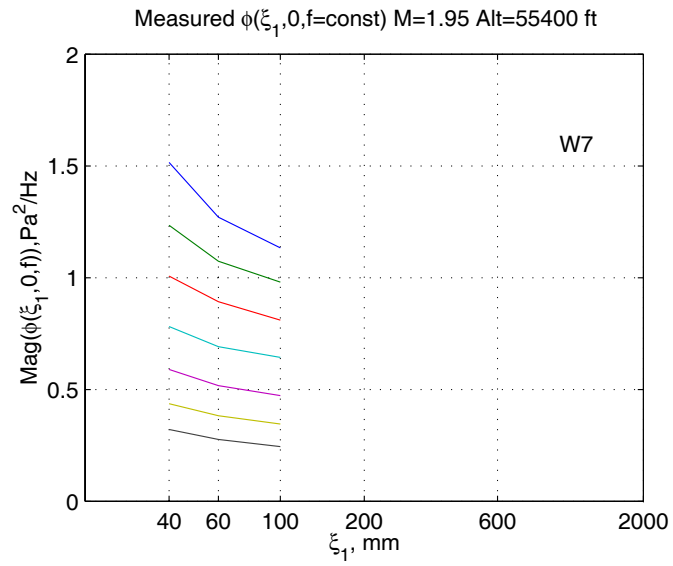
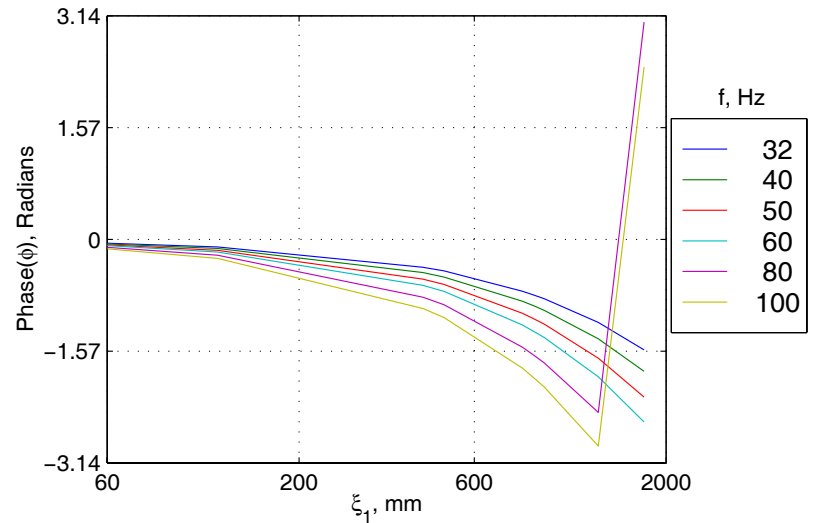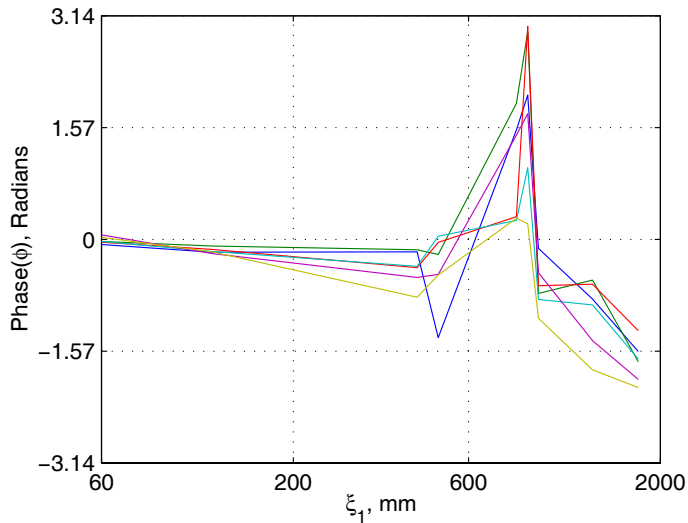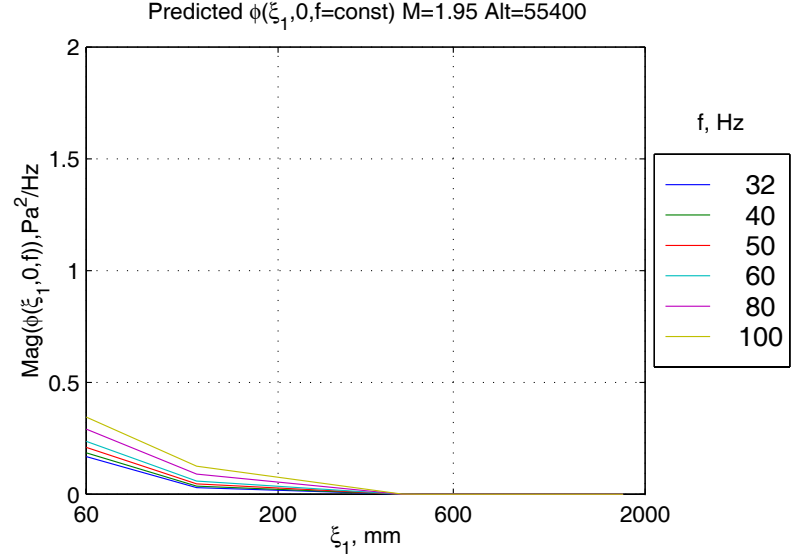**Figure 54 Cross-Spectra - Longitudinal, Window Blank 7, Measured and Predicted at Mach 1.95, 600 to 2500 Hz**
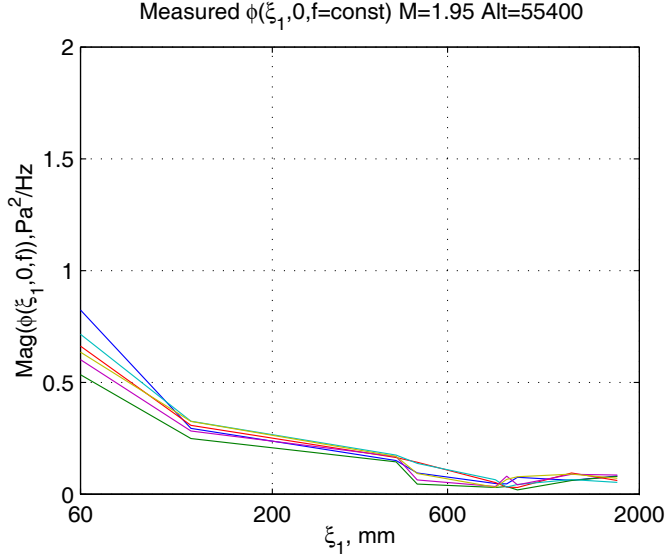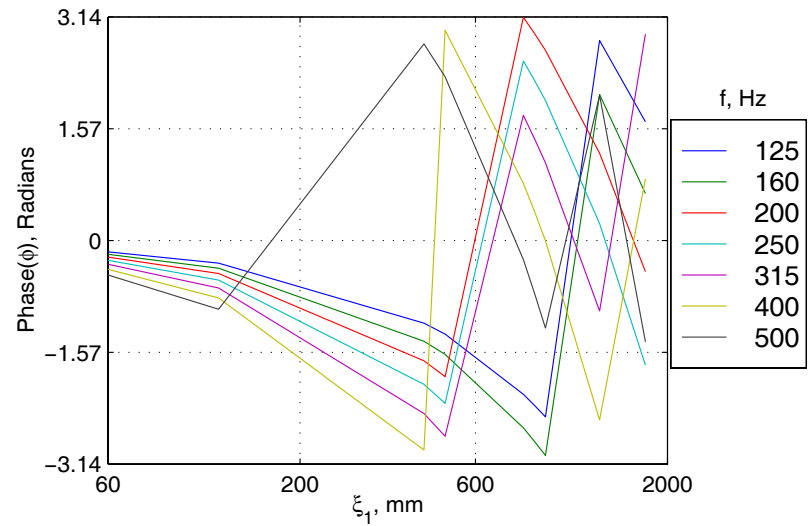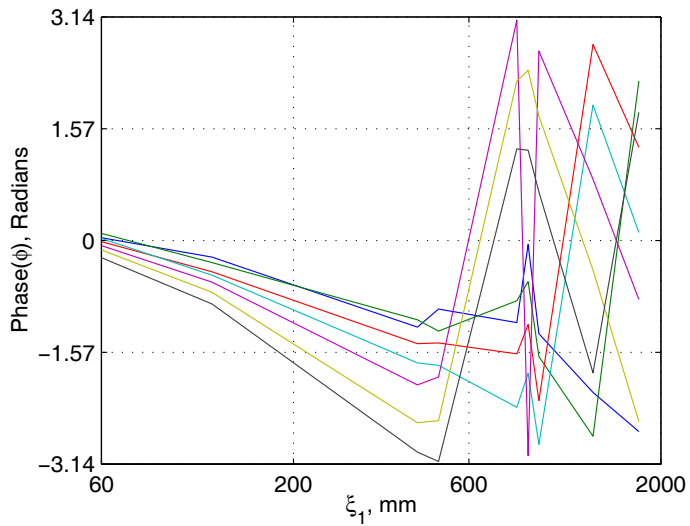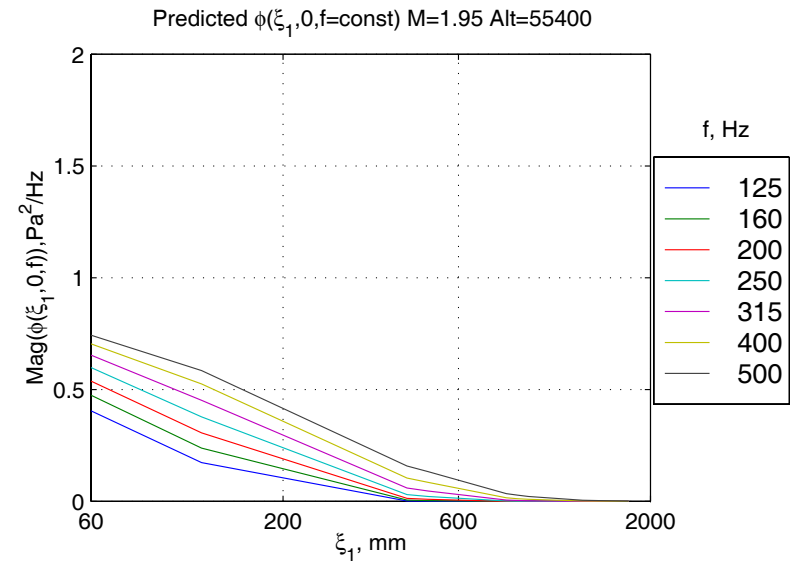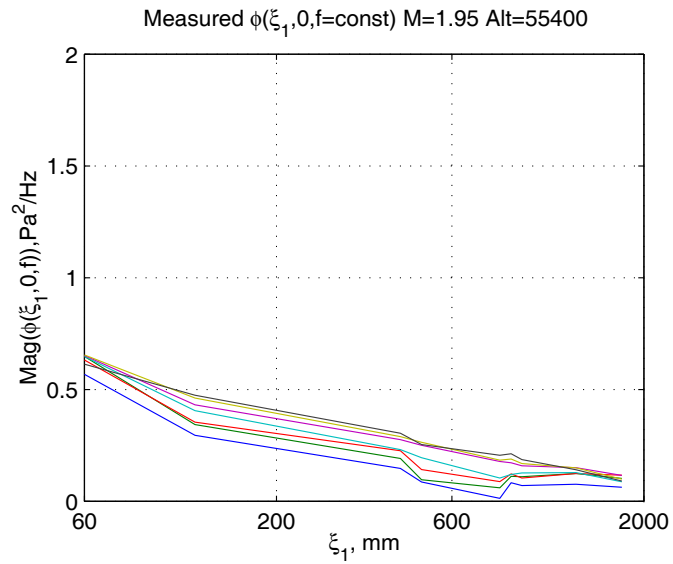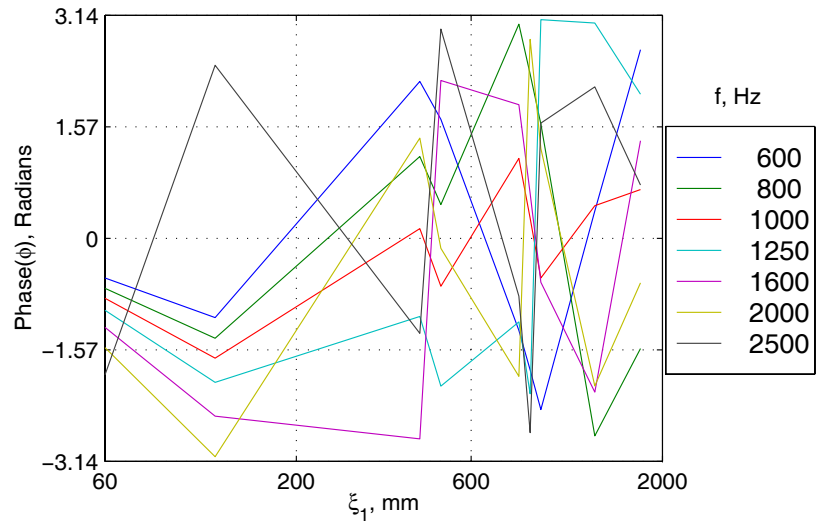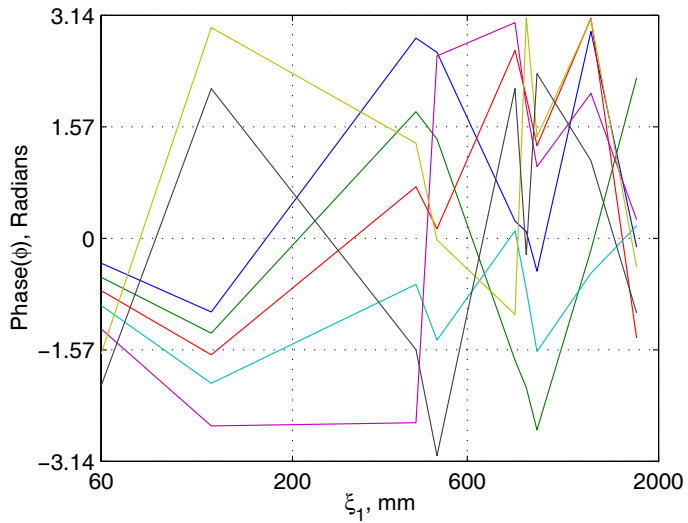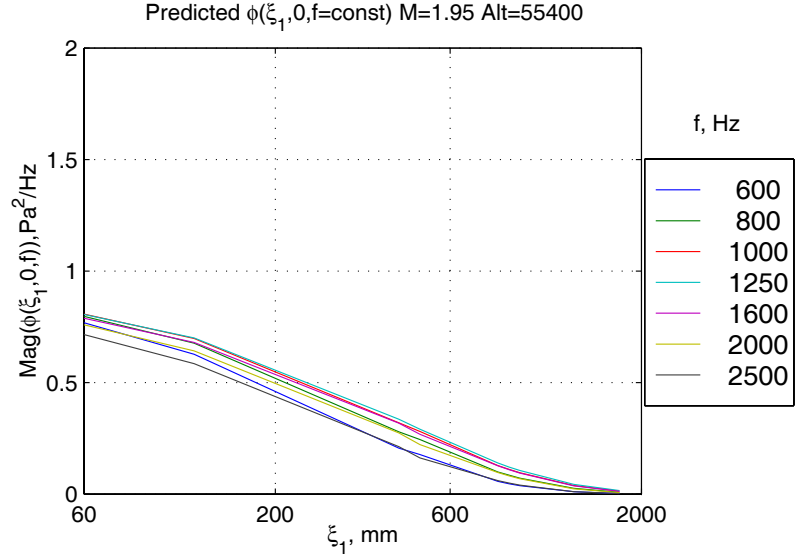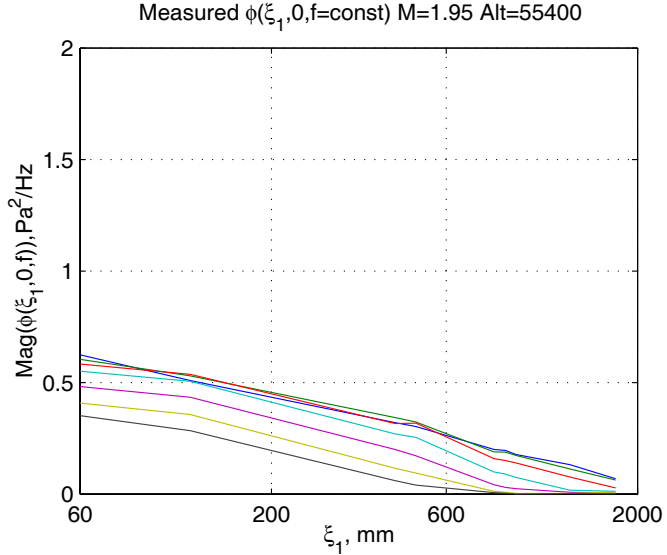
58
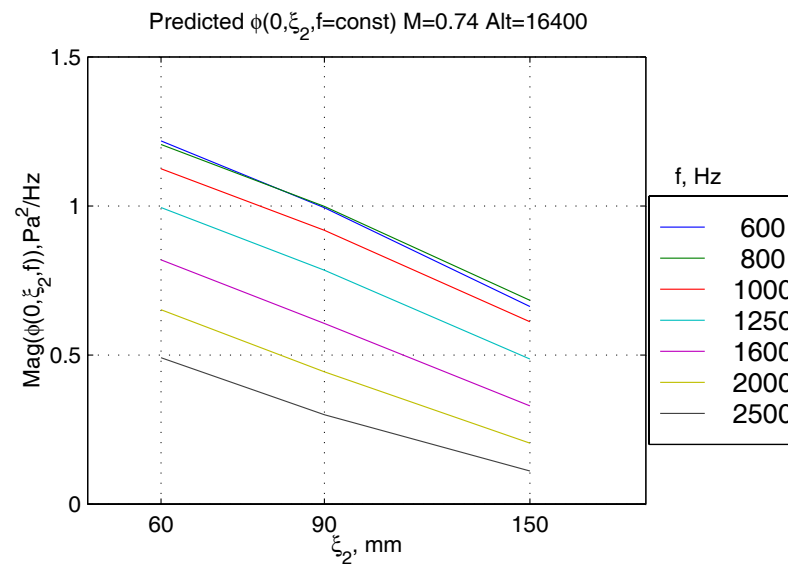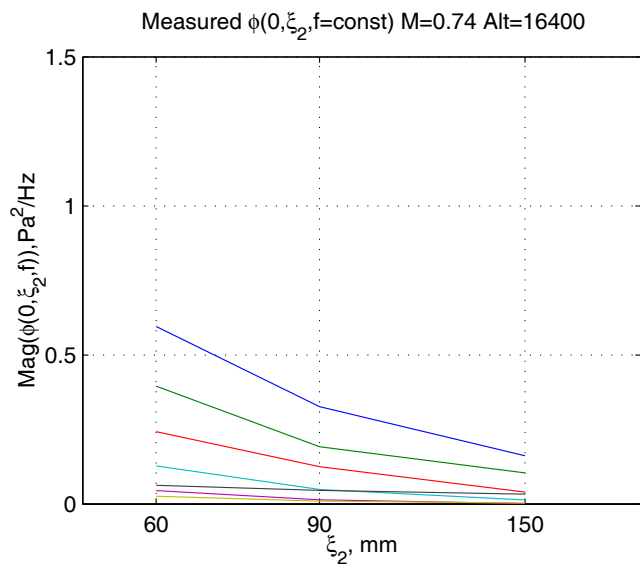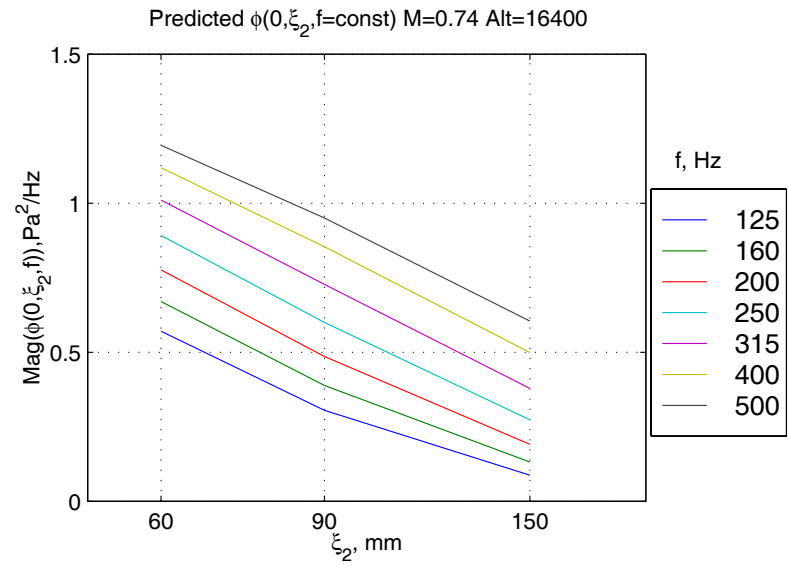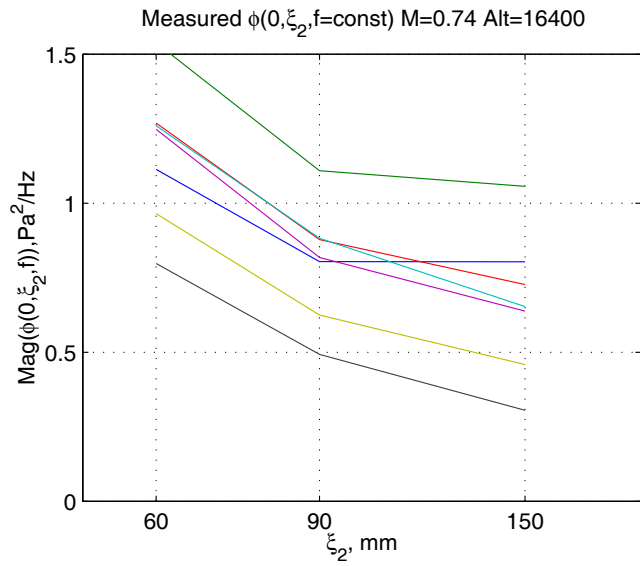
Figure 55 Cross-Spectra - Lateral, Window Blank 7, Measured and Predicted at Mach 0.74
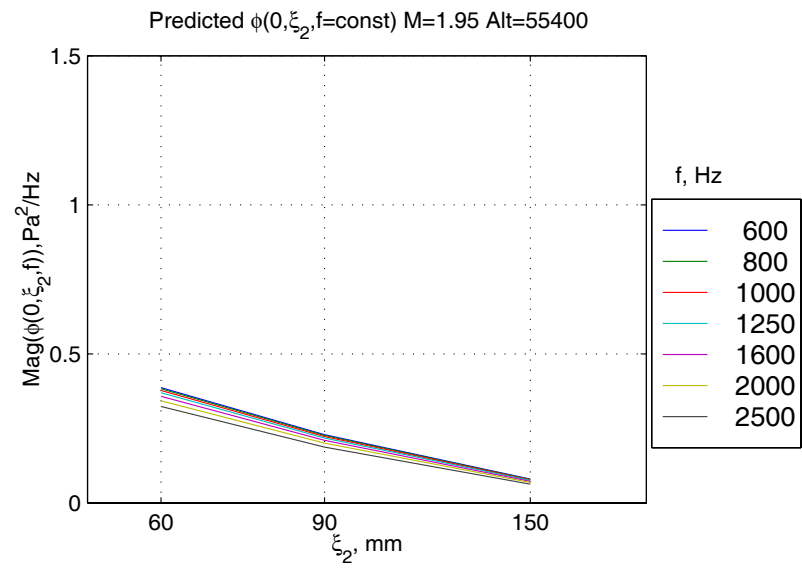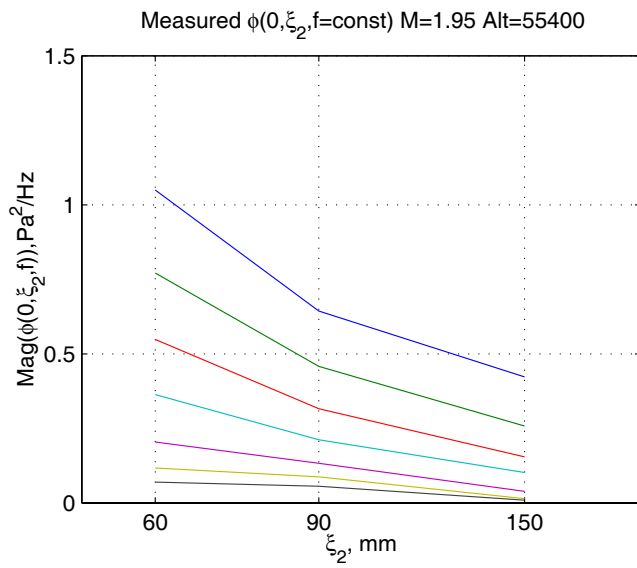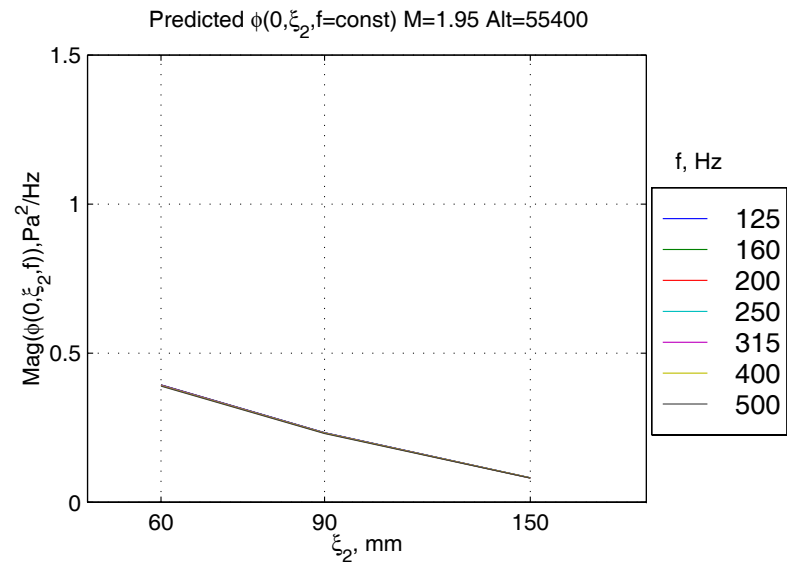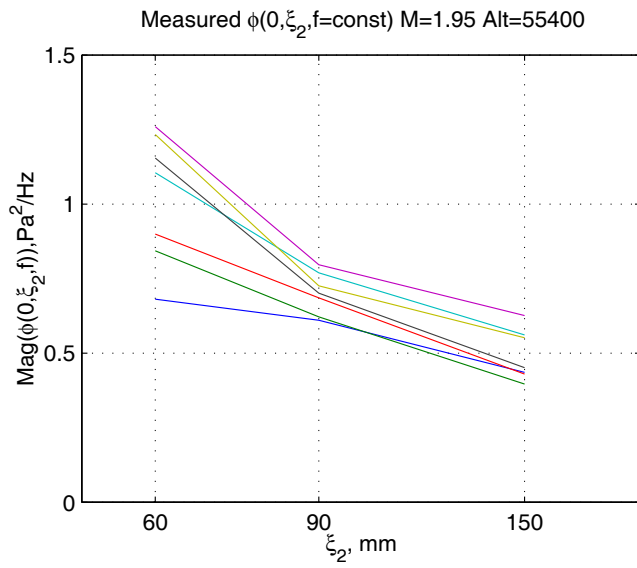
Figure 56 Cross-Spectra - Lateral, Window Blank 7, Measured and Predicted at Mach 1.95

6. Efimtsov Auto Spectrum Model Adjustments

Comparisons of the measured flight data and the predictions from the Efimtsov model showed two characteristics which the Efimtsov model did not predict. The first was a broad band spectral peak around a Strouhal number of 0.6 where the Strouhal number is calculated as $\dfrac{2\pi f \delta^*}{U_0}$. The measured data also showed a slightly steeper roll-off at high frequencies (above 1 kHz) than the predicted roll-off.

6.1 Broad Peak

The broad band peak's magnitude is of the order of 2 dB. In some of the data it is obvious and prominent, in some of the data it is non-existent. Here are arguments for the presence of the broad peak:

- Intuitively, one would expect that certain frequency regions would contribute more strongly to turbulence energies according to the length scales imposed on the flow by the boundary layer thickness; such behavior has been shown to exist for free shear layers in jet plumes. The measured data's behavior supports this reasoning by exhibiting its spectral peak at a constant Strouhal number.

- Schewe [Ref. 16] shows a figure (here reproduced as Figure 57) with spectra that exhibit the broad spectral peak.
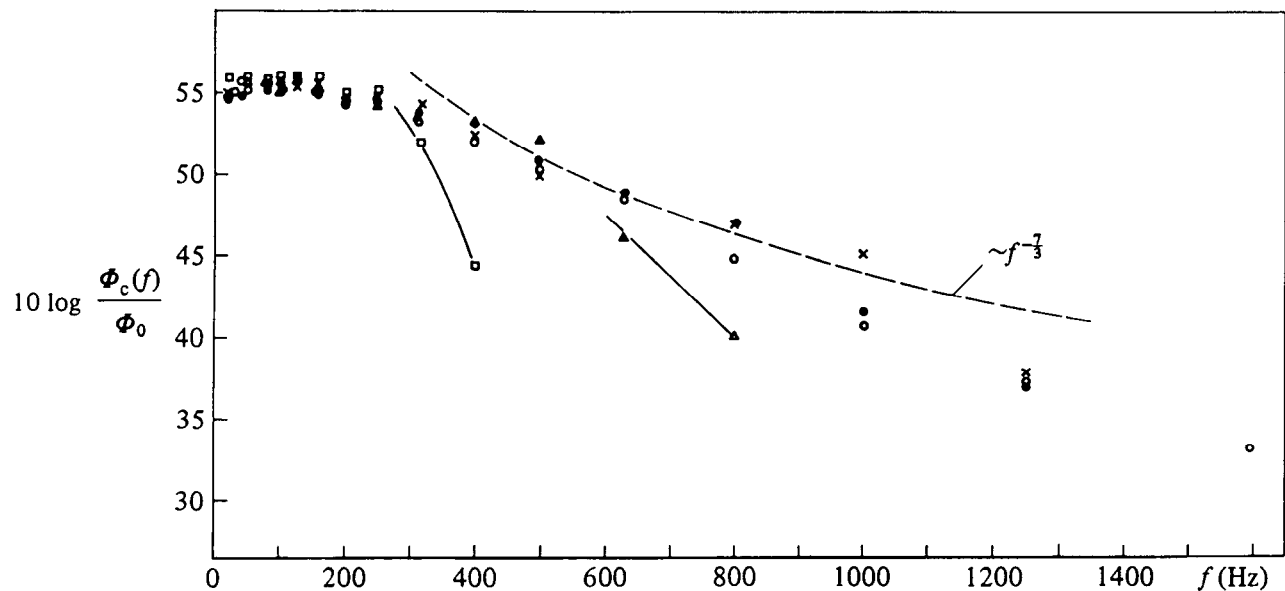
Figure 57 Excerpt from Ref. 16: *'Corrected power spectral densities ...'*

- The scatter in the low frequency auto spectral data can be attributed - at least in part - to transducers not being completely flush mounted. Efimtsov's [Ref. 8] wind tunnel data indicates that the probability is higher of measuring a higher level due to flushness deviations than one below the 'true' value. One might therefore believe the lower portion of the scattered points more, leading to the broad peak asserting its presence.

61

- The low frequency data for window blanks in the back of the aircraft may be contaminated by engine noise, air as well as structure borne, leading to higher measured levels than would be measured in a 'pure' boundary layer.

Here are arguments against the presence of the broad peak:

- The broad peak's magnitude is small; it is within the scatter of the data.

- The majority of past models exhibit no broad peaks (the exception is the ESDU model).

To the authors, the arguments 'for' the peak were more compelling. Therefore, a procedure was developed to add an appropriate adjustment to Efimtsov's model. The peak occurs in a frequency region which is weighted strongly in human response to noise metrics for interior noise; it is therefore important to model loads there as accurately as possible.

6.2 High Frequency Roll-Off

The Efimtsov model predicts a much shallower high frequency negative slope than all other models, as well as the TU-144LL data. We decided to adjust the Efimtsov model to follow the TU-144LL after correcting for transducer size (see Section 4, 'Data Correction').

6.3 Efimtsov Adjustment Functions

Two analytical functions were used to adjust the predicted curves to more accurately reproduce the measured SPL spectra.

The broadband peak was modeled by a log-normal distribution equation:

$$C_1 \exp\left(-\left(\log(St) - \log(St_1)\right)^2\right)$$

where St is the Strouhal number, and St_1 is a reference value.

To account for the slope of the high frequency roll-off, another function is added to the prediction equation. The Efimtsov model over-predicts for flight conditions below Mach 1.65 and under-predicts for conditions above 1.65 which leads to the following adjustment function:

$$(M - 1.65)\log_{10}(f)$$

Since only the high frequency slope needs adjustment, a tanh function centered at 1000 Hz is included. The final adjustment equation is:

$$\Phi(f)_{adjusted} - \Phi(f)_{predicted} =$$

$$2.5\exp\left(-\left(\ln\left(\frac{2\pi\delta^*}{U_0}(f)\right) - \ln(0.6)\right)^2\right) + \frac{1}{4}\left(\tanh\left(\log_{10}\left(f/1000\right)\right) + 1\right)(M - 1.65)\log_{10}(f)$$

Figure 58 shows an example of this function.
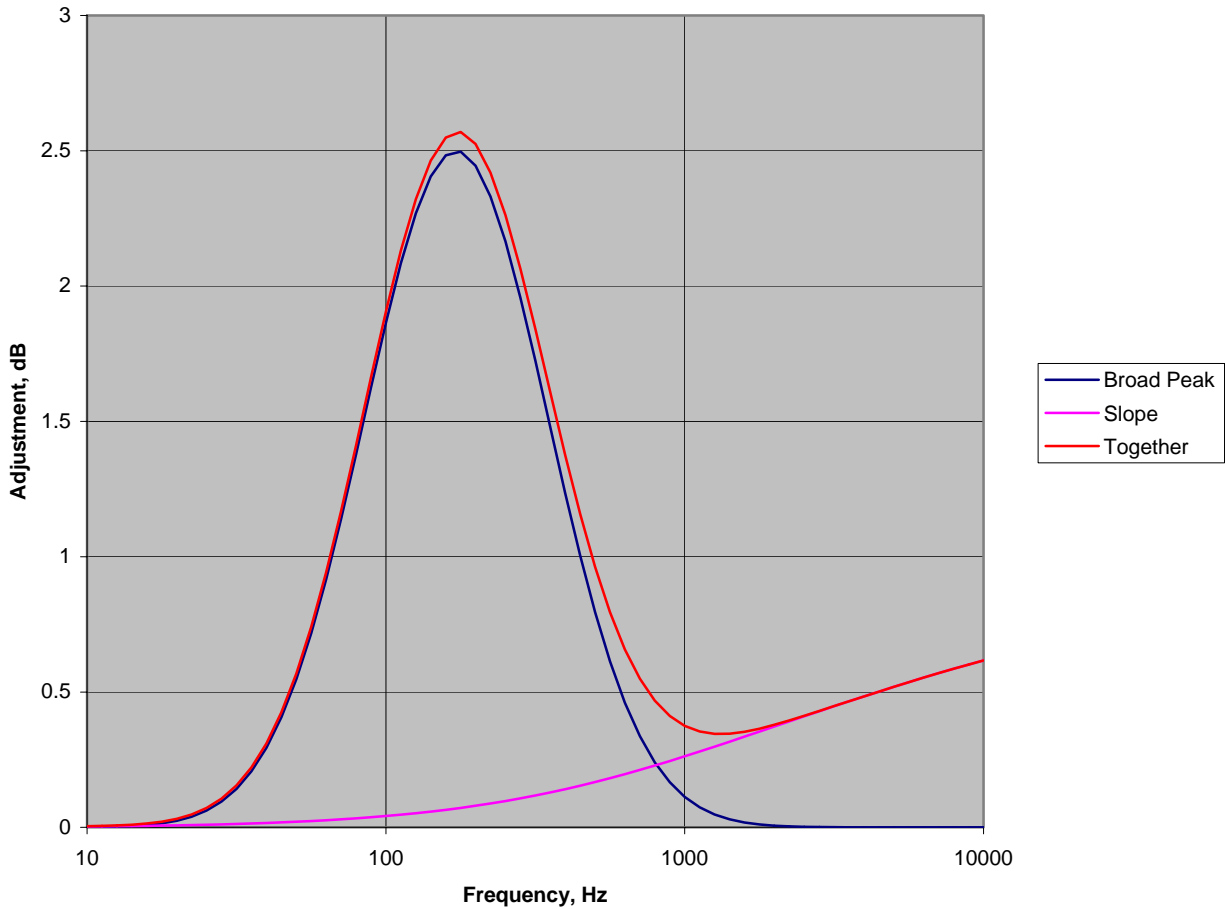
Figure 58 Sample Adjustments for Mach 2, $\delta^* = 1 ft$, U₀=1800 fps.

Figure 59 shows the original Efimtsov model and the adjusted model for Mach 1.95 55,400ft flight condition as well as measured flight test data. Other conditions are shown in Figure 60 - Figure 64.

6.4 Comparisons of Adjusted Efimtsov Prediction to Measured TU-144LL Data

Some observations:

- The adjusted model follows the measured data better on forward and center window blanks than on the aft.

- The high frequency roll-off of the data is well modeled, except that the model does not follow a data trend where further aft sensors exhibit a greater high frequency slope, crossing over the spectra of further forward sensors.

- At low frequencies, no adjustments were made to the Efimtsov model because there was no trend to be found in the widely scattered data.
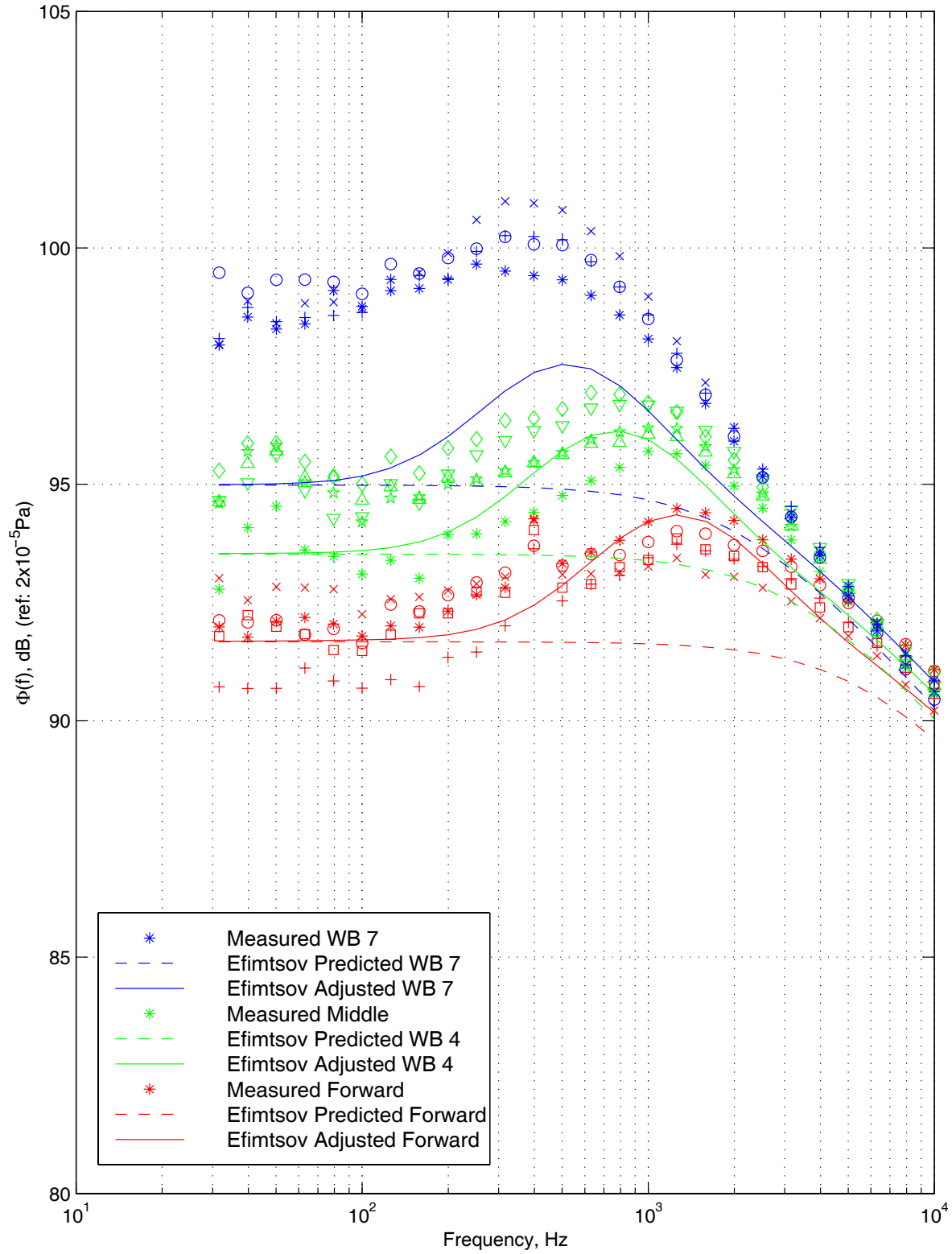
Figure 59 Adjusted Efimtsov Model and In-Flight SPL Data (M 1.95, 55,400 ft, Window Blanks 1, 4, and 7)
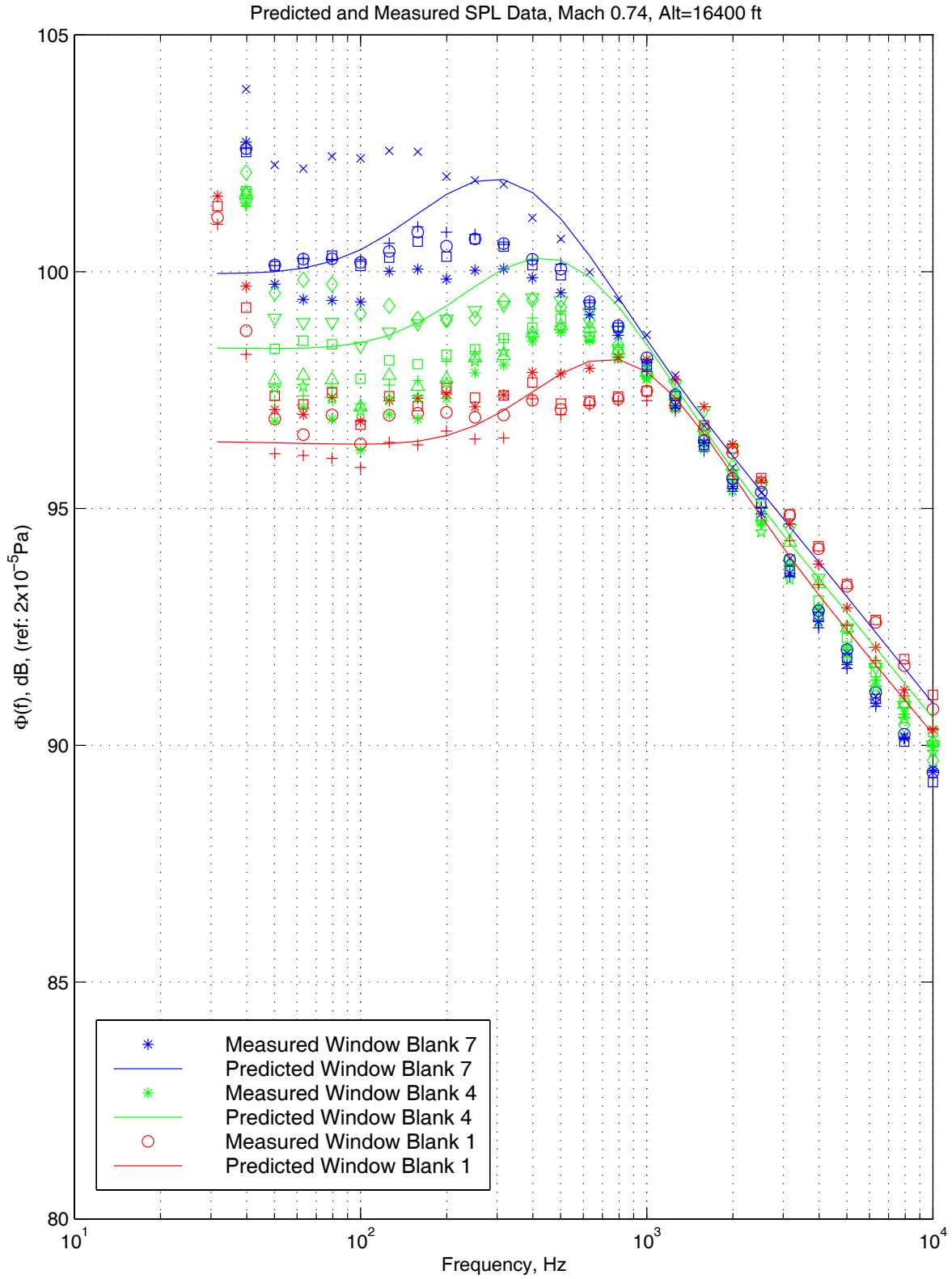
Figure 60 Adjusted Efimtsov Model and Tu144 In-Flight SPL Data (M 0.74, 16,400 ft, Window Blanks 1, 4, and 7)
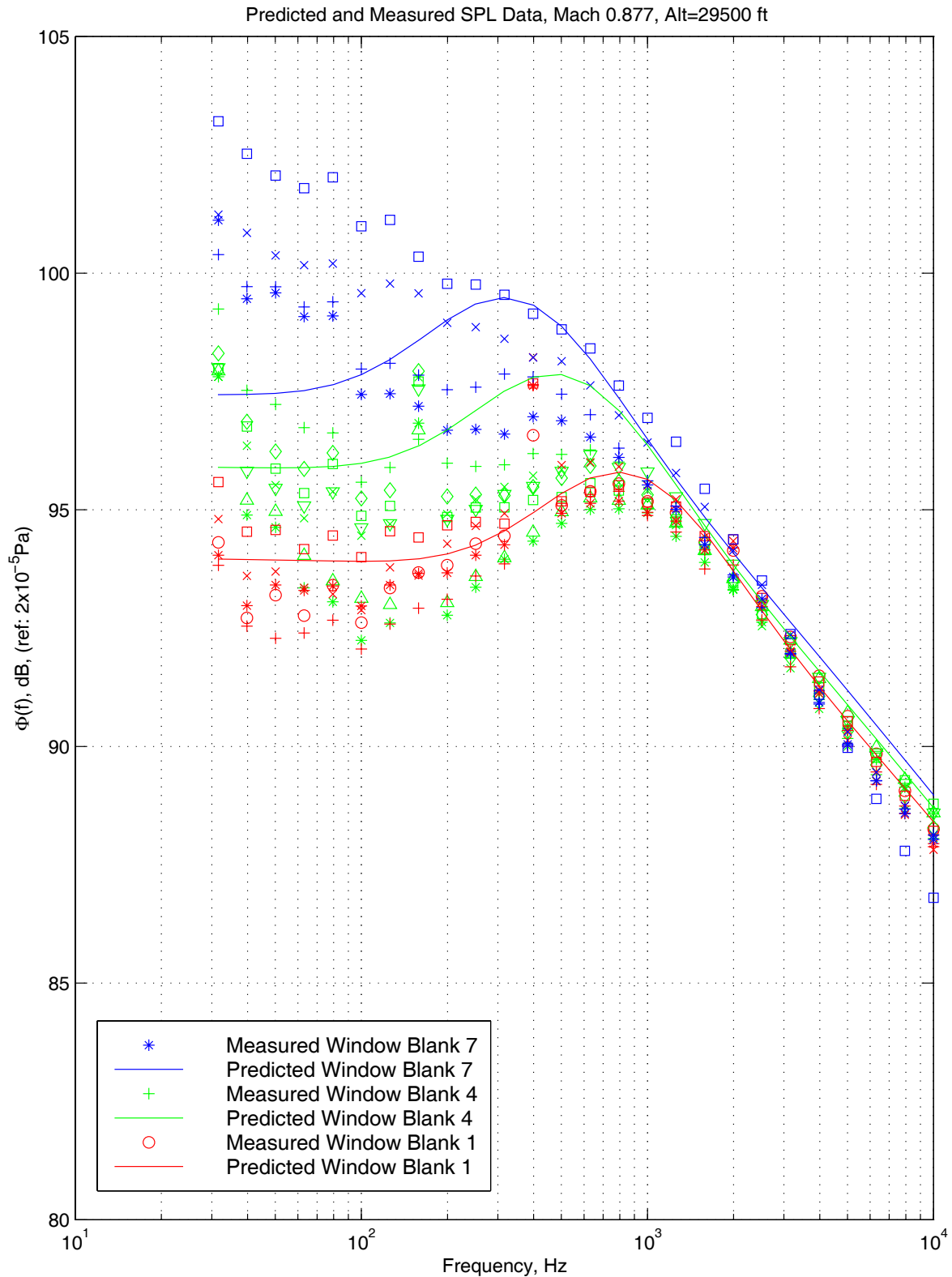
Figure 61 Adjusted Efimtsov Model and Tu144 In-Flight SPL Data (M 0.88, 29,500 ft, Window Blanks 1, 4, and 7)
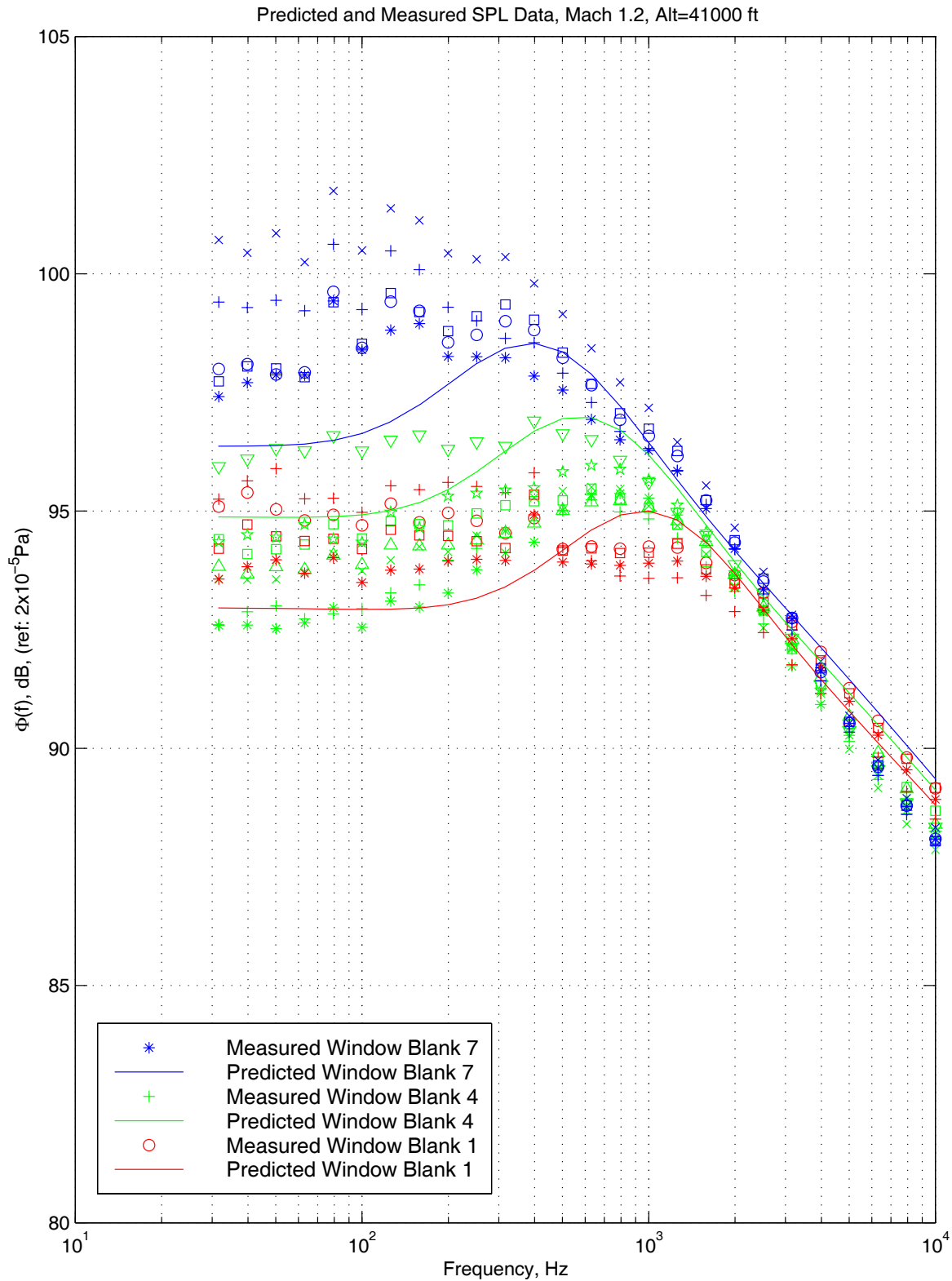
Figure 62 Adjusted Efimtsov Model and Tu144 In-Flight SPL Data (M 1.2, 41,000 ft, Window Blanks 1, 4, and 7)
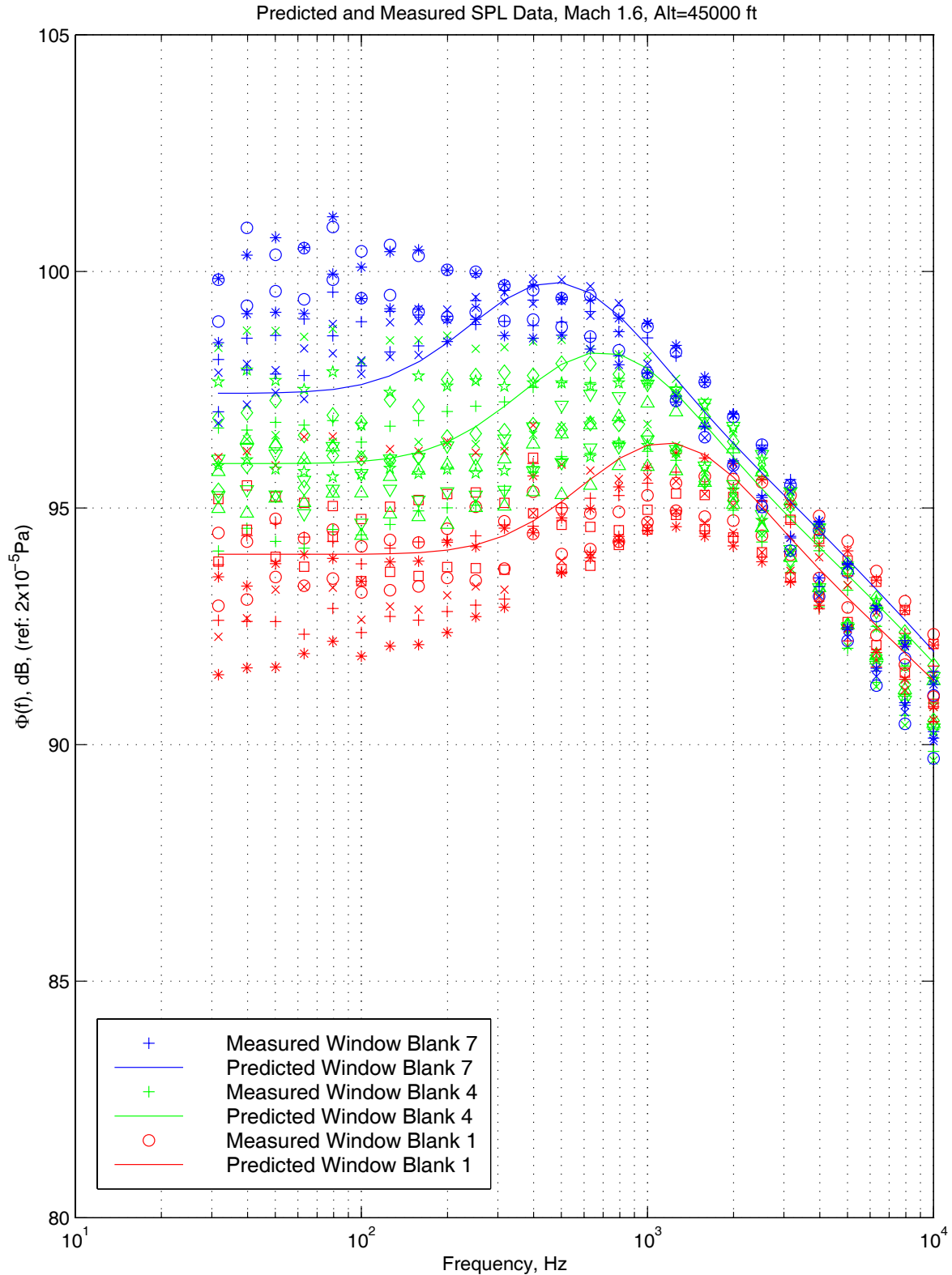
Figure 63 Adjusted Efimtsov Model and Tu144 In-Flight SPL Data (M 1.6, 45,000 ft, Window Blanks 1, 4, and 7)
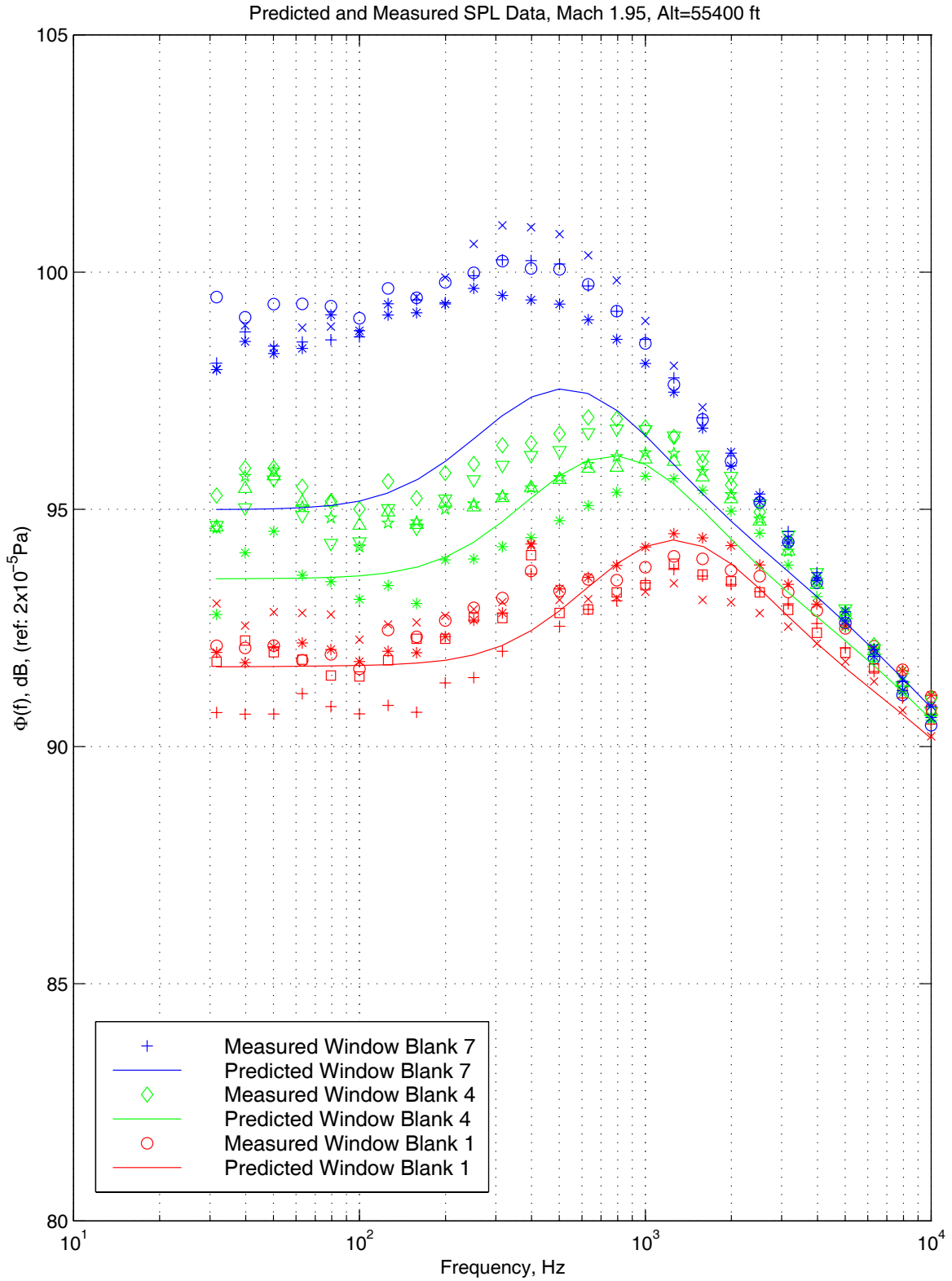
Figure 64 Adjusted Efimtsov Model and Tu144 In-Flight SPL Data (M 1.95, 55,400 ft, Window Blanks 1, 4, and 7)

6.5 Comparison to Other Flight Test Data

A comparison of other measured data could be used in order to determine if the adjustments are specific to the NASA-Boeing Tu144LL test or if the adjustments could be applied to all flight vehicles. The existing supersonic flight data is limited to the Concorde [Ref. 9], and XB-70 [Ref. 8]. Several sources of wind tunnel data exist but will likely be of limited use for direct comparison purposes.

Figure 65 shows the adjusted Efimtsov predicted SPL and those measured on the Concorde [Ref. 9]. A broad spectral peak seems to be present in the Concorde data as well. The gross outlier in window blank 2 probably needs to be attributed to a flushness problem. If the Corcos correction were to be applied to the Concorde data the measured and predicted high frequency roll-offs would match a lot better.
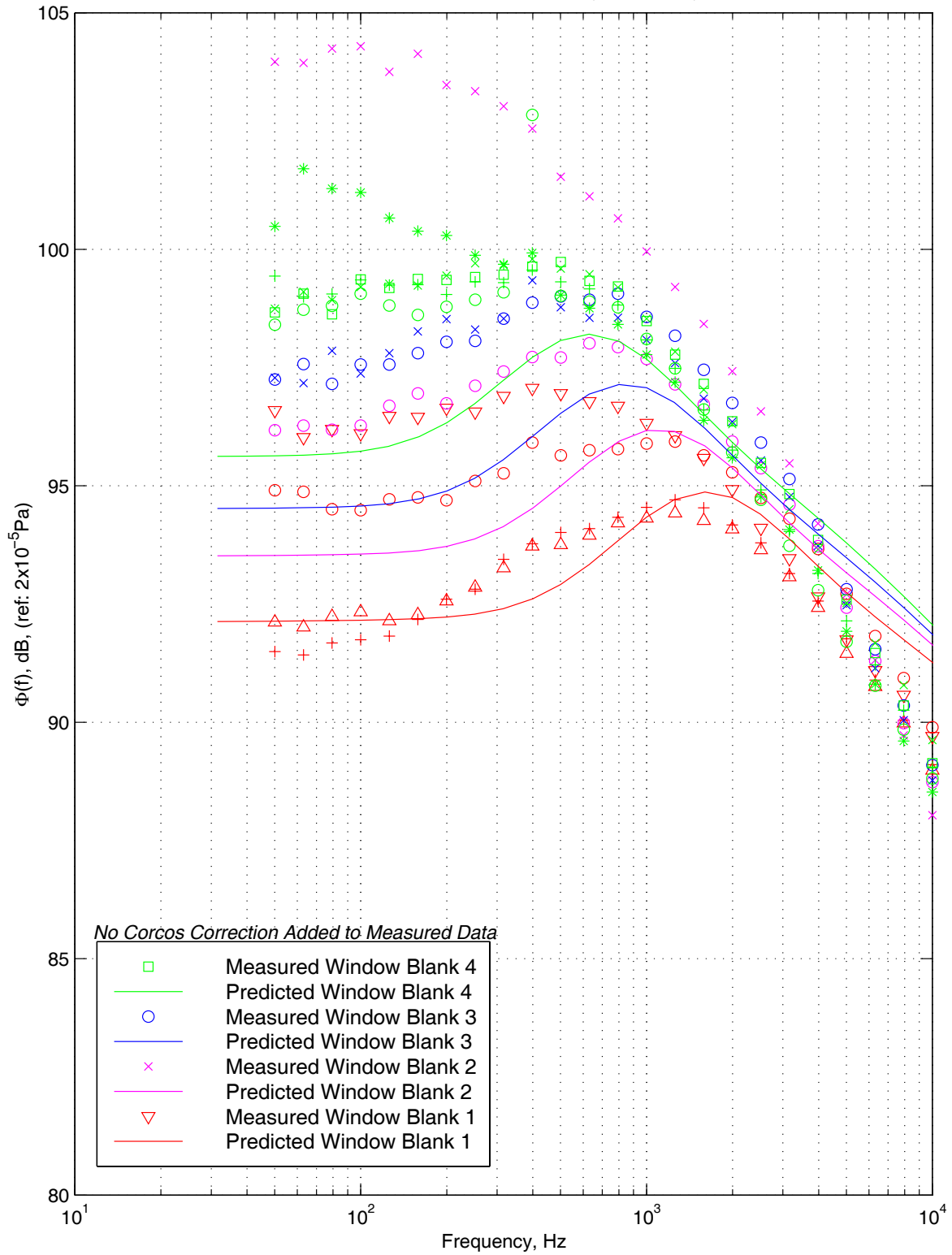
Figure 65 Adjusted Efimtsov Predicted SPL and Measured Flight Test Data from Concorde (Mach 2)

7. Consequences of Model Adjustments to HSCT Interior Noise

What follows is a qualitative assessment of what changes one might expect in HSCT interior noise predictions that are based on the Efimtsov model:

- The broad spectral peak is added in a frequency range roughly from 200 to 3000 Hz. In the higher end of this range the human ear is particularly sensitive. In the lower end of that range, fuselage structures often exhibit coincidence effects (particularly honeycomb) or panel resonances (particularly skin/stringer).

- The small change of the high frequency roll-off slope decreases the high frequency portion at Mach numbers below 1.65, and increases it above that Mach number.

Without the benefit of a detailed quantitative analysis, one might engage in educated speculation that high Mach number cruise interior levels will increase somewhere between 1 to 3 dB.

For most of the length of the fuselage (middle and aft) the model adjustment adds noise energy mostly at frequencies below 1000 Hz, regardless of Mach number. This is the area where active noise control shows the most promise.

8. Recommendations for Future Work

The following items should be considered for future work:

- Auto-Spectra:

  - Use Boeing data (777, MD-90) to further evaluate subsonic performance of the adjusted model.

  - Explanation of higher than currently predicted levels in the aft portion of the fuselage, found in Concorde as well as TU-144 measurements. Possibly further adjust the model.

  - Use A. Frendi's numerical prediction method to investigate the high Reynolds number and the thick boundary layer situation on the aft fuselage.

  - Include in the model effects of pressure gradients on the boundary layer, particularly the negative gradient on the tail cone section.

- Cross-Spectra:

  - Correct the measured cross-functions for the influence of local flow direction (measured on the TU-144 in 1999 [Ref. 18])

  - Adjust the cross-functional model using measured cross-functions using more of the TU-144 data than presented here

- Use ideas from Smol'yakov-Tkachenko and further develop a model for high Reynolds and Mach numbers without the assumption of multiplicative separability of the functions of the time and space separation variables.

9. References

Ref. 1   "Prediction of In-Flight Fluctuating Pressure Environments Including Protuberance Induced Flow" Wyle Laboratories Research Staff Report, WR71-10, (1971).

Ref. 2   "Estimation of the Surface Pressure Fluctuations in the TBL of a Flight Vehicle," Engineering Sciences Data Unit, Item Number 75021, (1975).

Ref. 3   Laganelli, A. L., Wolfe, H., "Prediction of Fluctuating Pressure in Attached and Separated TBL Flow," AIAA 12th Aeroacoustics Conference, AIAA Paper 89-1064, (1989).

Ref. 4   Goodwin, P. W., "An In-Flight Supersonic TBL Surface Pressure Fluctuation Model", Contract No. NAS1-20013, Boeing Document No. D6-81571 (1994).

Ref. 5   Efimtsov, B. M., "The Prediction of the Pressure Fluctuation Field Characteristics of the TBL", Contract No. BTRC-101F, Document No. BTRC101F-5/95, (1995)

Ref. 6   Blake, W. K., Mechanics of Flow-Induced Sound and Vibration, Academic Press, Inc., New York, 1986.

Ref. 7   Bies, D. A., "A Review of Flight and Wind Tunnel Measurements of Boundary Layer Pressure Fluctuations and Induced Structural Response", NASA CR-626, (1965).

Ref. 8   Efimtsov, B. M., Munin, A. G., "Determination of Optimal Fluctuation Pressure Transducer Mount Configuration and Frequency Response for Tu144LL" proprietary report by Central Aerohydrodynamic Institute (TsAGI) in Moscow, Russia, to The Boeing Company, August 1996.

Ref. 9   Lohman, K. T., "Cabin Noise and Turbulent Boundary Layer Pressure Fluctuations on a British Airways Concorde Aircraft – Test Report", Boeing Document No. T6-6970, (1994)

Ref. 10   Rizzi, S.A., Rackl, R.G., Andrianov, E.V., "Flight Test Measurements from the Tu-144LL Structure/Cabin Noise Experiment, NASA TM-2000-209858, January 2000.

Ref. 11   Efimtsov, B.M., Personal Communication, October 1998.

Ref. 12   Duff, G.F.D., Naylor, D., "Differential Equations of Applied Mathematics", Wiley 1966, Fourier transform tables, p.411 ff.

Ref. 13   Efimtsov, B.M., "Characteristics of the field of turbulent wall pressure fluctuations at large Reynolds numbers", Sov. Phys. Acoust. 28(4), July-August 1982, pp 289-292.

Ref. 14   Corcos, G.M., "Resolution of Pressure in Turbulence", J. Acoust. Soc. Amer. 35(2), February 1963.

Ref. 15   Spalart, P. (Boeing Associate Technical Fellow), Personal Communications, September/October 1998.

Ref. 16   Schewe, G., "On the structure and resolution of wall-pressure fluctuations associated with turbulent boundary-layer flow," J. Fluid Mech. (1983), vol. 134, pp. 311-328.

Ref. 17   Smol'yakov, A.V., Tkachenko, V.M., "Model of a field of pseudosonic turbulent wall pressures and experimental data", Sov. Phys. Acoust. 37(6), Nov.-Dec. 1991.

Ref. 18   Rizzi, S.A., Rackl, R.G., Andrianov, E.V., "Flight Test Measurements from the Tu-144LL Structure/Cabin Noise Follow-On Experiment, NASA TM-2000-209859, February 2000.

10. Appendix A - ESDU Equations

Equations for calculating fluctuating pressure levels derived by ESDU [Ref. 3]:

$$L_a = 178.441947 + \log_{10}(M)\left(39.29984 + \log_{10}(M)\left(3.0984996 - \log_{10}(M)\left(25.32020 + 25.18335 \cdot \log_{10}(M)\right)\right)\right)$$

$$L_b = -5.2735 - \log_{10}(M)\left(0.19002 + \log_{10}(M)\left(2.29509 - \log_{10}(M)\left(4.83039 + 5.93327 \cdot \log_{10}(M)\right)\right)\right)$$

$$L_c = 0.16237 - \log_{10}(M)\left(0.00510 - \log_{10}(M)\left(0.01416 - \log_{10}(M)\left(0.30915 + 0.37894 \cdot \log_{10}(M)\right)\right)\right)$$

$$L_p = 20 \times \log_{10}\left(\frac{1481.34}{\frac{1}{2}\rho_\infty c^2}\right)$$

$$L_1 = L_a + \log_{10}(Re) \times \left(L_b + \log_{10}(Re) \times L_c\right) - L_p$$

$$L_u = 10 \times \log_{10}\left(\frac{U_\infty}{\delta^*}\right)$$

$$L_s = -8.24 - \log_{10}(St) \times$$

$$\left(12.84 + \log_{10}(St)\left(6.95 + \log_{10}(St)\left(24.75 + \log_{10}(St)\left(29.30 + \log_{10}(St)\left(14.26 + \log_{10}(St)\left(3.17 + 0.27 \cdot \log_{10}(St)\right)\right)\right)\right)\right)$$

$$\Phi(f_i) = L_s + L_1 - L_u + 10 \times \log_{10}\left(bandwidth(f_i)\right)$$

11. Appendix B - Fourier Transform of a Turbulence Cross-Correlation Model

This work was performed with the expectation of creating an improved cross-spectral pressure fluctuation model, but could not be completed due to lack of time. The partial effort is documented here for the time when it can be continued.

When computing cross functions using the TU-144 data, cross-correlations turn out to be nicely smooth curves to which a model can be fitted with little uncertainty. Cross-spectra are harder to fit since they contain more noise and consist of real and imaginary parts. The approach to modeling cross-spectra is therefore to model the cross-correlations and to Fourier transform that model to obtain the cross-spectrum.

One way of modeling a cross-correlation function as a function of time delay τ is shown in Eq. 1. This form was chosen such as to be able to fit measured correlations with functions that have relatively simple Fourier transforms. Ref. 12 provides Fourier transform formulas.

$$R(\tau) = r_0 + e^{-\left(\frac{\tau-\hat{\tau}}{\tau_{s1}}\right)^2}\left[r_1 + r_2\left(\frac{\tau-\hat{\tau}}{\tau_{s2}}\right)^2 + r_3\cos\left(2\pi f_0(\tau-\hat{\tau})\right)\right] + \frac{r_4}{1+\left(\frac{\tau-\hat{\tau}}{\tau_{s3}}\right)^2} \qquad \textbf{Eq. 1}$$

Meaning of Symbols:

$\hat{\tau}$ = time delay of peak of cross-correlation

τ_{si} = time delay scale factors

r_i = magnitude constants

f_0 = frequency of spectral peak

The objective is to find the Fourier transform of this function, defined by

$$F\{R(\tau)\} = \int_{-\infty}^{\infty} R(\tau)e^{-2\pi i f\tau}d\tau \qquad \textbf{Eq. 2}$$

Eq. 1 can be re-written:

$$R(\tau) = r_0 + I_1 + I_2 + I_{3.1} + I_{3.2} + I_4$$

$$\textbf{Eq. 3}$$

where: $\quad I_1 = r_1 e^{-\left(\frac{\tau-\hat{\tau}}{\tau_{s1}}\right)^2}$, $\qquad\qquad\qquad I_2 = r_2 e^{-\left(\frac{\tau-\hat{\tau}}{\tau_{s1}}\right)^2}\left(\frac{\tau-\hat{\tau}}{\tau_{s2}}\right)^2$

$$I_{3.1} = \frac{r_3}{2}e^{-\left(\frac{\tau-\hat{\tau}}{\tau_{s1}}\right)^2}e^{2\pi i f_0(\tau-\hat{\tau})}, \qquad\qquad I_{3.2} = \frac{r_3}{2}e^{-\left(\frac{\tau-\hat{\tau}}{\tau_{s1}}\right)^2}e^{-2\pi i f_0(\tau-\hat{\tau})}$$

$$I_4 = \frac{r_4}{1+\left(\frac{\tau-\hat{\tau}}{\tau_{s3}}\right)^2}$$

Each element on the right hand side of Eq. 3 can be Fourier transformed separately:

$$F\{r_0\} = r_0 \delta(f = 0)$$

<div align="right">**Eq. 4**</div>

$$F\{I_1\} = r_1 \int_{-\infty}^{\infty} e^{-\left(\frac{\tau-\hat{\tau}}{\tau_{s1}}\right)^2 - 2\pi i f \tau} d\tau = r_1 \tau_{s1} \int_{-\infty}^{\infty} e^{-x^2 - 2\pi i f (\tau_{s1} x + \hat{\tau})} dx$$

where: $x = \left(\frac{\tau - \hat{\tau}}{\tau_{s1}}\right)$, $\tau = \tau_{s1} x + \hat{\tau}$, $d\tau = \tau_{s1} dx$

$$F\{I_1\} = r_1 \tau_{s1} \int_{-\infty}^{\infty} e^{-x^2 - 2\pi i f \tau_{s1} x - 2\pi i f \hat{\tau}} dx = r_1 \tau_{s1} \int_{-\infty}^{\infty} e^{-(x^2 + 2\pi i f \tau_{s1} x + (\pi i f \tau_{s1})^2 - (\pi i f \tau_{s1})^2 + 2\pi i f \hat{\tau})} dx$$

$$= r_1 \tau_{s1} e^{-\pi^2 \tau_{s1}^2 f^2 - 2\pi i f \hat{\tau}} \int_{-\infty}^{\infty} e^{-(x + \pi i f \tau_{s1})^2} dx = \underline{r_1 \tau_{s1} \sqrt{\pi} e^{-\pi^2 \tau_{s1}^2 f^2 - 2\pi i f \hat{\tau}}} = F\{I_1\}$$

<div align="right">**Eq. 5**</div>

$$F\{I_2\} = r_2 \int_{-\infty}^{\infty} \left(\frac{\tau - \hat{\tau}}{\tau_{s2}}\right)^2 e^{-\left(\frac{\tau-\hat{\tau}}{\tau_{s1}}\right)^2 - 2\pi i f \tau} d\tau = r_2 \left(\frac{\tau_{s1}}{\tau_{s2}}\right)^2 \int_{-\infty}^{\infty} \left(\frac{\tau - \hat{\tau}}{\tau_{s1}}\right)^2 e^{-\left(\frac{\tau-\hat{\tau}}{\tau_{s1}}\right)^2 - 2\pi i f \tau} d\tau$$

$$= r_2 \left(\frac{\tau_{s1}}{\tau_{s2}}\right)^2 \tau_{s1} \int_{-\infty}^{\infty} x^2 e^{-x^2 - 2\pi i f \tau} dx = r_2 \left(\frac{\tau_{s1}}{\tau_{s2}}\right)^2 \tau_{s1} \int_{-\infty}^{\infty} x^2 e^{-x^2 - 2\pi i f \tau_{s1} x - 2\pi i f \hat{\tau}} dx$$

$$= \frac{r_2}{r_1} \left(\frac{\tau_{s1}}{\tau_{s2}}\right)^2 r_1 \tau_{s1} e^{-\pi^2 \tau_{s1}^2 f^2 - 2\pi i f \hat{\tau}} \int_{-\infty}^{\infty} x^2 e^{-(x + \pi i f \tau_{s1})^2} dx = \frac{r_2}{r_1} \left(\frac{\tau_{s1}}{\tau_{s2}}\right)^2 i^2 \frac{d^2 F\{I_1\}}{df^2}$$

$$= -\frac{r_2}{r_1} \left(\frac{\tau_{s1}}{\tau_{s2}}\right)^2 r_1 \tau_{s1} 2\pi \sqrt{\pi} \frac{d}{df} \left[e^{-\pi^2 \tau_{s1}^2 f^2 - 2\pi i f \hat{\tau}} \left(-\pi \tau_{s1}^2 f - i\hat{\tau}\right) \right]$$

$$= -\frac{r_2}{r_1} \left(\frac{\tau_{s1}}{\tau_{s2}}\right)^2 r_1 \tau_{s1} (2\pi)^2 \sqrt{\pi} e^{-\pi^2 \tau_{s1}^2 f^2 - 2\pi i f \hat{\tau}} \left[\left(-\pi \tau_{s1}^2 f - i\hat{\tau}\right)^2 + \left(-\pi \tau_{s1}^2\right) \right] = \underline{F\{I_2\}}$$

<div align="right">**Eq. 6**</div>

$$I_{3_{1,2}} = \frac{r_3}{2} \int_{-\infty}^{\infty} e^{-\left(\frac{\tau-\hat{\tau}}{\tau_{s1}}\right)^2 \pm 2\pi i f_0 (\tau - \hat{\tau}) - 2\pi i f \tau} d\tau = \frac{r_3 \tau_{s1}}{2} \int_{-\infty}^{\infty} e^{-x^2 \pm 2\pi i f_0 \tau_{s1} x - 2\pi i f \tau_{s1} x - 2\pi i f \hat{\tau}} dx$$

$$= \frac{r_3 \tau_{s1}}{2} \int_{-\infty}^{\infty} e^{-\left(x^2 + 2\pi i \tau_{s1} x (f \mp f_0) + 2\pi i f \hat{\tau}\right)} dx = \frac{r_3 \tau_{s1}}{2} \int_{-\infty}^{\infty} e^{-\left(x^2 + 2\pi i \tau_{s1} x (f \mp f_0) - \pi^2 \tau_{s1}^2 (f \mp f_0)^2 + \pi^2 \tau_{s1}^2 (f \mp f_0)^2 + 2\pi i f \hat{\tau}\right)} dx$$

$$= \frac{r_3 \tau_{s1}}{2} e^{-\pi^2 \tau_{s1}^2 (f \mp f_0)^2 - 2\pi i f \hat{\tau}} \int_{-\infty}^{\infty} e^{-(x + \pi i \tau_{s1} (f \mp f_0))^2} dx = \underline{r_3 \tau_{s1} \frac{\sqrt{\pi}}{2} e^{-\pi^2 \tau_{s1}^2 (f \mp f_0)^2 - 2\pi i f \hat{\tau}}} = I_{3_{1,2}}$$

<div align="right">**Eq. 7**</div>

$$F\{I_4\} = r_4 \int_{-\infty}^{\infty} \frac{e^{-2\pi i f \tau}}{1 + \left(\frac{\tau - \hat{\tau}}{\tau_{s3}}\right)^2} d\tau$$

Substitute: $x = \tau - \hat{\tau}$, $\tau = x + \hat{\tau}$, $d\tau = dx$

$$F\{I_4\} = r_4 e^{-2\pi i f \hat{\tau}} \int_{-\infty}^{\infty} \frac{e^{-2\pi i f x}}{1+\left(\dfrac{x}{\tau_{s3}}\right)^2} dx = r_4 e^{-2\pi i f \hat{\tau}} \tau_{s3}^2 \int_{-\infty}^{\infty} \frac{e^{-2\pi i f x}}{\tau_{s3}^2 + x^2} dx = r_4 e^{-2\pi i f \hat{\tau}} \pi \tau_{s3} e^{-2\pi \tau_{s3} f}$$

$$\underline{F\{I_4\} = r_4 \pi \tau_{s3} e^{-2\pi f (\tau_{s3} + i\hat{\tau})}}$$

Eq. 8

REPORT DOCUMENTATION PAGE

Form Approved
OMB No. 0704-0188

1. REPORT DATE *(DD-MM-YYYY)*	2. REPORT TYPE	3. DATES COVERED *(From - To)*
01-12-2005	Contractor Report	Sep 1997 - Nov 1998

4. TITLE AND SUBTITLE

Modeling of Turbulent Boundary Layer Surface Pressure Fluctuation Auto and Cross Spectra – Verification and Adjustments Based on TU-144LL Data

5a. CONTRACT NUMBER

NAS1-20220

5b. GRANT NUMBER

5c. PROGRAM ELEMENT NUMBER

6. AUTHOR(S)

Rackl, Robert
Weston, Adam

5d. PROJECT NUMBER

5e. TASK NUMBER

5f. WORK UNIT NUMBER

537-06-37-20

7. PERFORMING ORGANIZATION NAME(S) AND ADDRESS(ES)

The Boeing Company
Seattle, WA

8. PERFORMING ORGANIZATION REPORT NUMBER

9. SPONSORING/MONITORING AGENCY NAME(S) AND ADDRESS(ES)

National Aeronautics and Space Administration
Washington, DC 20546-0001

10. SPONSORING/MONITOR'S ACRONYM(S)

NASA

11. SPONSORING/MONITORING REPORT NUMBER

NASA/CR-2005-213938

12. DISTRIBUTION/AVAILABILITY STATEMENT

Unclassified-Unlimited
Subject Category 71
Availability: NASA CASI (301) 621-0390

13. SUPPLEMENTARY NOTES

Langley Technical Monitor: Stephen A. Rizzi. An electronic version can be found at http://ntrs.nasa.gov

14. ABSTRACT

The literature on turbulent boundary layer pressure fluctuations provides several empirical models which were compared to the measured TU-144 data. The Efimtsov model showed the best agreement. Adjustments were made to improve its agreement further, consisting of the addition of a broad band peak in the mid frequencies, and a minor modification to the high frequency roll-off. The adjusted Efimtsov predicted and measured results are compared for both subsonic and supersonic flight conditions. Measurements in the forward and middle portions of the fuselage have better agreement with the model than those from the aft portion. For High Speed Civil Transport supersonic cruise, interior levels predicted by use of this model are expected to increase by 1-3 dB due to the adjustments to the Efimtsov model. The space-time cross-correlations and cross-spectra of the fluctuating surface pressure were also investigated. This analysis is an important ingredient in structural acoustic models of aircraft interior noise. Once again the measured data were compared to the predicted levels from the Efimtsov model.

15. SUBJECT TERMS

High speed research; Tupolev 144; Tu-144LL; Supersonic turbulent boundary layer pressure fluctuations

16. SECURITY CLASSIFICATION OF:			17. LIMITATION OF ABSTRACT	18. NUMBER OF PAGES	19a. NAME OF RESPONSIBLE PERSON
a. REPORT	b. ABSTRACT	c. THIS PAGE	UU	88	STI Help Desk (email: help@sti.nasa.gov)
U	U	U			19b. TELEPHONE NUMBER *(Include area code)*
					(301) 621-0390

Standard Form 298 (Rev. 8-98)
Prescribed by ANSI Std. Z39-18